UNIVERSITÀ della CALABRIA
Facoltà di Ingegneria
Dipartimento di Meccanica

Dottorato di Ricerca in Ingegneria Meccanica

XXV Ciclo (2009-2012)

Scuola di Dottorato "Pitagora" in Scienze Ingegneristiche

SSD: ING-IND/14 – Progettazione Meccanica e Costruzione di Macchine

Dissertazione finale sottomessa per il conseguimento il titolo di Dottore di Ricerca in Ingegneria Meccanica

Design and application of a novel microelectromechanical system for *in situ* SEM/TEM displacement controlled tensile testing of nanostructures

Coordinatore
Prof. Sergio Rizzuti

Supervisori
Prof. Leonardo Pagnotta

Prof. Horacio Espinosa

Candidata
Ing. Maria Pantano

Anno Accademico 2011/2012

UNIVERSITÀ della CALABRIA
Facoltà di Ingegneria
Dipartimento di Meccanica

Dottorato di Ricerca in Ingegneria Meccanica

XXV Ciclo (2009-2012)

Scuola di Dottorato "Pitagora" in Scienze Ingegneristiche

SSD: ING-IND/14 – Progettazione Meccanica e Costruzione di Macchine

Dissertazione finale sottomessa per il conseguimento il titolo di Dottore di Ricerca in Ingegneria Meccanica

Design and Application of a novel microelectromechanical system for in situ SEM/TEM displacement controlled tensile testing of nanostructures

Coordinator

Prof. Sergio Rizzuti

Advisors

Prof. Leonardo Pagnotta

Prof. Horacio Espinosa

Candidate

Ing. Maria Pantano

Anno Accademico 2011/2012

Contents

Estratto

Il presente lavoro si apre con un confronto fra le principali metodologie per la caratterizzazione meccanica dei materiali alla micro- e nanoscala (ovvero, caratterizzazione di componenti con dimensione caratteristica nell'ordine dei micro- e nanometri), sviluppate dalla comunità scientifica a partire dalla prima metà del XX secolo, allo scopo di individuare fra queste le più versatili e maggiormente efficaci. Le tecniche più promettenti sono basate sullo sviluppo di microsistemi elettromeccanici (MEMS) appositamente progettati, che riproducono su un wafer di silicio (con area inferiore ad un $1mm^2$ e spessore dell'ordine di pochi μm) una struttura di prova completa e miniaturizza, adatta ad effettuare test di trazione su provini con dimensioni caratteristiche dell'ordine del micro- e nanometro.

L'efficacia di tali dispositivi, evidente, soprattutto, nella loro compatibilità con la microscopia elettronica (microscopi elettrici a scansione/trasmissione-SEM/TEM), può, tuttavia, essere condizionata da diversi fenomeni di disturbo, che possono compromettere il buon esisto delle prove. Uno di questi fenomeni di disturbo, già noto in letteratura, è legato all'insorgere di meccanismi di instabilità, che rendono impossibile seguire eventuali tratti di rilassamento tensionale nella curva caratteristica dei provini (*softening*), che sono, però, di grande interesse scientifico, in quanto legati ad un singolare

comportamento del materiale. Il problema dell'instabilità viene superato, nel presente lavoro, con l'implementazione di una nuova soluzione progettuale, che è stata introdotta e verificata nel disegno e successiva applicazione di un nuovo dispositivo di prova. In particolare, esso è un vero e proprio MEMS, che consente l'esecuzione di prove di trazione al SEM/TEM in controllo di spostamento.

L'architettura del chip di prova è, come da tradizione, basata sulla presenza di due elementi principali, ciascuno dei quali collegato ad una delle due estremità del provino da testare. Il primo elemento è un attuatore termico, che, una volta attivato, mette in trazione un provino, che è collegato, dalla parte opposta, ad un sensore di spostamento. Questo, a causa del carico trasmessogli dall'attuatore tramite il provino stesso, devia dalla sua iniziale posizione di equilibrio.

La novità del progetto presentato è nell'implementazione di uno schema retroazionato, ovvero nella presenza di un controllore, che, in base al segnale fornito in uscita dal sensore, aziona un attuatore elettrostatico, capace di generare la forza necessaria a riportare il sensore stesso nella sua posizione iniziale di equilibrio. In tal modo, l'estremità del provino collegata al sensore di spostamento risulta, in pratica, incastrata (per via elettronica), condizione questa che impedisce l'insorgere di fenomeni di instabilità.

I componenti del dispositivo MEMS sono stati dimensionati mediante modellazione analitica e numerica, per garantire che le prove siano condotte in controllo di spostamento, e con la possibilità di applicare deformazioni (fino al 50%) e carichi (fino a circa 100μN) sufficientemente elevati per portare a rottura un'ampia varietà di provini di diverso materiale.

Il progetto è stato poi completato con il disegno di tutte le maschere necessarie per la successiva fabbricazione del dispositivo, eseguita in commessa

esterna da una compagnia specializzata.

Al termine del processo di fabbricazione, è stato assemblato un apposito set-up sperimentale, capace di garantire il corretto funzionamento del sistema di prova, fornendo connessioni elettriche fra il dispositivo MEMS ed una strumentazione esterna, comprendente amplificatori di corrente, generatori di tensione, un amplificatore lock-in ed una scheda di acquisizione dati, che consente di interfacciare il chip con il controllore, implementato al calcolatore.

L'efficacia del sistema di prova sviluppato è stata dimostrata mediante una applicazione su nanofilamenti di argento con diametro di circa 70nm e una base di misura di 3-4 μm. I risultati ottenuti hanno fornito una stima delle proprietà meccaniche di questo materiale, in termini di modulo di Young, tensione di snervamento e rottura, in linea con dati già presenti in letteratura, ricavati per provini di dimensioni analoghe. È stata anche verificata la capacità del dispositivo di seguire tratti discendenti della curva caratteristica dei provini, come risulta nel caso specifico di un test, durante il quale è stato registrato una brusco rilassamento delle tensioni, in corrispondenza dello snervamento del provino in esame.

In future applicazioni, il presente sistema di prova sarà adoperato per effettuare altri test di trazione al SEM e TEM su diversi tipi di materiale. In aggiunta, poiché i provini risultano elettricamente isolati dal corpo del dispositivo MEMS, sarà possibile effettuare anche prove elettromeccaniche, volte a valutare proprietà, come piezoresistività e piezoelettricità, che stanno attirando un interesse crescente nell'ambito della progettazione di dispositivi elettrici ed elettromeccanici sempre più efficienti.

Abstract

Since the 1920s, different methodologies have been developed especially for mechanical characterization of material samples with characteristic length on the order of micro/nanometers. In the present manuscript, the main of such methodologies are presented and compared, in order to provide guidelines for mechanical characterization at the micro/nanoscale, and to identify the most versatile and effective among them. These are based on complete and miniaturized tensile testing stages, developed on proper microelectromechanical systems (MEMS). Because of their small size (they lie onto silicon wafers with area smaller than $1mm^2$ and thickness of only few micrometers), such testing devices are particularly suitable to handle micro/nanosized components, and can fit inside the tight chamber of scanning/transmission electron microscopes (SEM/TEM), for real-time imaging of sample deformation.

However, the effectiveness of the tests they allow to perform can be compromised by some disturbing phenomena, like onset of instability, as reported in a certain kind of tensile testing devices. In particular, these devices become unstable as soon as the sample under investigation shows stress relaxation, after some strain has been applied. Nevertheless, it is very important to be able to detect such singularities, since they may allow a deeper comprehen-

sion of materials' behavior.

In the present work, the above mentioned instability issue is overcome through the design of a novel device for *in situ* SEM/TEM tensile testing of nanostructures under true displacement control. Like other stages, also the one presented herein consists of two main components: an actuator and a sensor, which are separated by a small gap for positioning of the specimen. Actuation is performed by a thermal actuator, which pulls the end of the sample attached to it. The other end of the sample is instead connected to a displacement sensor, which moves from its equilibrium position, as a consequence of the force transmitted to it by the specimen. However, the main novelty of the present design is the introduction of a feedback control loop. In particular, a controller, implemented within a software routine, receives as input the sensor output, and computes the voltage to be applied to an electrostatic actuator, in order to generate a rebalance force of electrostatic nature, thus bringing the sensor back to equilibrium. In this way, the end ofand this boundary condition removes any potential source of instability.

The MEMS sensing and actuating structures were designed by the means of both analytical and numerical approaches, in order to provide sufficiently high deformation (up to about 50% strain) and forces (up to 100μN) to break a variety of material samples. Fabrication was carried out by an external foundry on the basis of the masks drawings, reported in the present manuscript.

In order to guarantee a correct functioning of the device, a proper experimental apparatus was developed. This allowed electrical connection of all of the actuating and sensing parts with external instrumentation, including current pre-amplifiers, power supplies, a lock-in amplifier, and a data acquisition card, which was used as interface between the controller and the

MEMS device.

The effectiveness of the present experimental apparatus was proven through an application on silver nanowires, with about 70 nm diameter and 3-4 μm gage length. The corresponding results, in terms of Young modulus, fracture and yield strength, showed good agreement with data already available in the literature, obtained for samples with comparable size. Also the device ability to detect singularities in the sample characteristic was demonstrated, as emerges from a load drop recorded after yielding of a nanowire.

As a conclusion, the present experimental apparatus can be considered for future *in situ* SEM/TEM tensile tests on other material samples, as well as for electromechanical tests, since the specimen results to be electrically isolated from the remaining of the device. Thus, very interesting properties, like piezoresistivity and piezoelectricity, could be evaluated.

Introduction

Mechanical characterization of materials at the micro/nanoscale has acquired increasing attention during the last two decades, as acknowledged by the dramatical increase in number of correlated studies. Such trend can be explained by two main reasons. First, experiments carried out on micro/nanostructures, like carbon nanotubes and metallic nanowires, have shown an extraordinary behavior, not known at the macroscale, which can be exploited for a new generation of devices. Secondly, the further scaling down of electronic systems, like micro/nanoelectromechanical systems (MEMS/NEMS), is shrinking the size of their structural components to micro/nanometers. Thus, the design of even more performing and competitive as well as reliable devices, requires a deep knowledge of the mechanical behavior of the involved materials at such small length scales. However, many challenges arise in this context. First of all, on dealing with micro/nanosized samples, the common engineers' practice to consider materials mechanical properties independent of components physical dimension is no longer adequate. In fact, the above mentioned nanotubes and nanowires have unique properties, not shown by their bulk counterparts. Thus, the results of standard tests on macrosamples are not valid at this scale. Secondly, the size effect while being the key to the extraordinary behavior of

micro/nanosamples, causes their manipulation and testing not possible with standard techniques. This is the reason why the scientific community has addressed so many efforts to develop mechanical testing systems suitable for micro/nanocomponents. Among those apparatus, the most promising are the so called *on-chip* testing devices. These are true micro electromechanical systems (MEMS), which provide on a platform of about 1x1 mm^2, all the structures for loading samples with a characteristic length on the order of micro- or nanometers (10^{-6} and 10^{-9} m, respectively) and for sensing the corresponding displacements. Many are the advantages such systems can offer, but certainly the most important feature is their compatibility with the tight chamber of scanning/transmission electron microscopes (SEM/TEM). In particular, since they can be positioned inside SEM/TEM, tests can be performed under real time imaging of sample deformation, thus providing many information which otherwise could not be derived.

However, such testing systems require quite sophisticated design and calibration procedures, and their effectiveness can be compromised by a number of issues, including not perfect alignment between the sample axis and loading direction, and, above all, the onset of instability in certain kind of devices for tensile testing, as it is recorded as soon as the sample characteristic shows stress relaxation (e.g., softening).

In order to solve this latter critical issue, a novel *on-chip* tensile testing device was designed[1], as reported in present manuscript. This is organized in six chapters, each describing one aspect of the design and assembly of the experimental apparatus necessary to guarantee a correct functioning of the device.

[1]All of the associated experimental work was carried out at the Micro and Nanomechanics Laboratory of Northwestern University (Evanston, IL).

In particular, after providing (chapter 1) an overview of the different techniques developed for mechanical characterization of micro- and nanocomponents, in order to highlight the potential of the above mentioned on-chip testing devices, the attention is then focused on the instability issue affecting a certain kind of tensile testing devices (chapter 2). To discuss this topic in details, an analytical model is derived to explain the causes generating instability, and then a solution for this problem is proposed. This involves the implementation of an electrostatic feedback control in a custom-made software routine. As it emerges, the experimental setup needed for conducting tests with the present device requires many elements, beyond the device itself. In particular, it includes proper electronics for providing connection between the device and external instrumentation, as amplifiers, power supplies, as well as a personal computer for implementation of the controller. For the sake of clarity, each of these elements is considered in a separated chapter. In particular, chapter 3 is focused on the mechanical design of the device, and the process adopted for its fabrication. Later, chapter 4 illustrates how the controller was implemented in a software routine properly designed for the present application. Then, chapter 5 presents all of the electrical connection and external instrumentation, building up the present experimental apparatus, whose effectiveness is finally proven through an application on tensile testing of silver nanowires (chapter 6).

Chapter 1

Mechanical characterization of materials at the micro- and nanoscale

1.1 Interest in mechanical characterization of materials at the micro- and nanoscale

Mechanical behavior of materials at the micro- and nanoscale has gained increasing attention during the last two decades, as a natural consequence of the development of micro and nanoelectromechanical systems (MEMS/ NEMS), and various kinds of nanostructures (e.g., nanotubes, nanowires, and nanoribbons). MEMS/NEMS are micro/nanoscale devices fabricated with appropriate techniques, derived from integrated circuits (ICs) fabrication processes. They are able to perform a variety of functions, and since the 1990s, due to their small size, short time response, high performance, and

low energy requirements, they have found common application in several fields, ranging from consumer's electronics to the automotive and biomedical industry [1]-[4].

From a structural point of view, a MEMS is a stack of different material layers, including ceramics (silicon, silicides), metals, and even polymers, with thickness ranging from hundreds of nanometers (10^{-9}m) to tens of micrometers (10^{-6}m). Hence, the mechanical behavior of such small components is a key factor for a competitive and effective design.

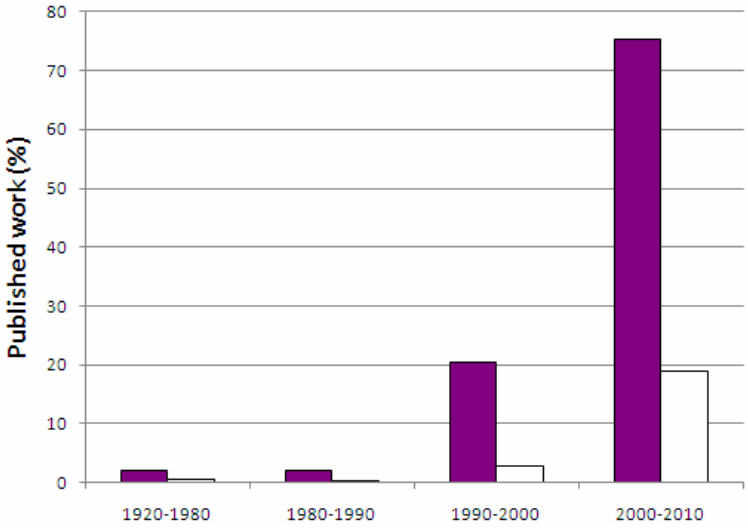

Figure 1.1: Scientific production about mechanical characterization of materials at the micro- and nanoscale since the 1920s: in purple the global production, in white the production related to the nanoscale.

However, in spite of the usual engineers' common sense, it has been well known for many years that materials behavior is size dependent at such length scales [5]-[6]. For example, metals, when shaped as nanowires, exhibit very interesting thermal, optical, and mechanical properties, which

are instead not observed in bulk counterparts [7]. Similarly, the particular atoms arrangement of carbon nanotubes and graphene is responsible for their extraordinary physical and mechanical properties [8]. Unfortunately, the size effect, while being the key to the unique behavior of nanostructures, causes mechanical properties of MEMS/NEMS materials to not be derived from bulk properties evaluated through traditional methods.

Furthermore, the standardized well-assessed methodologies for mechanical characterization at the macroscale are not effective at the micro/nanoscale. In fact, they involve machinery and equipment, which are not suitable for manipulation of micro/nanocomponents. Thus, it should not be a surprise that many researchers have been interested in the development of dedicated micro/nanotesting procedures. In particular, such interest has increased since the 1980s, promoted by the advent of the first MEMS inside some research laboratories (figure 1.1). Figure 1.1 shows the trend of scientific papers published in the main international journals, referring to mechanical characterization of materials at the micro- and nanoscale since the 1920s [9]. Here, purple bars are related to works on both micro- and nanocomponents, whereas white bars include those experiments carried out on samples with characteristic length strictly on the order of nanometers. These latter studies have been increasing but not as dramatically as those performed on samples with characteristic length on the order of micrometers. This can be explained since MEMS are commercially available since the 1990s, whereas NEMS are not yet.

All of these experiments, gathered to draw the plot in figure 1.1, involve the development of different procedures, which have been applied on a variety of materials in order to identify their major mechanical properties, including Young's modulus, Poisson's ratio, yield strength, fracture strength, hard-

ness, and endurance limit. The main of such procedures will be separately discussed in the following sections.

1.2 Methodologies for mechanical testing of materials at the micro and nanoscale

As already anticipated, several experimental techniques have been developed for mechanical characterization of micro- and nanosamples. However, they all share the common feature of requiring high resolution systems for load and displacement measurements.

Typical tools able to guarantee nanometer resolution are scanning/ transmission electron microscopes (SEM/TEM), which are involved in many micro/ nanoscale testing systems, as shown later in more detail.

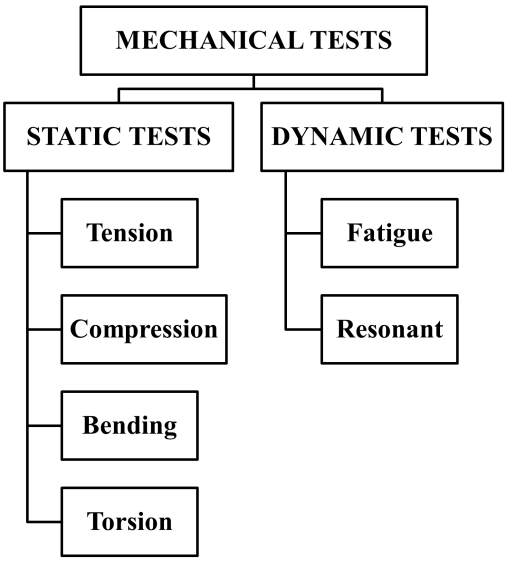

Figure 1.2: Main methodologies for mechanical testing of materials at the micro- and the nanoscale

With reference to force measurements, the literature offers many and different solutions. In particular, usually researchers prefer developing their own testing stages, including custom-made transducers, some of which were also patented [10]. However, commercial load cells are also available, as well as complete testing stages, like those released on the market by DTS (Menlo Park, Ca) and Zwick (Ulm, Ge) [11]-[12].

Among all of these testing systems, particularly interesting are the *on-chip* testing devices. In fact, unlike other apparatus, these are real MEMS with the unique advantage to be so small to be compatible with the chambers of SEM/TEM. Thus, they allow performance of tests under real-time imaging of the sample deformation, thus providing useful information to advance the knowledge of fracture mechanisms at small length scales [13].

Tests at the micro/nanoscale can be grouped in the same two categories as those performed at the macroscale: static tests and dynamic tests (figure 1.2). Static tests include tension, compression, bending, torsion, and nanoindentation tests, whereas the main dynamic tests are resonant and fatigue tests. All of them will be described in the following sections, with particular attention to the *on-chip* apparatus developed within each category.

1.2.1 Static tests: Tension test

As in usual macroscopic tension tests, the specimen is fixed at one end, while being loaded at the other end by an increasing uniaxial force (figure 1.3) under a displacement control condition. This latter is usually preferred over load condition, because it allows to capture singularities in the specimen characteristic, like necking and softening phenomena.

A lot of information can be derived through this test, like creep, the Pois-

son's ratio, and, above all, the stress-strain curve of the material sample, which, in turn, provides properties, like the Young's modulus, yield and fracture strength.

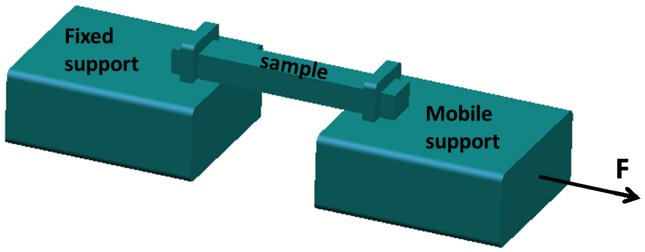

Figure 1.3: Schematic of a tension test

The variety of obtainable information is the main reason why tension test is so common at the macroscale. Similarly, at the microscale, it can be very powerful, too. However, in this case new challenges have to be faced, like for example manipulation and preparation of free-standing and initially stress free specimens. Furthermore, perfect alignment between the sample axis and the load direction is almost impossible to achieve, even with optical microscopes and positioning stages [14], and undesired fracture may occur when mounting and gripping, especially if the material to be tested is brittle.

Besides, these are only general issues, encountered in most of the cases. Then, there are other difficulties related to the specific testing apparatus considered. In fact, during the years many and different arrangements have been designed to perform microtension tests, which differ from one another for sample fabrication, gripping mechanisms, and systems for force and displacement measurements.

First, samples have to be fabricated in order for them to be easily accom-

modated on their testing stage. Thus, several shapes can be found in the literature, each corresponding to a specific apparatus. In fact, there are specimens, where the gage length is enclosed within a frame [15], specimens provided with plates at the ends for gripping purpose [16], bow-tie shaped specimens able to fit into tapered grips [17], specimens cofabricated within the loading structure [18], or separately fabricated, and then picked up and positioned at the right location through a micromanipulator [19]. However, it is quite challenging to pick a single nanosample up and manipulate it correctly, because of adhesion problems. In fact, sometimes electrostatic attraction between the sample and the manipulator probe is not sufficient to move the sample from its original position. Thus, this has to be to welded to the probe tip by some means, like deposition of one or more Platinum thin layers [19].

Gripping can be performed by several means, like frictional [20] or electrostatic attraction, which is particularly powerful at this length scales [21]. Then, glues [22], tapes [23], and connecting rings [24] can be used as well.

Regarding to force measurement, as already said, there are commercial loading cells available, but usually they are not able to provide nanoNewton resolution. Thus, most of the times, researchers build custom-made force transducers, like cantilevers [25], microfabricated frames [26], flexural springs [18], and strain gauges [27].

Similarly, measurement of the stain can be performed through different solutions, like diffracted spots [28], digital image correlation (DIC) [29]-[30], optical encoders [27], Moiré method [31]-[32], electron pattern speckle interferometry [33], or microvernier gages [34].

As said before, one of the main issue, which can compromise the effectiveness of tension tests is the alignment of the sample along the loading

direction, which may introduce bending beyond the desired axial stress, if not properly performed [156]. In order to circumvent such problem, a very interesting solution has been found since the end of the 1990s, with the development of the first generation of *on-chip* testing devices [36]-[37]. These are proper MEMS, which include on the same platform both actuators (for loading) and sensors (for measuring displacements), with a sample directly co-fabricated within all the mechanical parts. Furthermore, they offer the unique advantage of such a small size compatible with the tight chamber of SEM/TEM. Thus, test progress can be observed through real time imaging of the sample deformation, following eventual nucleation and propagation of defects, which can provide insight into fracture mechanisms at such small length scales [38]. In addition, since these devices are proper MEMS, they can be easily fabricated through well-assessed microfabrication processes, and, due to their nature of electromechanical devices, they can allow simultaneous performance of both mechanical and electrical tests [39], to evaluate important electromechanical properties, like piezoresistivity and piezoelectricity.

However, in spite of such advantageous features, they were not ideal testing stages yet. In fact, they could be used only once and required quite sophisticated design and calibration procedures. Then, the variety of materials, which could be tested, was limited to those which could be deposited according to the microfabrication processes, employed for fabrication of the remaining of the device. Thus, 1D nanostructures, like nanotubes and nanowires, were excluded.

In order to overcome such main limitation, new MEMS testing devices are designed in order to accommodate a sample, which can be separately fabricated and then mounted on the chip. This is usually positioned through

high-resolution microscopes combined with nanomanipulators [40], but even with these tools, such operation remains still quite challenging.

On-chip tensile testing devices can differ from each other for design details, but basically all of them consist of an actuator, which can be thermal [41]-[42], electrostatic comb-drive [43], inch-worm [44], or piezoelectric [45], and a sensor, which is now in most of the cases either electrostatic comb-drive based or a simple beam [45].

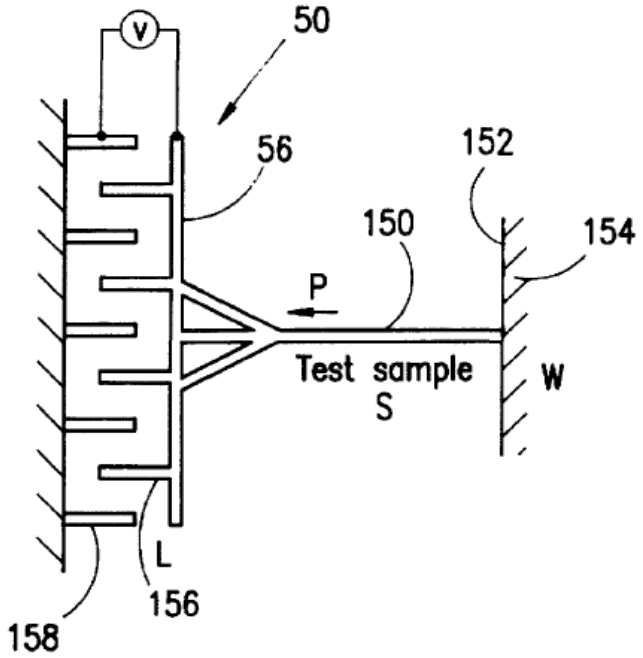

Figure 1.4: Schematic view illustrating an exemplary of the comb-drive unit (156-158), constituting the loading structure. The test sample (150) is a beam fabricated as a part of the loading device (50). It is confined between the wall (152) of the substrate (154) and a trunk (56), which transfers the motion from the comb elements to the sample

The first of these chips to be patented [10] was developed by Saif & McDonald in 1998 [46]. Its structure is quite complex and includes an electrostatic comb-drive actuator, supported by spring-like features, and a sample co-fabricated within the whole device. When the actuator is activated, one end of the sample is pulled accordingly, while the other end is kept fixed to the substrate (figure 1.4). The actuator consists of many parallel plate electrodes, which move apart from each other when biased with a voltage. However, the total electrostatic force they generate is not completely transferred to the sample, since a part of it is absorbed by the springs supporting the actuator electrodes, as a consequence of their elastic deformation. The sample displacement is instead evaluated through the analysis of pictures taken under a microscope during the test.

The main limitation of the present testing procedure is related to the force and strain measurements, which are not independent, and to the small variety of materials to be investigated, since the sample is co-fabricated with the device.

In 2004, Haque & Saif patented their own tensile testing chip, which was suitable for in situ SEM testing, too [47]. In this case the chip is a platform of 10x3 mm^2, including a co-fabricated sample, which is supported at one end by a beam, which behaves as a force sensor, while the other end is supported by an array of transverse beams (figure 1.5).

The platform has a hole for placement of the actuating unit, which pulls the part of the device including the transverse beams. The displacement of the specimen is derived from the displacement of the force sensor (which provides also the acting force when multiplied by its spring constant) minus the displacement of the other end of the sample, known from the relative displacement between a feature connected to the sample and a reference one,

fixed to the substrate. Since the force sensor and these latter features are spatially far from each other, force and displacement measurements cannot be performed simultaneously.

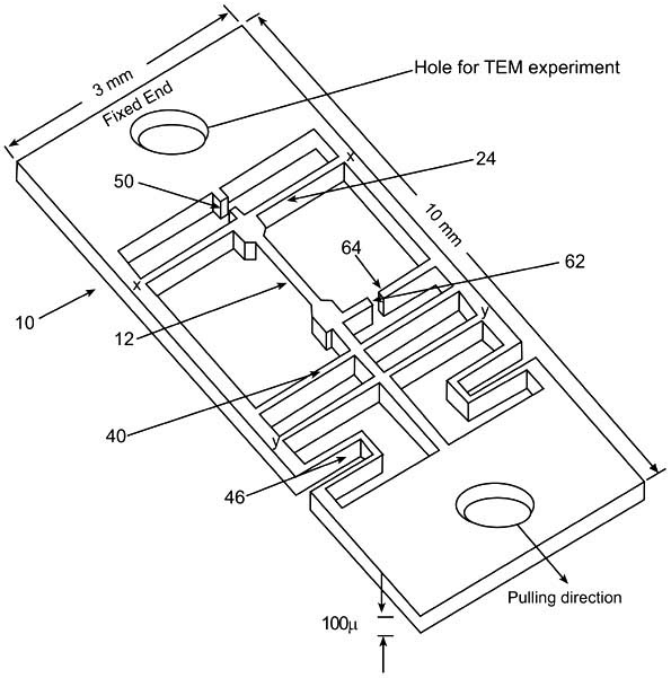

Figure 1.5: Schematic view illustrating the apparatus proposed in [47]. Here, the specimen (12), co-fabricated within the testing chip (10), is supported at one end by a force sensor (24) and at the other end by an array of transverse beams (40). Springs (46) can be employed to provide structural integrity

Recently, this testing device has been further improved in a new design [48]. It still keeps the same shape as before with the force sensor beam. However, now the specimen can be separately fabricated and then mounted between two grooves, which guarantee gripping. Furthermore, in order to perform

high temperature tests, the stage is now fabricated in SiC (Silicon Carbide). Such material has high thermal conductivity together with a high melting temperature (2830°C), thus its mechanical behavior does not change significantly within a wide range of temperatures. Temperature is measured *in situ* by a bimetallic sensor (SiC/Pt) placed upon the sample to be tested. However, this implies that the sample has to be fabricated with such additional structure, which could not be compatible with all kinds of material, thus reducing the application range of the present system.

Another interesting on-chip testing device is the one developed by Espinosa et al. [153], which was the first to provide electrical measurement of the applied load through a capacitive load sensor, while deformation was recorded through SEM images of the sample taken during the test. Such device will be described in detail in the next chapter.

All of the testing systems mentioned above involve the presence of an external structure, and/or electrical signals for loading the samples. On the contrary, the chip reported in [50] exploits a different operating principle. Here, the testing structure is very simple, including a freestanding beam, called actuator, anchored to the substrate at one end, and attached to the sample on the other side. The sample is usually a thin freestanding beam co-fabricated with the actuator, and clamped to the substrate at the opposite side.

The actuator performs both actuating and sensing function. In fact, it is a long slender beam, which, as a consequence of the fabrication process, is affected by residual stress. Upon release, such stress is relaxed, and causes a deformation of the beam (e.g., a contraction if tensile internal stress was present). However, if this is connected to another material beam (e.g., the sample under investigation), the actuator is constrained in its movement,

thus transferring a load to the adjacent beam, as a consequence. The effective magnitude of the applied load depends on the initial internal stress and to the geometry of both the specimen and the actuator. Ideally, by changing the geometry (length and width) of the actuator, a wide range of strain can be applied to the sample. On the contrary, for a fixed geometry, a well defined strain level is imposed, corresponding to a well defined stress condition, which can be evaluated on the basis of some analytical models, as those derived from the Stoney's formula, which is more extensively described in one of the following sections.

Furthermore, many testing structures can be fabricated on the same wafer, each corresponding to a different strain. Thus, from measurement of the displacement undergone by the samples, many stress-strain points can be identified for plotting a stress-strain curve.

The main sources of error affecting the results depend on many factors, like the uncertainty in the knowledge of the geometry, the Young modulus of the actuator, the strain caused by the internal stress in both the sample and actuator after release, and the uncertainty on sample displacement. Nevertheless, due to its simplicity, this is a very interesting testing apparatus, which can be able to perform also combined electromechanical tests [51].

1.2.2 Static tests: Compression test

Compression test at the microscale was performed for the first time in [52], and since then it has been mainly considered to study plasticity [53]. From a technical point of view, compression test is much easier to be carried out than tension test, since sample preparation and gripping are less complex. In fact, the sample (figure 1.6) is usually a micro- or nanopillar (with small

aspect ratio to avoid buckling), fabricated by focused ion beam (FIB), which is anchored to the substrate on one side, while being loaded by a flat head nanoindenter on the other side [54]-[55]. This test is used up to very large strains in order to investigate plasticity and strain hardening response as well.

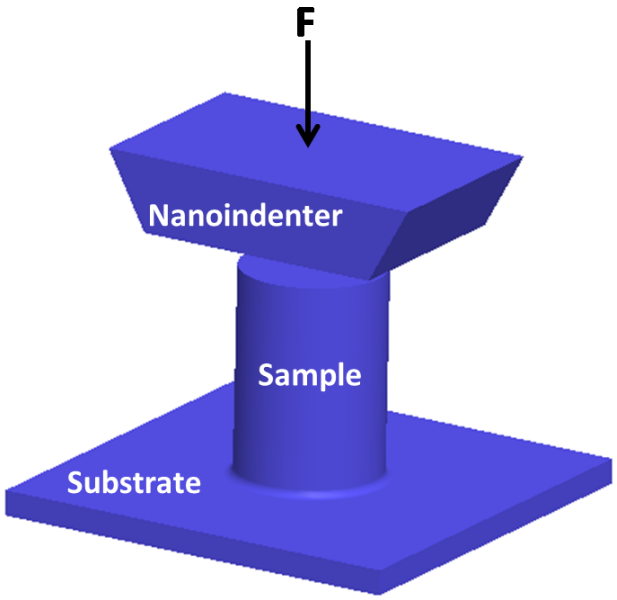

Figure 1.6: Schematic of a compression test

It can also be performed *in situ* a TEM for real time imaging of the sample deformation [56].

In spite of its apparent simplicity, microcompression test has many critical aspects to be considered for its results to be reliable and accurate. In fact, the fillet radius at the bottom of the pillar, where it is anchored, the compliance of the sample base attached to the substrate, load misalignment, and friction between the nanoindenter head and the sample uppermost surface,

are all factors which have to be carefully taken into account, and this can be efficiently accomplished by a numerical study, as reported in [57].
In literature there is only one patented microcompression apparatus, which was proposed in 2008 by Suhir et al. [58]. Their testing system (figure 1.7) was designed to characterize a forest of carbon nanotubes and nanofilaments, grown onto a substrate. In particular, a commercial load cell is used to apply and record the compressive load, while the corresponding displacement is measured through non-contact techniques.

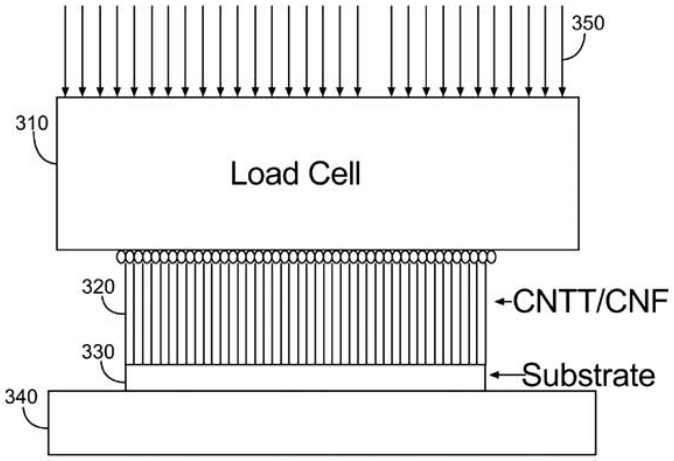

Figure 1.7: Schematic view of the apparatus illustrating the test unit proposed by Suhir et al. [58]. Here, a uniform compressive load (350) is applied on a CNT/CNF array (320), grown on a substrate (330)

The main advantage of such system is the design simplicity, but this is effective to characterize only the global behavior of a forest of samples, while a single nanotube/nanowire cannot be individually tested.

1.2.3 Static tests: Bending tests

A good alternative to tension tests can be offered by bending tests. In fact, they require smaller forces and produce larger displacements. However, a more restricted number of mechanical quantities can be inferred, including residual stress, Young's modulus, and Poisson's ratio. Generally, such mechanical quantities are determined by the use of appropriate models from continuum mechanics, which provide correlation between load/displacement field and the specimen's geometry and mechanical properties. However, in many cases the theoretical boundary conditions, supposed within the models, do not well represent real experiments. Thus, such approximation may cause the corresponding results to be affected by some error.

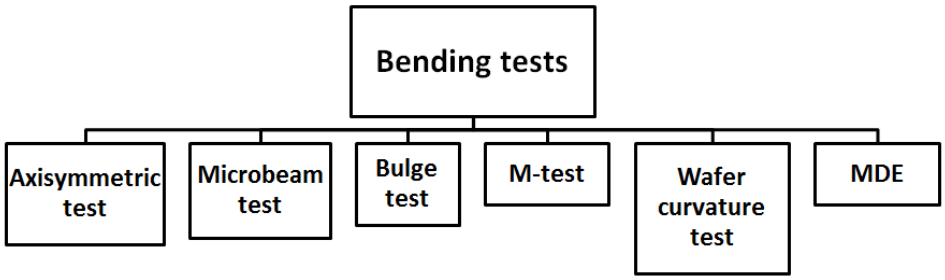

Figure 1.8: Bending tests for mechanical characterization of materials at the micro- and nanoscale

A variety of bending tests can be found in the literature, varying for loading structures, specimen's shape, measurement equipment, and boundary conditions. The main configurations are (figure 1.8): the axisymmetric bending test, the microbeam test, the bulge test, the M-test, the wafer curvature test, the membrane deflection experiment (MDE), and the on-chip bending tests.

Axisymmetric bending test

The axisymmetric bending test is employed to determine the fracture strength of thin circular samples. The specimen is fixed to a hollow cylinder along its periphery and loaded at its center by a spherical indenter (figure 1.9).

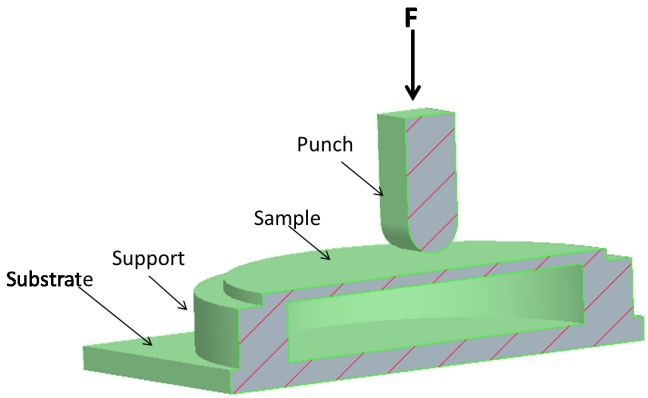

Figure 1.9: Section of the apparatus for axisymmetric bending test

The fracture starts at the opposite side of the loading point. Thus, no local effects influence the experiments.

The fracture stress (σ_F) can be calculated as [59]:

$$\sigma_F = \frac{3P}{4\pi h^2}(1+\nu)\left(\frac{8}{3} + 2\ln\frac{a}{a_1} - 2\ln 2\right) \tag{1.1}$$

where P is the load at fracture, h the sample thickness, ν the Poisson's ratio, a the radius of the support hole, a_1 the radius of the contact area between the spherical probe and the sample.

The main advantage of this test relies on the specimens, which are easy to fabricate. On the contrary, its main limitations are: difficulties for precise positioning of the specimen; uncertainties of the actual boundary conditions; limited number of information obtainable from the test (only the fracture

strength can be evaluated). Maybe for these reasons, this test has been rarely performed, and limited to one material only, which is silicon [60]-[61].

Microbeam test

The specimen is usually a rectangular thin film, loaded by a concentrated bending force, and available in two main configurations: cantilevered (figure 1.10) or clamped at both ends (figure 1.11).

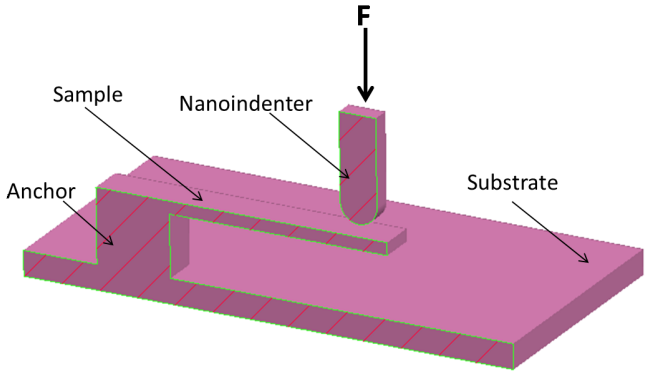

Figure 1.10: Apparatus for a microbeam test, where the specimen is a cantilever

In the fist case, the load is applied at the free end of the sample, whereas in the second case, it is applied at the middle of the specimen span. However, in both cases, the bending force can be generated by an atomic force microscope (AFM) [62], probes attached to a micro-force testing machine [63]-[64], or electrostatic actuation [65]-[66].
This test is usually employed to determine the Young modulus and fracture resistance of the material sample. In particular, these can be derived from analytical models, already included in classical continuum mechanics, which relate elastic properties to geometrical quantities, applied loads, and corre-

sponding displacements.

For example, the Young modulus (E) of a cantilever beam, like the one shown in figure 1.10, can be derived as [59]:

$$E = \frac{4(1-\nu^2)L^3}{bh^3}\frac{P}{\delta} \tag{1.2}$$

where ν is the Poisson's ratio, b and h the length and the width of the cantilever, respectively, h its thickness, P the concentrated bending load, and δ the corresponding transverse displacement.

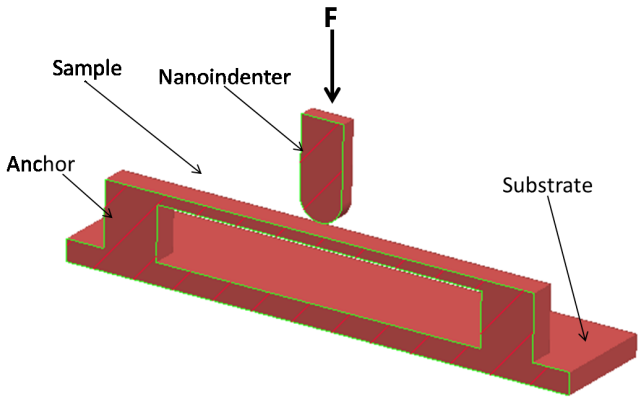

Figure 1.11: Section of the apparatus for a microbeam test, where the specimen is clamped at both ends

While the fracture strength (σ_F) can be computed as [59]:

$$\sigma_F = \frac{6\,L\,P_F}{b\,h^2} \tag{1.3}$$

where P_F is the loading causing fracture.

The main reason why such test is very common is related to the availability of specimens, which can be easily fabricated by standard microfabrication

processes. However, there are also limitations, which especially refer to the boundary conditions. In fact, it is very difficult to reproduce into practical experiments infinitively stiff constraints, which are instead assumed within the analytical models.

Furthermore, the design of the testing stage is not as simple as it may look. In fact, the length of the sample beam plays a key role, since if this is too long, the force required to bend it is small, and thus the device is difficult to calibrate, whereas if the beam is too short, the involved force is higher, but more complex analytical models than the expressions previously reported are required [67].

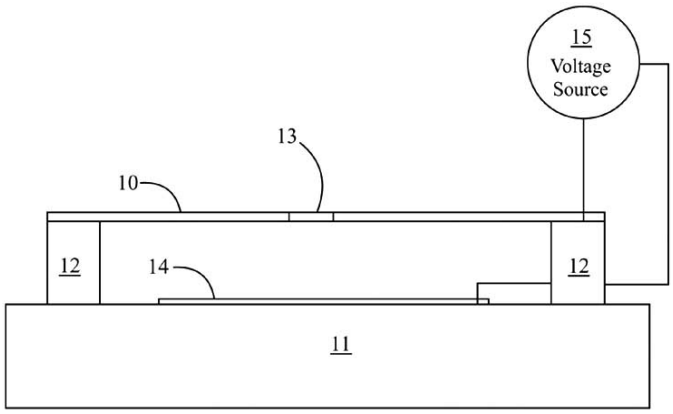

Figure 1.12: Side view of the apparatus proposed by de Boer et al. for material testing at the micro-scale [68]. The apparatus comprises the sample, which is a compliant conductive free-standing membrane (10). A notch is micromachined on the sample (13), in order to introduce a stress concentration region able to trigger failure. The sample is anchored to the substrate (11) through rigid supports (12). A bias voltage (15) is applied between a conductive pad (14) on the substrate and the conductive membrane

In the literature, it is possible to find a couple of microbeam testing apparatus which were patented in the last decade.
In 2002, de Boer et al. reports a simple electromechanical device (figure 1.12), where a thin freestanding membrane is anchored to the substrate at both ends [68]. When applying a voltage between the membrane (e.g., the sample to test) and an electrode placed on the substrate, an electrostatic force is generated, which bends the sample toward it. Furthermore, the sample has a stress concentration region right at the center, in order to increase the magnitude of the acting stress, and study fracture mechanisms.

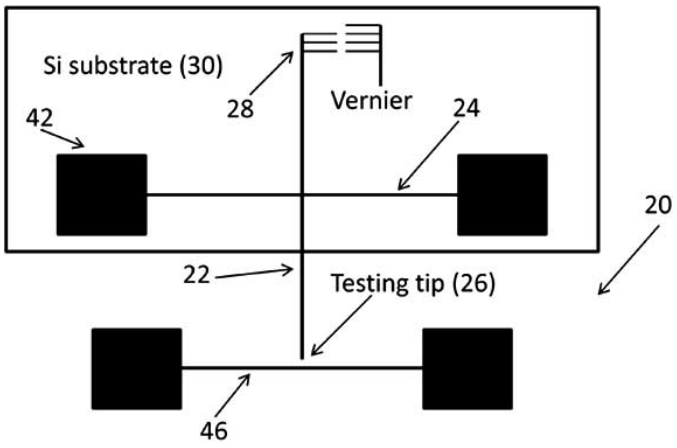

Figure 1.13: Schematic view of the apparatus illustrating the testing chip (20) proposed by Mackin et al. [69]. It comprises a freestanding beam (24), anchored to the substrate (30) at its ends (42) at which a testing probe (22) is attached. The testing probe is provided with a Vernier scale (28) at one end and a testing tip (26) at the other one. This latter can apply a force to the thin film membrane (46) to be tested

The resulting deformation can be measured through non-contact techniques,

while the applied load is known from the bias voltage.

The second example was patented in 2006 by Mackin & Laseman [69]. Here, the sample is a thin membrane fixed at both end, and loaded at the center by a probe attached to a beam which is in turn connected to a fixed-fixed beam, which behaves as a force transducer (figure 1.13). In particular, a piezoelectric actuator moves the beam ending with the probe, thus causing deflection of the sample membrane. Such deflection can be measured by subtracting from the piezoactuator displacement, the deflection of the force transducer, read from the Vernier scale placed at the end of the beam on the opposite side to that of the probe. The displacement of the force transducer can then be converted into force measurement through some non-linear expressions from beam theory.

Bulge test

This test was introduced in 1992 by Vlassax & Nix [70]. It allows for testing of thin membranes (either circular or rectangular), clamped to a supporting frame at its periphery (figure 1.14). The load consists of a pressure field at one side of the membrane, which can be applied by compressed air [71]. This technique has been used to derive mechanical quantities, like the Young modulus, Poisson ratio, and residual stress, by considering some models from continuum mechanics, which relate the mechanical quantities to the applied pressure, the corresponding displacement field (which can be measured by a laser interferometer [71]), and the geometry. For example, in case of a rectangular membrane, pressure (p) and corresponding transverse deflection

(δ) are related as [59]:

$$p = C_1 \frac{h\sigma_R}{a^2}\delta + C_2(\nu)\frac{hE}{a^4}\delta^3 \tag{1.4}$$

where C_1 and $C_2(\nu)$ are constants, which can be determined through FEM analyses, ν is the Poisson's ratio, a half of the length, h the thickness, E the Young modulus, and σ_R the residual stress.

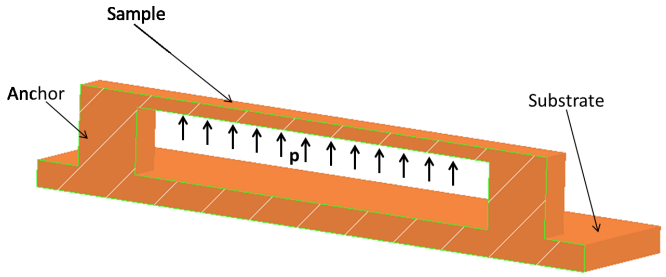

Figure 1.14: Schematic of a bulge test

However, for the analytical models to be valid, ideal boundary conditions have to be reproduced in real experiments. This is very unlike to happen, since the supporting frame has a certain compliance, though. Thus, more accurate analysis would be appropriate, like those supported by FEM modeling. Another inconvenience which may affect the effectiveness of tests is separation of the membrane from the substrate [67], which should instead be avoided. However, in spite of these drawbacks, the bulge test has been extensively applied, and this due to the potential simplicity of the testing procedure and the availability of samples fabricated according to standard microfabrication processes.

M-test

The sample is a freestanding conductive microbeam, which is bent by an increasing electrostatic force until collapse to the substrate (figure 1.15).

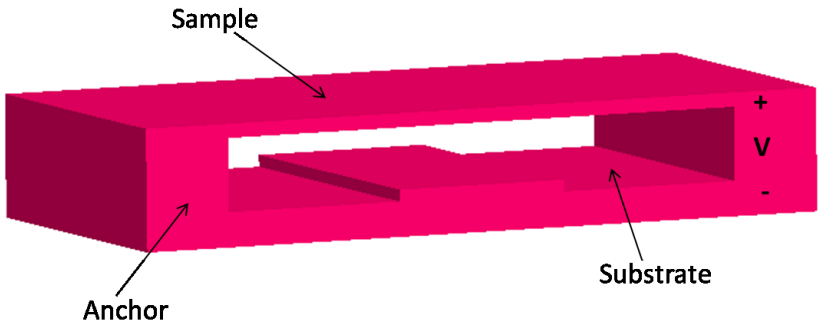

Figure 1.15: Schematic of an m-test

The voltage biasing the beam which causes the collapse is known as pull-in voltage (V). This can be related to the elastic properties and the residual stress of the material sample through simple analytical expressions, which are valid under some assumptions, like infinitely stiff supports and no residual strain [72]:

$$V = \sqrt{\frac{\gamma_1 S}{\epsilon_0 L^2 D_n (1 + \gamma_3 g_0/b)}} \tag{1.5}$$

where ϵ_0 is the air permittivity, g_0 the initial gap between the sample and the electrode on the substrate, b and L the membrane width and length, respectively, γ_1, γ_2, and γ_3 are constants. The other parameters, D and S, are defined as:

$$D = 1 + \frac{2[1 - \cosh(\gamma_2\, kL/2)]}{(\gamma_2\, kL/2)\sinh(\gamma_2\, kL/2)} \tag{1.6}$$

and

$$S = \sigma^*\, h\, g_0^3 \qquad B = E^* h^3 g_0^3 \qquad k = \sqrt{\frac{12S}{B}} \tag{1.7}$$

being $E^* = E/(1-\nu^2)$ for wide beams, while $E^* = E$ for narrow beams, respectively. The effective stress σ^* is zero for cantilever beams, while $\sigma^* = \sigma_R(1-\nu)$ for beams fixed at both ends.
Then, such expressions can be appropriately modified in order to account for non-idealities introduced by the fabrication process [73].
With this test the Young's modulus and the residual stress field are generally derived.

Wafer curvature test

This test is adopted to evaluate the residual stress field inside thin films, deposited onto a thick substrate [74], exploiting an analytical expression which relates it to the curvature of the substrate-thin film system, just induced by the presence of internal stress. Such expression, formulated by Stoney [75], is:

$$\sigma_f = \frac{E_s d_s^2}{6(1-\nu_s)d_f}\Big(\frac{1}{R_{post}} - \frac{1}{R_{pre}}\Big)$$

In the above, E_s and ν_s are the Young modulus and the Poisson ratio of the substrate material, d_s and d_f are the thickness of the substrate and the thin film, respectively; R_{pre} and R_{post} are the wafer curvature before and after deposition, which can be determined by a profilometer.
Such formula is valid if the substrate is much thicker than the thin film, and small deflections are considered. Thus, it can be necessary to introduce a more accurate model for the curvature, in order to expand the application range of the test. For example, the literature provides some extensions of Stoney's formula to discontinuous films and multilayers [76]. However, a limitation which cannot be removed is the inapplicability to evaluate effects of post-deposition processes on released structures, since by definition such

test requires a sample deposited onto a substrate.

Membrane deflection experiment (MDE)

The membrane deflection experiment (MDE) was introduced by Espinosa et al. in 2001 [77]. The specimen is obtained from a Si wafer, which is microfabricated by successive deposition and etching steps, in order to define, as final shape, a thin double dog-bone freestanding membrane, fixed at both ends to the substrate, and spanning a micromachined window beneath (figure 1.16).

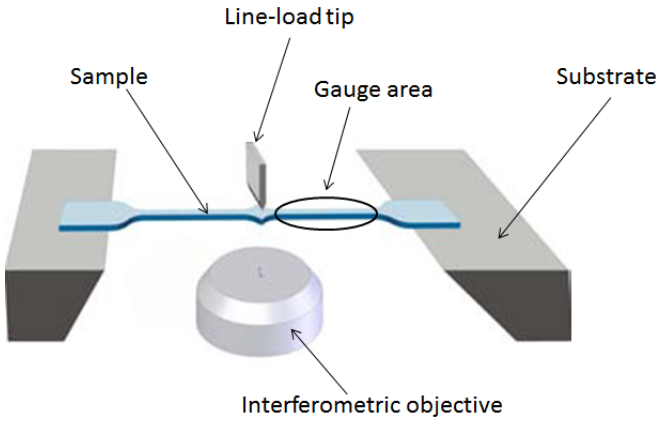

Figure 1.16: Schematic of an MDE

The double dog-bone shape of the membrane is designed in order to avoid stress concentration, thus failure, at either the clamped ends or the center, where the force is applied. In particular, such a transversal force actually results in in-plane tension load in the two narrower regions of the sample, each corresponding to a gage length. Thus, all the advantages of tension tests apply to this test, too.

Load is applied by a nanoindenter with a wedge diamond tip, thus providing

high load and displacement resolution. Then, the membrane displacement can be recorded by a Mirau interferometer and a CCD camera [78], or by the out-of-plane ESPI (electronic speckle pattern interferometer) [79].
This test was used to measure fracture toughness [80] and to characterize the tensile properties (stress-strain curve, yield stress, necking) of thin films. In particular, this was applied to nanomaterials, such as nanocrystalline diamond, amorphous diamond, and single crystal silicon carbide (SiC) films, as well as metals, like gold [81]-[82].

On-chip bending test devices

The literature includes some examples of on-chip bending testing devices, with co-fabricated specimens, as illustrated in [67].
The first of those devices consists of a rigid ring connected to the substrate through two 700 nm thick and 34 μm long specimens. The ring has also twelve protruding freestanding arms, provided with comb-drive elements, which are the electrodes of a parallel plate electrostatic actuator. When a voltage is applied between such electrodes and the corresponding fixed ones, the ring results to be subject to a torque, which corresponds to in-plane bending of the two specimens. These have a trapezoidal cross-section, designed in order to avoid stress-concentration regions, and trigger the failure into a specific portion of the specimen.
The comb-drive structure is used for both actuating and sensing purpose. In fact, from the applied voltage it is possible to derive the corresponding generated force, based on classical electrostatic laws. Furthermore, as the electrodes move, as a consequence of the bias voltage, the capacitance between a pair of fixed and the corresponding moving electrode changes.

Such capacitance change can be measured experimentally, and then related through simple electrostatics laws to the corresponding rotation, generated on the device (which is related to the specimens' displacement). Then, it is necessary to build a 3D numerical model in order to reproduce the experimental condition and identify both the Young modulus and the fracture strength of the specimens.

The second on-chip bending device consists of a freestanding Si square plate, connected to the substrate through a couple of 700 nm thick and 7 μm specimens (at the center) and four springs at the corners. When a voltage is applied between the substrate and the square plate, the specimens are subjected to an out-of-plane bending load. In order to trigger the failure in a central region of the specimens, these have a trapezoidal cross-section.

The square plate is also provided with four rectangular regions, which form with the substrate four capacitive parallel plate sensors. As the device is actuated, the capacitance of such sensor changes, and such change can be related to the corresponding displacements of the specimens.

As before, then FEM simulations are carried out in order to identify the corresponding values for the Young modulus and the fracture strength which allow reproducing the experimental conditions in terms of generated loads and displacements.

The third device was designed to study fracture of 15 μm thick polysilicon samples, provided with an initial notch [67].

Both actuation and sensing are performed electrically by separated comb-drive like units, which are supported by six suspension springs anchored to the substrate. The actuation unit consists of more than 4000 comb-drive elements, while the sensing unit includes 480 comb-drive capacitors, whose capacitance changes as a consequence of the displacement generated by the

actuator. Then, simple electrostatics laws can be used to relate the applied load to the bias voltage, and the capacitance change to the corresponding displacements.

As said, these devices were used to investigate the Young's modulus, the fracture stress, and fracture mechanism of polysilicon thin and thick films, respectively. However, also other materials could be tested, if compatible with the microfabrication process implemented in this design.

The main limitation of these devices is the data reduction method they are coupled with. In fact, such method can be sensitive to fabrication tolerances which can introduce variation in the real structure with respect to the nominal one. If such variations are not included in the analysis, not negligible errors could then be introduced.

1.2.4 Static tests: Torsion test

Few examples of torsion tests are reported in the literature. One of them was carried out in [83]. Here, a specimen with rectangular cross-section is connected at one end to a stage, allowed to rotate, while the other end is fixed. A sensor is mounted on the same stage in order to measure the applied torque, while sample rotation is measured through an optical method. In particular, a laser beam hits the sample, and the corresponding reflected beam is then captured by a diode at a different position, depending on sample rotation. Torque and the corresponding sample rotation depend on many factors, and, in particular, on the shear moduli of its structural material. Thus, known the geometry and other mechanical properties, like the Young modulus, it is possible to build a numerical model of the sample, introducing an initial guess set of shear moduli. Then, these latter are changed in

successive iterations, until the experimental conditions are reproduced (e.g., the sample rotates by the same experimental angle when subjected to the experimental torque). However, since there are two unknowns (e.g., two shear moduli), at least two tests are needed.

Torsion test was applied to isotropic and anisotropic materials, as well as to study plasticity size effects in microwires [84]-[85].

In [36], the authors reported an example of torsion on-chip testing device, which was used to evaluate the maximum shear stress of a single crystal silicon bar.

It includes two parallel plate comb-drive actuators, each with 2000 pairs of interdigitated fixed and moving electrodes. When the actuator is biased, its body moves toward the fixed electrodes. The actuators are designed in order to apply two equal forces, which causes the rotation of a lever attached to the sample, which as a consequence results to be twisted. The sample is a Silicon pillar with square cross-section, cofabricated with the remaining of the device. Its rotation can be read from a Vernier scale placed close to the lever arm, while the torque is the force applied by the actuator (minus the force absorbed by the springs supporting the actuator electrodes) multiplied by the moment arm.

However, torsion test is quite challenging to be implemented and the proposed results are affected by significant uncertainty. Thus, it has not been very common.

1.2.5 Static tests: Nanoindentation

Nanoindentation was developed between the 1970s and the 1980s [86]-[88], but it has attracted increasing attention since 1992, when Oliver and Pharr

proposed an improved analytical method to derive the hardness and the elastic modulus of a material sample from nanoindentation load-penetration curves [89]. Many papers and reviews on this topic can be found in the literature [90]-[92].

One of the main advantage offered by this technique is the easy preparation of samples, if compared to other tests. However, this requires some preliminary knowledge about the material behavior, which has to be either assumed or determined through inverse procedures. In this regard, nanoindentation is less accurate than for example tension and compression test.

Furthermore, it requires complex data reduction, which is typically accomplished by numerical analysis, and the provided results can be affected by errors due to the presence of the necessary substrate supporting the specimen (substrate effect), which have to be taken into account through proper analysis [93]. Thus, neither freestanding samples nor one-dimensional nanostructures, like nanotubes and nanowires, can be tested, but only thin films.

In the literature, it is possible to find two patented nanoindentation testing systems. The first one was proposed in 1999 by Giannakopulos et al. (figure 1.17), and is valid in a wide range of material size from the macro to the nanoscale [94]. As mentioned above, also in this case it is necessary to start from a model to correlate indentation load and depth, which the material sample is expected to follow. Such model can be a power or an exponential law, depending on the indenter (which can have sharp or flat tip), and the Young modulus of the sample, too. Then, experiments provide the real load-penetration curve, which is compared to the guessed one. From such comparison, the Young modulus can be back calculated. The procedure can be automated by the use of a computer, which can control the test and the successive computation operation (figure 1.17).

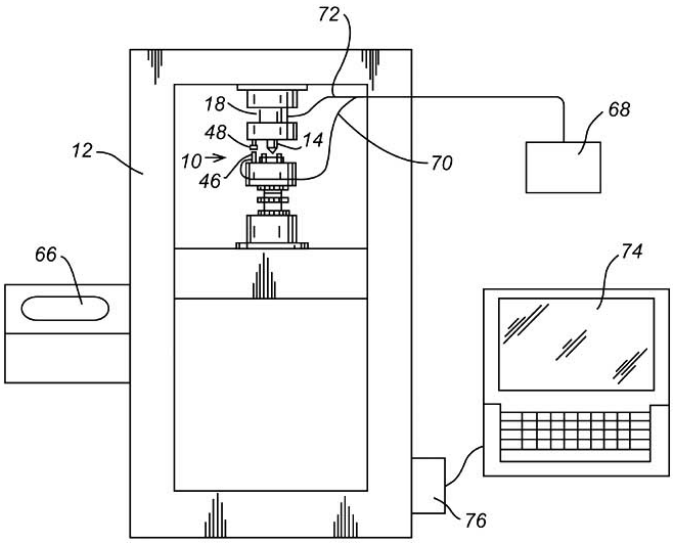

Figure 1.17: Schematic view of the apparatus proposed by Giannakopulos et al. [94]. The indentation apparatus (10) consists of an indenter (14), fastened to a load cell (18), a displacement sensor (46-48). Then, the loading frame (12) can be connected to a control panel (66) to allow for manual control. Automated analysis and test are carried out by the means of a computer (74), connected by an A/D converter (68) and wires (70-72) to the load cell (18) and the displacement sensor (46)

The second nanoindentation testing procedure above mentioned was patented by Suresh et al. in 2001 [95]. It is aimed at determining preexisting stress and stress gradient affecting a material sample before a nanoindentation test. It is based on observing that preexisting stress modifies the indentation area corresponding to a certain load. In particular, in presence of tensile stress, the indentation area is larger than the area when no initial stress applies. Similarly, a compressive initial load causes a smaller inden-

tation area. In order to extract the initial stress field, one set of indentation load-depth-area is required for an initial stress free specimen. Additionally, also some knowledge of the mechanical properties of the material sample is necessary, including the Young modulus and the yield strength.

Different strategies are then available for derivation of the residual stress field. For example, after performance of an indentation test on a stressed region, the following parameters are known: the applied load (P_s), the corresponding indentation area (A_s) and depth (h_s). The average load in the stressed region, P_{ave} can be computed as:

$$P_{ave} = \frac{P_s}{A_s} \tag{1.8}$$

Then, the quantity h_0^2, related to the penetration depth in a stress-free region of the specimen can be calculated as:

$$h_0^2 = P_s\Big\{\sigma_y\Big[1+\frac{\sigma_u}{\sigma_y}\Big]C\Big[1+\ln\Big(\frac{\tan\alpha\, E}{3}\sigma_y\Big)\Big]\Big\} - 1 \tag{1.9}$$

where σ_y, σ_u are the yield and the ultimate strength, respectively, E is the Young modulus, α the indentation angle, and C a constant depending on the indenter.

Then, the ratio R can be found as:

$$R = \frac{h_s^2}{h_0^2} \tag{1.10}$$

Thus, the residual stress, σ_r, can be evaluated from the following expressions:

$$\begin{cases} R &= \dfrac{1}{1+\sin\alpha\,\sigma_r/P_{ave}} & \text{if} \quad R<1, \\ R &= \dfrac{1}{1-\sigma_r/P_{ave}} & \text{if} \quad R>1. \end{cases} \tag{1.11}$$

Some other more complex strategies can be implemented in those cases when the residual stress field is not constant, but varies with depth.

More in general, the experimental load-penetration curves, which can be derived during nanoindentation tests, contain useful information to determine the hardness [96], the residual strains [97], the Young's modulus [98], and the toughness [99] of a variety of materials, including metals, ceramics, polymers, and composites.

1.2.6 Dynamic tests: Fatigue tests

In many integrated circuits and MEMS applications, thin films either free-standing or deposited on a substrate have to withstand cyclic loads, due to intentional vibrations involving the device (like resonators), accidental vibrations due to non ideal environmental conditions (when the device is close to vibrating systems, like air bags in cars), or due to temperature change during their working life.

It is well known that fatigue can modify mechanical properties of materials at the macroscale, and can initiate failure mechanisms. Thus, the knowledge of the fatigue behavior of materials is a key issue for accurate and reliable design. Similarly, at the micro- and nanoscale, for correct functioning of microdevices, it is important to determine how their structural materials behave under cyclic load.

For this reason, in the last decades a significant research work has been aimed at the development of suitable fatigue tests on microsamples to provide insight into fatigue damage mechanisms, fatigue crack initiation and growth. However, because of the different behavior shown by materials at the micro/nanoscale, it may not be a surprise that not only metals [100], but also brittle materials, like silicon, have been tested [67]. In particular, with reference to silicon, this has shown premature fatigue failure, unlike to

its corresponding bulk behavior. Several hypotheses have been formulated in order to explain this, which mainly highlight the key role of oxide layers always covering silicon devices [101]. Microcracks may originate there and propagate under cyclic load until catastrophic failure occurs, and failure conditions were shown to depend on operational environment where the device works. However, further work is still needed to fully explain such mechanisms.

According to the nature of the involved load, fatigue tests can be grouped in two main categories, uniaxial and bending tests, even if during the past other conditions were used [102]. The most common test requires uniaxial cyclic loading, which is more often in tension-tension than tension-compression mode. In fact, this latter configuration can eventually cause buckling [103]. Specific tension-tension apparatus were developed for testing of thin metal wires [103]-[104], either metal [105]-[109] or silicon [110] freestanding films, whereas thin metal films deposited onto a substrate were tested in [111] A typical fatigue test is carried out on a freestanding microbeam, which is excited by dynamic bending under the constant load amplitude control provided by repeated indentation [112]-[113]. In this case, from variation of the beam stiffness, cyclic strain hardening or softening can be captured, as well as observation of fatigue crack growth.

A similar methodology was followed for testing thin films deposited onto a substrate, under tension-compression loading [114]. Bending methods based on monitoring of the resonant frequencies of microsamples are also available, and they were adopted for characterization of either thin films or multilayers [115]-[116]. However, in this case, fatigue failure is supposed to occur when a reduction of 10 Hz in the resonant frequency is recorded, corresponding to development of cracks already above a certain size.

Another common fatigue test involves thermal loading. In this case, the sample is a thin metal film bonded to a silicon substrate. A current flowing inside the metal generates heat by Joule effect, corresponding to temperature increase. Since the metallic sample and the substrate have different thermal expansion coefficient, a thermal stress is induced within the sample. If the flowing current is AC, also the corresponding mechanical stress is cyclic, too. With respect to mechanical bending and uniaxial cyclic loading, thermal loading has the advantage of not requiring actuating structures, but only a couple of electrodes. This means that this test can be performed *in situ* electronic microscopes, and can easily extended to a wide range of frequency, depending on the frequency of the AC current. On the other hand, it is intrinsic to the thermal technique that only metallic and not freestanding samples, but bonded to a substrate, can be tested. However, the main limitation of such test is the existing relationship between temperature and strain, which cannot be varied independently. In fact, the strain is the result of the temperature increase and the difference between the thermal expansion coefficient of the involved materials. Furthermore, it is not possible to monitor the stress inside the sample. Therefore, the test is performed under strain control, and the corresponding stress is derived from a stress-strain curve independently determined by other techniques, like the wafer curvature test. Thus, cyclic hardening or softening cannot be evaluated [117].
All of the aforementioned tests and those presented in [118]-[122], [123], require external macroscopic actuating and sensing systems for application of loads and sensing of strains, respectively. However, in literature it is possible to find some examples of on-chip fatigue testing devices. They are usually actuated by appropriate comb-drive structures [43], [101], under uniaxial [43] or bending cyclic loading [101]. In particular, the first testing device

[43] consists of a parallel plate actuator, where attached one end of the sample, being the other end fixed to the substrate. When the actuator is biased with a voltage, the actuator pulls the specimen, whose displacement can be read from a Vernier scale. The actuator has also a sensing function, since it is relatively compliant, thus for the same voltage the delivered displacement is different when there is a sample mounted. On converting the voltage into force, and subtracting, for a given displacement, the force with no sample mounted from the force with sample, it is possible to identify the force needed to deform the sample.

The second device has a more complex structure [101]. It consists of a Silicon rotational mass, ending with a beam, which is the sample to test. This is fabricated with usual microfabrication processes, and results with a notch for stress concentration. The rotational mass is provided at opposite sides with electrostatic comb-drive elements, with either actuating or sensing function. When biasing the comb-drive fingers on one side with an AC voltage, the mass starts oscillating, and, in test condition, it is excited to vibrate at resonance. As the mass moves, the capacitance on the comb-drive elements on the other side changes. Such variation can be detected through proper circuitry and then converted into displacement measurement. From a FEM analysis, the displacement field on the sample can be converted into stress field, while assuming a linear elastic characteristic. In this way, it is possible to monitor how stress varies with the number of cycles, even if the assumption of linear-elastic behavior is reasonable only for brittle materials, like Silicon.

1.2.7 Dynamic tests: Resonant tests

Resonant tests are typical non-destructive tests, which allow for evaluation of the elastic properties and residual stresses of the sample from measurement of its resonant frequencies.

Common samples which can be tested have usually the shape of micro- and nanobeams [124]-[185], square or circular thin plates [128]-[129], or supported thin films [130].

All of the resonant techniques are based on analytical or semianalytical models, which relate the geometry, the mass, the residual stress field, and the mechanical properties of the specimen to its resonance frequencies.

In particular, the Young's modulus or the residual stresses can be derived from the first resonant frequency of a cantilever [131]-[134] or a beam simply supported at both ends [135].

In fact, the fundamental resonant frequency of a cantilever beam can be expressed as [59]:

$$f = 0.1 \frac{h}{L^2} \sqrt{\frac{E}{\rho}} \tag{1.12}$$

where h and L are the thickness and the length of the beam, respectively, E the Young modulus, and ρ the density. For a beam simply supported at both ends, its first resonant frequency is related to both the Young modulus and the residual stress (σ_r) as [59]:

$$f = \frac{\pi}{2\sqrt{12}} \frac{h}{L^2} \sqrt{\frac{E}{\rho}} \left[\sqrt{1 + \frac{12\,\sigma_r\,L^2}{\pi^2\,E\,h^2}} \right] \tag{1.13}$$

Simultaneous determination of both the Young's modulus and the residual stresses can be accomplished from tests on beams clamped at both ends [125]. Two resonant frequencies of circular or square plates with free boundary conditions are instead necessary for determination of the Young's modu-

lus and the Poisson's ratio [128]-[129]. At least, twenty resonant frequencies are required for determination of the anisotropic elastic constants of thin films deposited onto a substrate by the resonant ultrasound spectroscopy (RUS) [130].

The main source of errors affecting resonant techniques are related to uncertainties in the geometry of the samples, as well as to the compliance of real supports, which are not ideal as supposed in the analytical or semianalytical models. Furthermore, on conducting tests in air, additional dissipative phenomena can introduce shifts in the resonant frequencies of microfabricated structures.

A typical dissipative phenomenon affecting the dynamic performance of MEMS devices, like those for carrying out resonant tests, is *squeeze-film air damping* [136]-[137]. This occurs each time a thin layer of fluid (smaller than one third of the confining surface) is confined between two solid surfaces, provided with relative movement. In particular, when one plate comes closer to the other or move apart, the thin layer of air is pulled out/sucked into its small channel, and an even significant pressure field arises into the fluid. This then generates a resistive force acting against the moving surface, causing damping. However, such problem is avoided if the test is carried out in vacuum.

In the literature, it is possible to find a patented resonant testing apparatus. This was proposed in 2007 by Kothari et al. (figure 1.18) to determine the residual stress in thin membranes of devices for displaying images, and in general it can be applied to MEMS provided with structures similar to those used herein as interferometric units [138]. An exemplary unit comprises a reflective deformable membrane (14a/14b), attached to the substrate. The cavity is then bounded by the movable membrane and a partially reflective

optical stack (16a/16b).

If no residual stress is present, the resonant frequency of the thin membrane can be evaluated according to previous equation (1.12). Otherwise, it is given by previous equation (1.13).

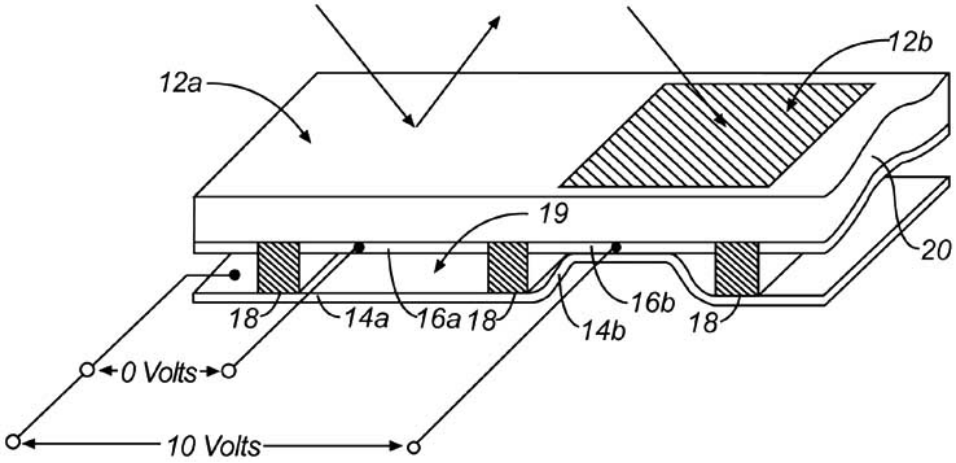

Figure 1.18: Schematic view of the apparatus illustrating the test unit proposed by Kothari et al. [138]. It consists of an interferometric modulator (12a/12b), having a partially reflective optical and conductive stack (16a/16b) and a movable reflective membrane (14a/14b).

The resonant frequency can be detected when applying an AC voltage between the optical conductive stuck and the membrane, which is allowed to vibrate. By varying the frequency of the bias voltage, the resonant frequency can be identified when high oscillations occur. Then, from the knowledge of the membrane geometry (which should be carefully determined, in order to minimize the errors on the final results), the residual stress can be derived. Alternatively, another method is presented. This is based on observing that

residual stresses causes deformation of the membrane, thus modifying the gap thickness of the interferometric cavity. Since the color of the reflected light depends on the optical path (e.g., gap thickness) of the incident light, such color changes with respect to the expected one by design. Thus, from the color of the reflected light, the gap thickness, and finally, the entity of the residual stress inside the membrane can be evaluated.

To the class of resonant tests belong also many techniques based on the use of the atomic force microscope (AFM). One of the most popular is the atomic force acoustic microscopy (AFAM). Its basic principle is related to the observation that the resonant frequencies of the AFM cantilever change when its tip is brought into contact with a sample surface [67]. Through appropriate analytical models those frequencies can be related to the sample-tip coupling, which is generally modeled as a spring [139]. Thus, from the stiffness of such spring, mechanical properties of the sample, like its Young's modulus [140]-[141], can be derived. Samples, which can be tested, are both thin films [142] and nanowires [143].

1.2.8 Other techniques

Beyond the above mentioned techniques, the literature offers examples of other testing systems for mechanical characterization of micro- and nanosamples, like fracture testing systems [144], hole drilling [145], and Raman spectroscopy [59] based methods.

With reference to fracture tests, there are two interesting on-chip devices, which were proposed for quantification of the fracture toughness of silicon. The first one [144] is a simple silicon structure consisting of a silicon free-standing beam (e. g., the sample) anchored to the substrate at both ends.

By the means of an indenter a small initial crack is introduced inside the sample, which is also subject to some residual stress induced by the fabrication process. Upon release of the beam, the residual stress is relaxed, causing opening of the crack, whose initial size and position are known from measurement through an SEM.

The magnitude of the residual stress (e.g., the stress on the sample) is measured through a separate testing structure, and then, a numerical analysis is carried out in order to determine the corresponding stress intensity factor on the sample for those initial crack length and position. Many of these experiments can then be simultaneously performed, varying the length of the crack, in order to estimate the critical stress intensity factor (e.g., toughness) of the material sample.

The second testing system was the third device presented in the previous section about the on-chip bending systems [67]. The only difference is that in this case the specimen has an initial crack generated by the head of an indenter.

Compared to the fracture chip previously described, the load is not applied through relaxation of residual stress, but through an electrostatic actuator. Thus, the stress can be varied, and in particular increased until the crack propagates, triggering dynamic failure of the sample. In this condition, the corresponding stress intensity factor reaches its critical value, which can thus be identified.

An alternative method which allows for a simultaneous determination of both the Young modulus and the Poisson ratio is the hole method [145]. It is based on the introduction of a relatively small hole inside the testing structure. Then, analytical expressions already included in classical mechanics can be considered for derivation of the displacement field near the hole,

when applying a uniaxial load sufficiently far from the singularity region. The displacement is a function of the magnitude of the applied load, as well as of the geometry and the mechanical properties (e.g., Young modulus and Poisson ratio) of the material sample. Thus, with an inverse procedure, the Young modulus and the Poisson ratio can be derived from accurate measurement of the geometry and displacement field. In particular, this latter can be evaluated through a non-contact method, like Digital Image Correlation (DIC), which can determine the relative displacement of a sample area between pictures taken before and after loading. Such procedure guarantees high displacement resolution (1-2 nm), which is of fundamental importance in order to derive reliable results.

Furthermore, the hole method can be applied to test samples with even complex geometry, if a more accurate FEM analysis is adopted to relate the elastic constants to the displacement field. However, the area on the sample where to measure the displacements has to be carefully chosen, in order to provide a significant number of points, which undergo relatively significant displacement, otherwise the extraction of the mechanical constants is not effective.

The last method which is worthy to be mentioned is based on Raman spectroscopy. Such methodology allows for evaluation of the residual stress field inside material samples [146]-[147]. In fact, the Raman spectrum of a sample shows a peak which is shifted when residual stress is present. However, in order to use such technique, it is necessary that the stress state is simple and its form already known. Then, from the peak shift, its magnitude can be evaluated.

1.3 Research trends on mechanical characterization of materials at the micro- and nanoscale

During the last decades, the aforementioned methodologies have been employed with different intensity to test a variety of materials, depending on the time frame. Thus, the following two sections are aimed at showing how the interest of the scientific community has been addressed toward each testing methodology and material class with time. This will be accomplished through some figures reported in [9], which were obtained from consulting hundreds of papers published in the main international journals since the 1950s.

1.3.1 Testing methodologies

In the previous sections, advantages, disadvantages, and application of the main methodologies for mechanical characterization of materials at the micro- and nanoscale were presented. Figure 1.19 summaries such description, reporting what are the mechanical quantities each method is suitable to determine (where the symbol x confirms suitability to determine a specific quantity), while the pie chart in figure 1.20 provides information about how often each of them has been preferred with respect to the others. From such chart, the tension test results to be the most frequently employed. This should not be a surprise, since it is the most versatile technique, allowing for determination of many mechanical properties, including the Young modulus, the yield and fracture stress (figure 1.19). In fact, it provides complete characterization of materials through their full stress-strain curve, and information about their plastic deformation and creep. Furthermore, both micro- and nanosamples of a variety of materials, including freestanding films and

nanowires, can be tested.

TEST			IDENTIFIABLE QUANTITY						
			Young's modulus	Poisson's ratio	Shear modulus	Yield strength	Fracture strength	Creep	Residual stress
Tension			X	-	-	X	X	X	-
Compression			X	-	-	X	-	-	-
Bending	Axisymmetric		X	-	-	-	X	-	-
	Bulge		X	X	-	X	X	-	X
	MDE		X	-	-	X	X*	-	X
	Microbeam		X	-	-	-	X	-	X
	M-test		X	-	-	-	-	-	X
	Wafer curvature		-	-	-	-	-	-	X
Torsion			-	-	X	-	-	-	-
Nanoindentation			X	-		-	-	X	X
Resonant	Sonic	beams	X	-	-	-	-	-	X
		plates or fims	X	X	-	-	-	-	-
	RUS		X	X	-	-	-	-	-
	AFAM		X			-	-	-	-

		S-N curves	Fatigue damage	Crack growth rate
Fatigue	Uniaxial tension	X	X	X
	Bending	X	X	X
	Thermal	X	X	X

(*) Can also identify fracture toughness

Figure 1.19: Mechanical quantities of materials at small length scales which can be determined with different techniques

However, in spite of the intense work already done, still today there are neither standardized guidelines nor universal equipment to refer to. Thus, every researcher has been developing his own testing apparatus, and convergence toward a unified methodology seems to be still far.

As mentioned in the previous sections, the most promising configuration is provided by on-chip testing devices. These, in fact, have sufficiently small size to be placed inside the chamber of electron microscopes (SEM/TEM), allowing for real time imaging of the sample deformation. Furthermore, these are electromechanical systems, thus they give the possibility to per-

form combined mechanical and electrical tests, useful to investigate material properties like piezoresistivity and piezoelectricity.
However, on developing an effective on-chip tensile testing device, many challenges have to be faced, which in general include a quite sophisticated design, as well as a complex experimental setup.

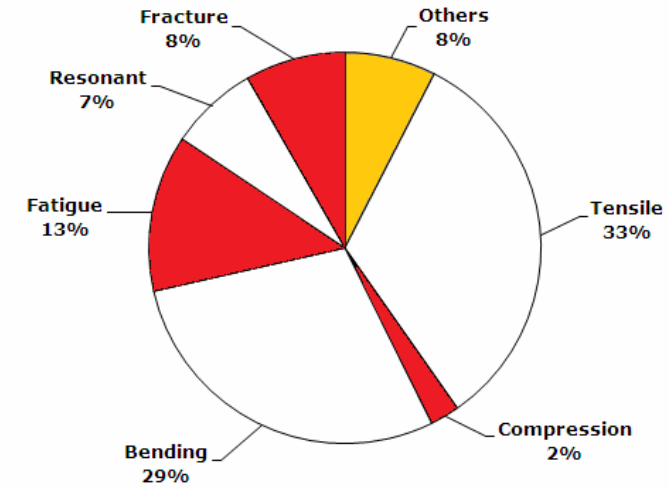

Figure 1.20: Testing methodologies for mechanical characterization of materials at the micro- and nanoscale

The second main class of tests is represented by bending tests. They are relatively easier to perform than tensile tests, but each of them provides a limited number of mechanical properties (figure 1.19). Among them, the most versatile is the bulge test, which can give information about the Young's modulus, the Poisson's ratio, the yield and the fracture strengths, and the residual stresses. Other configurations, like the axisymmetic, M-test, and wafer curvature test have been less considered.
Dynamic tests have been extensively employed (figure 1.20), too. Those in-

clude fatigue tests, which have gained increasing attention for investigation of both metallic and ceramic micro- and nanosamples (as later shown in figure 1.23), in order to derive S-N curves (stress versus number of cycles to failure), and give insight into the mechanisms of fatigue damage, fatigue crack initiation, and growth.

Resonant tests prevail as an alternative to static tests for determining the Young's modulus and residual stresses of a wide range of material samples with different geometries. In particular, resonant tests can be preferred over bending wafer tests, like the wafer curvature method, since they can determine residual stresses affecting samples after release [132].

Beyond the aforementioned testing methods, there are others, like compression, fracture mechanics, Raman spectroscopy for residual stress measurement, hole drilling for measurement of the isotropic elastic constants. However, they have been poorly applied, because of either the limited number of information they provide or the complexity of the apparatus they require.

In figure 1.20 (as following figures 1.21, 1.22, and 1.23) nanoindentation is not considered, because of the great number of works published on its applications, which could cause undervaluation of other important techniques, like tension and bending tests.

1.3.2 Tested materials

During the years, different techniques have been adopted to test a variety of materials, including metals, ceramics, and polymers (figure 1.21). The most common are silicon, silicides, copper, nickel, and aluminum (figure 1.23). In particular, silicon (both single and polycrystalline) and its compounds (silicon oxide and silicides, like silicon carbide and silicon nitride) have been

the most intensively studied, since they are still today the basic materials for fabrication of microdevices (figure 1.21). However, also metals have attracted general attention, followed by carbon (in the shape of nanotubes), polymers and other materials, like Gallium Nitride (GaN) and Zinc Oxide (ZnO) nanowires.

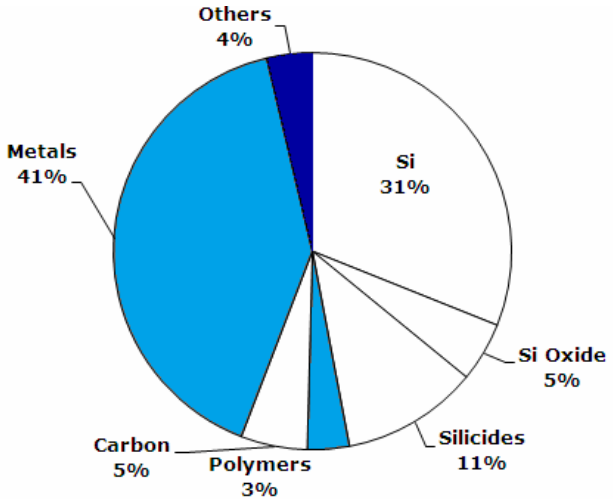

Figure 1.21: Materials tested at the micro- and nanoscale

With reference to how interest on materials changed with time, figure 1.22 shows the percentage of papers reporting tests on a specific material from 1950 to 2010. From this, it can be verified that silicon and its compounds have always surpassed the interest toward other materials. However, as the importance of metals in MEMS design is increasing, because for example the application of metal nanowires as interconnects, the number of studies about their characterization at the micro- and nanoscale is increasing accordingly. Also the interest about new materials, like silicon carbide (SiC) and amorphous nanocrystalline diamond can be noted, as well as that about

carbon nanotubes.

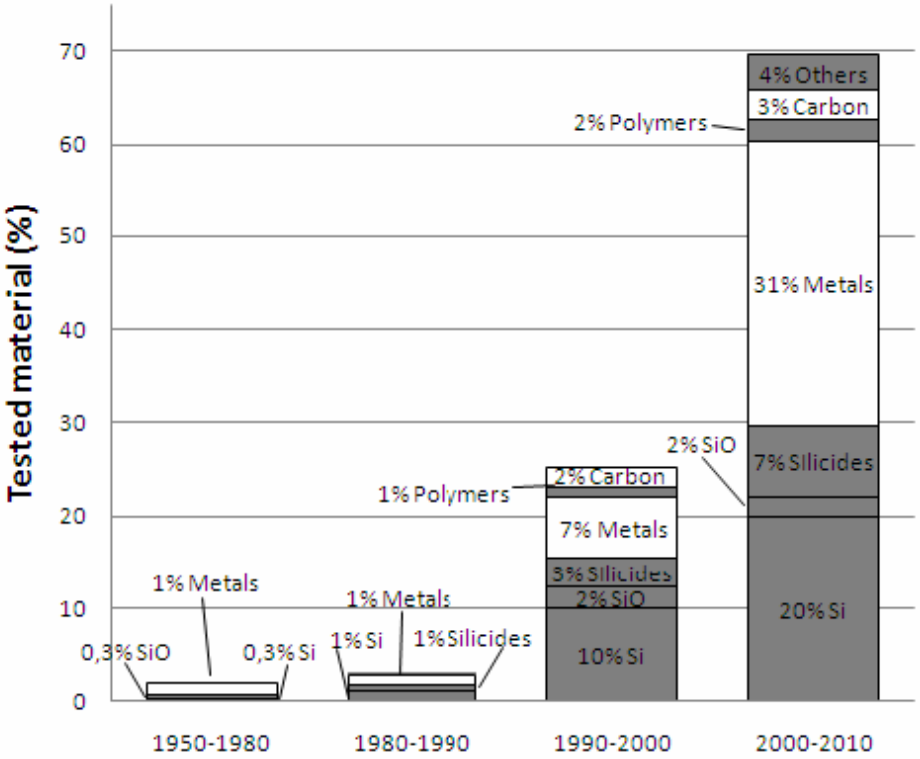

Figure 1.22: Materials tested at the micro- and nanoscale

They were first grown in the 1990s, and have soon attracted significant interest, due to their excellent electrical, thermal, and mechanical properties, which make them a good alternative to traditional materials.

TEST		MATERIAL				LENGTH SCALE	
		Ceramic (Silicides)	Metals	Polymers	Others	Micro	Nano
Tension		Si SiC SiN SiO_2	Au Al Cu Ag TiN	Epoclad Epoxy PAN	SiGe CNT ZnO DNA GaN	x	x
Compression		Si	Mg Au Mo TiAl Ni	-	-	x	x
Bending	Axisymmetric	Si	-	-	-	x	-
	Bulge	Si SiN	Au Al W Cu	-	-	x	x
	MDE	SiC	Au Al Cu	-	Nanocrystalline diamond Amorphous-tetahedra diamond	x	-
	Microbeam	Si SiN	Cu Ni Au	-	CNT ZnO GaN	x	x
	M-Test	Si	Au	-	-	x	-
	Wafer Curvature	SiC	Ni Al	-	-	x	x
Torsion		Si	Ni NiFe Cu	-	-	x	-
Nanoindentation		Si SiC	W TiNi Al Steel Cu TiN	✓	SiGe C	x	x
Resonant	Microbeam	Si SiC	Au Ni	Polymide	GaN ZnO	x	x
	Thin film	Si	Cu		CVD	x	-
	AFAM	Si	Ni	-	-	x	x
Fatigue	Uniaxial	Si	Cu Al Ni NiCo	-	Collagen	x	x
	Bending	Si SiN	Steel	-	-	x	-
	Thermal	-	Cu	-	-	x	-

Figure 1.23: Materials tested at the micro- and nanoscale

Chapter 2

Development of a novel microelectromechanical system (MEMS) for mechanical testing of nanostructures

2.1 Typical stability problems of tensile testing devices

As stated in the previous chapter, MEMS-based mechanical testing systems are very powerful instruments for investigation of materials behavior at the micro/nanoscale. In fact, due to their small size, they can be combined with electron microscopy for real time observation of the sample deformation,

providing qualitative information about defect nucleation and propagation [148]. Furthermore, being electronic devices, they can carry out signals, containing quantitative information about loads and strains.
The typical structure of tensile testing devices includes three main parts:

- An actuator. This is the element which applies loads/displacements to the specimen during the test;
- A load sensor. This is the sensing part of the device, which has to provide information about the load applied to the sample;
- A sample. This is mounted across the gap which separates the actuator from the load sensor. The sample can be co-fabricated within the whole device, or fabricated apart and then mounted by the means of a manipulator.

In a usual design, the load sensor is a flexible structure, connected to the sample as springs in series. During a test, the actuator pulls the specimen, which transfers part of the delivered displacement to the load sensor. As a consequence, this latter undergoes a deformation, which can be measured either electronically or from analysis of successive pictures taken during the test. Such displacement can then be multiplied by the previously calibrated spring constant of the load sensor, in order to derive the applied load, which is the same for both the sensor and the specimen.
In order to increase the sensitivity of the load measurement, the sensor stiffness should be as smaller as possible, thus generating relatively high displacements in correspondence of even small loads. However, if the stiffness of the sensor is too low compared to the one of the specimen, then most of the displacement delivered by the actuator is transferred to the sensor, causing

a small deformation of the specimen. Thus, such parameter plays a major role, and a trade-off value has to be chosen.

When the load sensor moves along with the sample, it accumulates elastic energy, becoming potential source of instability. In fact, such energy is released when the force transmitted by the sample to the load sensor starts decreasing after some strain has been applied. This means that the load sensor comes back to its initial position, pulling the end of the specimen attached to it [149]. In such situation, the displacement-control condition is no longer guaranteed, and dynamic failure of the specimen may occur.

2.2 Analytical modeling of stability in typical tensile testing devices

In order to have a deeper understanding of the conditions generating instability, it is useful to study the equilibrium of the device from the point of view of the load sensor.

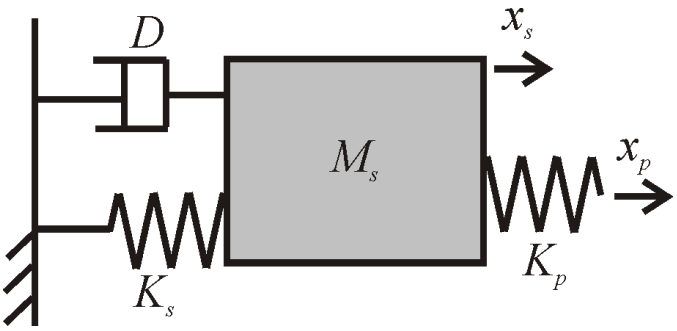

Figure 2.1: Lumped parameters model of a typical tensile testing device

The approach which is developed herein follows the one shown in [150] to explain stability in MEMS electrostatic-elastic systems.

For simplicity, the device can be studied through the lumped parameters model reported in figure 2.1, where the sample is represented by a spring, with spring constant k_p (its mass is negligible with respect to the one of the load sensor) and the load sensor by a mass (M_s) connected to the substrate through a damper (with damping constant D) and a spring (with spring constant k_s). The sample undergoes a displacement x_p, which is known, since the test is performed under displacement control. Such displacement is in general different from the displacement x_s characterizing the load sensor. For this latter to be at equilibrium, the sum of the forces acting on it has to respect the second Newton law:

$$M_s \frac{d^2 x_s}{dt^2} = \sum_i F_i \tag{2.1}$$

where F_i is the i-th force acting on the load sensor. In this case, there are three forces: 1) the elastic force transmitted to the load sensor by the sample (F_P); 2) the elastic force exerted by the load sensor spring (F_s); 3) the damping force (F_D). These forces can be written as:

$$F_p = k_p(x_p - x_s) \tag{2.2}$$

$$F_s = -k_s x_s \tag{2.3}$$

$$F_D = -D \frac{dx_s}{dt} \tag{2.4}$$

Thus, the 2.1 can be rewritten as:

$$M_s \frac{d^2 x_s}{dt^2} = -D \frac{dx_s}{dt} - k_s x_s + k_p(x_p - x_s) \tag{2.5}$$

In general, $x_p = x_p(t)$. However, first the steady-state solutions of the equilibrium equation can be considered. Thus,

$$x_p = \text{const.}_1$$

$$x_s = \text{const.}_2$$
$$\frac{dx_s}{dt} = 0$$
$$\frac{d^2x_s}{dt^2} = 0$$

Then, the 2.5 simplifies as:

$$-k_s x_s + k_p(x_p - x_s) = 0 \tag{2.6}$$

Here, it is possible to divide by $k_s \cdot x_p$, in order to get:

$$-\frac{x_s}{x_p} + \frac{k_p}{k_s}\Big(1 - \frac{x_s}{x_p}\Big) = 0 \tag{2.7}$$

which can be rewritten as:

$$-\frac{x_s}{x_p}\Big(1 + \frac{k_p}{k_s}\Big) + \frac{k_p}{k_s} = 0 \tag{2.8}$$

Thus, the solutions of such equation are the roots of the function $f(x_s/x_p)$, defined as:

$$f\Big(\frac{x_s}{x_p}\Big) = -\frac{x_s}{x_p}\Big(1 + \frac{k_p}{k_s}\Big) + \frac{k_p}{k_s}$$

Figure 2.2 plots $f(x_s/x_p)$ as a function of x_s/x_p for different values of k_p/k_s. In particular, only the range with physical meaning $-1 < x_s/x_p < 1$ is considered herein. From the figure, it results that $f(x_s/x_p)$ has a root (e.g., equilibrium is always achievable) only for $k_p/k_s > -1$, while $k_p/k_s = -1$ is a sort of critical value which changes the slope of the curve.

It is now interesting to evaluate the stability of the equilibrium positions at varying k_p/k_s. For simplicity, here the inertial term can be neglected. Then, the equilibrium equation 2.5 becomes:

$$D\frac{dx_s}{dt} = -k_s x_s + k_p(x_p - x_s) \tag{2.9}$$

or,

$$\frac{D}{k_s \cdot x_p}\frac{dx_s}{dt} = f(x_s/x_p) \tag{2.10}$$

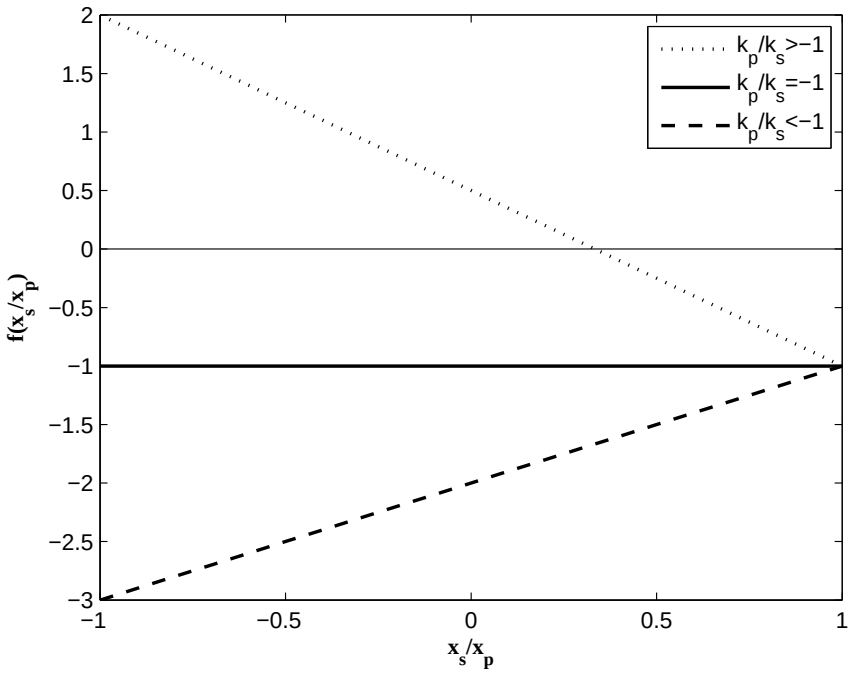

Figure 2.2: The function $f(x_s/x_p)$ versus x_s/x_p for different values of k_p/k_s

This means that except for a constant, the derivative of the load sensor displacement with respect to time is equal to the function $f(x_s/x_p)$. Now, it is useful to still refer to figure 2.2. In fact, first suppose that there is equilibrium and a small perturbation is applied moving the system to the left of the equilibrium point. If $k_p/k_s > -1$, then $dx_s/dt = f(x_s/x_p) > 0$, which means that x_s tends to increase, coming back toward the previous equilibrium position. On the contrary, if a small perturbation is applied moving the system

to the right of the equilibrium point, then $dx_s/dt = f(x_s/x_p) < 0$. Thus, x_s tends to decrease, coming back to the previous position. As a consequence, when $k_p/k_s > -1$, the system reacts against small perturbation of the equilibrium position, in order to come back toward it. A further confirmation for this comes from the solution of the previous differential equation 2.9, which shows the evolution of x_s with time for a fixed x_p. It emerges that when $k_p/k_s > -1$, after a transient, the system reaches a stable position (x_s remains steady with time). Otherwise, for $k_p/k_s < -1$, x_s cannot reach a steady position (figure 2.3).

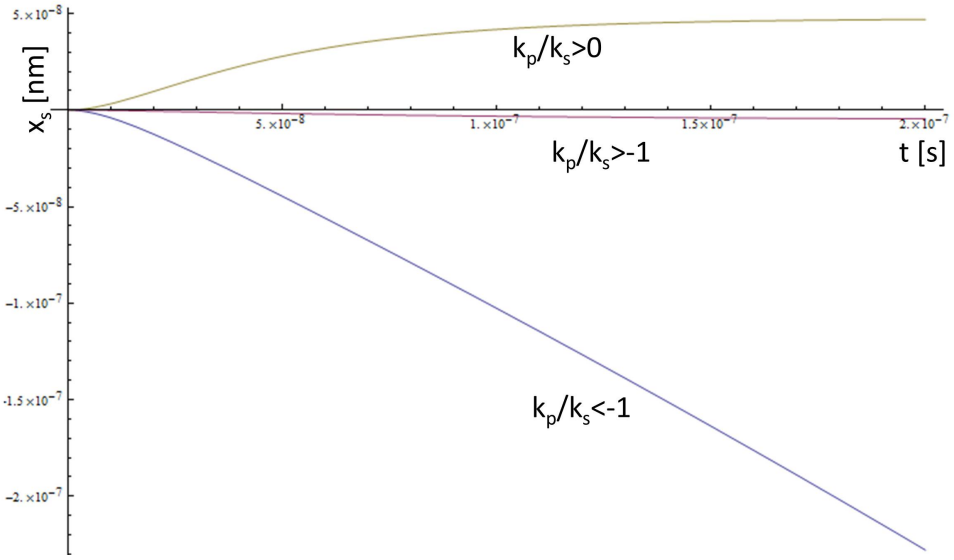

Figure 2.3: Time evolution of x_s for different values of k_p/k_s

This discussion is useful to highlight the importance of the load sensor stiffness which plays a role on determining the stability of the system.
In order to consider a more realistic case, the sample is now modeled though a non linear spring, whose characteristic can be written as:

$F_p = k_0(x_p - x_s) + k_1(x_p - x_s)^3$ (figure 2.4).

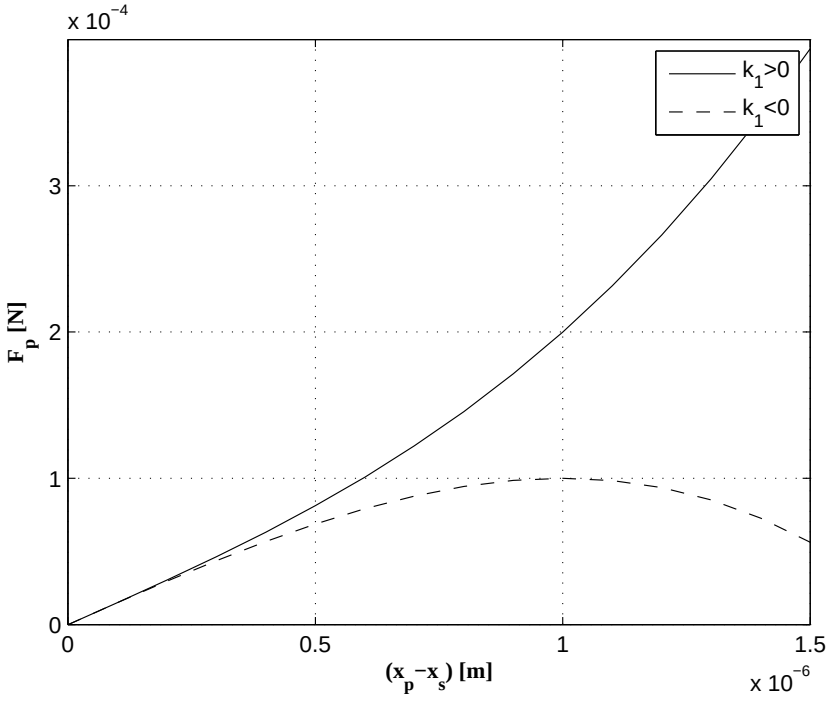

Figure 2.4: Sample characteristic modeled through the polynomial function $F_p = k_0(x_p - x_s) + k_1(x_p - x_s)$ at varying k_1

The most interesting case to analyze is when $k_1 < 0$, which corresponds to softening of the specimen after a certain deformation.

Repeating the same logic as before, and considering the new non-linear expression of the sample characteristic, the equation of dynamic equilibrium 2.5 can be rewritten as:

$$M_s \frac{d^2 x_s}{dt^2} = -D\frac{dx_s}{dt} - k_s x_s + k_0(x_p - x_s) + k_1(x_p - x_s)^3 \qquad (2.11)$$

which simplifies in the steady-state condition as:

$$-k_s x_s + k_0(x_p - x_s) + k_1(x_p - x_s)^3 = 0 \tag{2.12}$$

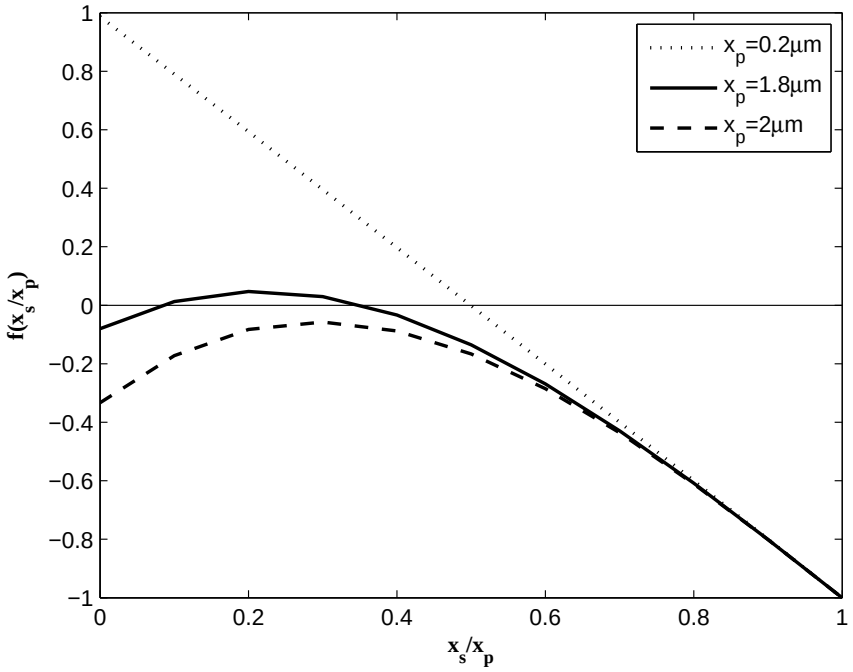

Figure 2.5: The function $f(x_s/x_p)$ versus x_s/x_p for different values of the specimen displacement x_p

This becomes, after dividing both sides by $k_s \cdot x_p$:

$$\frac{k_1}{k_s} x_p^2 \Big(1 - \frac{x_s}{x_p}\Big)^3 - \frac{x_s}{x_p}\Big(1 + \frac{x_s}{x_p}\Big) + \frac{k_0}{k_s} = 0 \tag{2.13}$$

As before, it is convenient to introduce the function $f(x_s/x_p)$, whose roots are the solutions of the equilibrium equation:

$$f(x_s/x_p) = \frac{k_1}{k_s} x_p^2 \Big(1 - \frac{x_s}{x_p}\Big)^3 - \frac{x_s}{x_p}\Big(1 + \frac{x_s}{x_p}\Big) + \frac{k_0}{k_s} \tag{2.14}$$

To evaluate the stability of the equilibrium point, it is possible to repeat the previous discussion, thus showing that the temporal derivative of x_s is $f(x_s/x_p)$ multiplied by a positive constant.

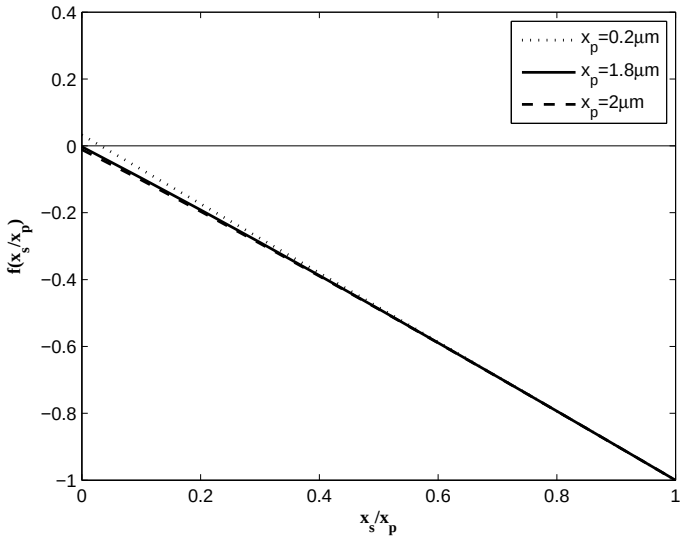

Figure 2.6: If the load sensor stiffness is increased, equilibrium is allowed even for bigger displacements of the sample

Figure 2.5 shows $f(x_s/\ x_p)$ as a function of x_s/x_p at varying x_p, and constant $k_s = k_0 > 0$. Such function is cubic, thus allowing for more than one solution. However, the region of interest here is limited to to the interval $0 < x_s/x_p < 1$, where the end of the specimen attached to the actuator moves more than the one attached to the load sensor (that is what should happen during a real test). At increasing x_p, $f(x_s/x_p)$ has first one root, corresponding to a stable equilibrium point, then it shows two roots. One is an unstable equilibrium point, whereas the other one is a stable point. With

reference to figure 2.4, it is possible to notice that the first point corresponds to a deformation of the sample falling in the softening region, while the second one to a deformation falling in the first part of the characteristic. Then, if x_p is further increased, no equilibrium can be achieved. In order to have stable equilibrium positions, even for specimen deformation (e.g. $x_p - x_s$) belonging to the softening region, one can increase the load sensor stiffness. In fact, figure 2.6 shows the response of the same system, for the same x_p, but for $k_s = 30 \cdot k_0$. The last case to consider in order to develop a model even more realistic regards a sample, whose characteristic is generic, and similar to the one reported in figure 2.7.

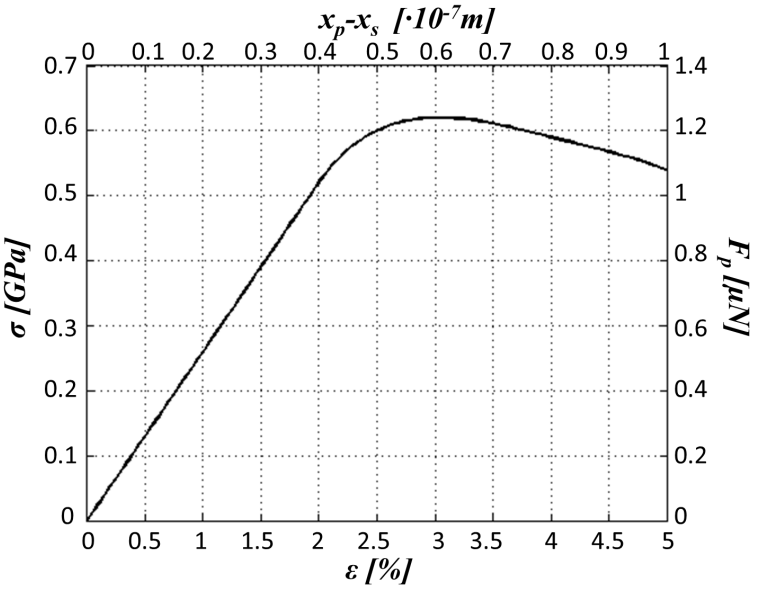

Figure 2.7: A generic sample characteristic, including a softening region

On repeating the same passages as before, first the new equilibrium equation can be written:

$$M_s \frac{d^2 x_s}{dt^2} = -D \frac{dx_s}{dt} - k_s x_s + F_p(x_p - x_s) \tag{2.15}$$

In steady-state condition, this simplifies in:

$$-k_s x_s + F_p(x_p - x_s) = 0 \tag{2.16}$$

Or, when dividing by x_p:

$$-k_s \frac{x_s}{x_p} + \frac{1}{x_p} F_p(x_p - x_s) = 0 \tag{2.17}$$

Then, the function $f(x_s/x_p)$ can be introduced, equal to the second term of the previous equation, whose roots are the equilibrium positions of the load sensor:

$$f(x_s/x_p) = -k_s \frac{x_s}{x_p} + \frac{1}{x_p} F_p(x_p - x_s) \tag{2.18}$$

For sake of comparison, figure 2.8 plots $f(x_s/x_p)$ as a function of x_s/x_p at varying x_p, and for a fixed k_s equal to the slope of the sample characteristic in the linear regime.

Until a certain value of x_p, $f(x_s/x_p)$ has roots, thus equilibrium is allowed. The stability of such equilibrium points can be inferred in the same way as before. For further increasing values of x_p, no roots are then available, which means no equilibrium can be achieved.

As before, equilibrium and stability can be provided by increasing the stiffness of the load sensor.

As a conclusion of the previous discussion, the role of the load sensor stiffness emerges as a critical parameter of the device stability. In particular, problems may arise when the sample characteristic shows softening. In this case, for the load sensor to still be able to achieve an equilibrium position, it should have the highest possible spring constant. Ideally, if this is infinite (e.g., the load sensor is a rigid structure) no instability problems occur.

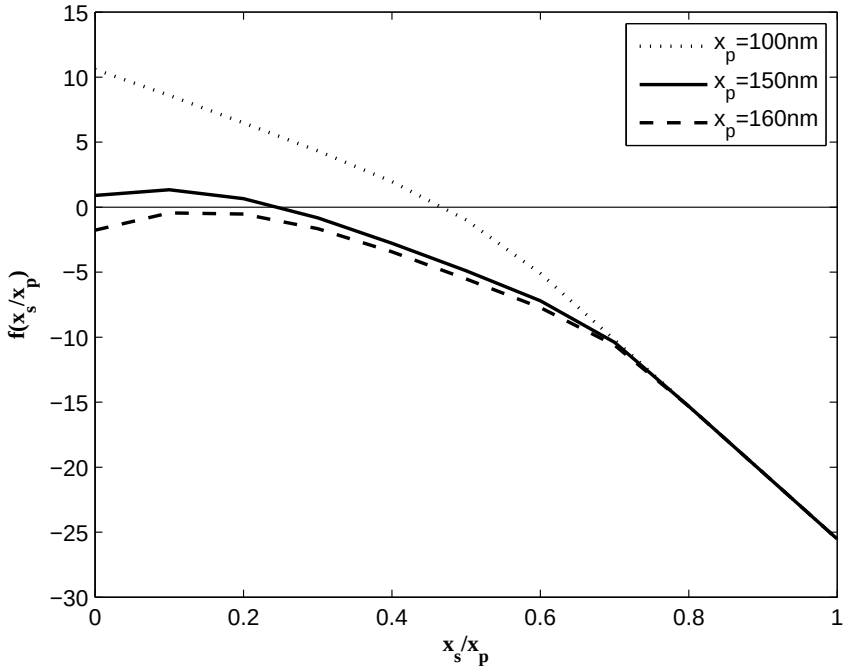

Figure 2.8: (a) The function $f(x_s/x_p)$ versus x_s/x_p for different values of the specimen displacement

However, a trade-off has to be achieved between stability needs and sensor sensitivity.

2.3 The previous tensile testing device

A typical device which can be modeled through the analytical approach presented in the previous section is the tensile testing device developed inside the Micro and Nanomechanics Laboratory of Northwestern University (Evanston, IL, USA) [149] (figure 2.9). Like other devices, it consists of an actuator and a load sensor, with a small gap (2 μm wide in this case) for

positioning of the sample. This latter is usually a one-dimensional nanostructure, like a nanotube or a nanowire, and is connected with both the actuator and the sensor as springs in series.

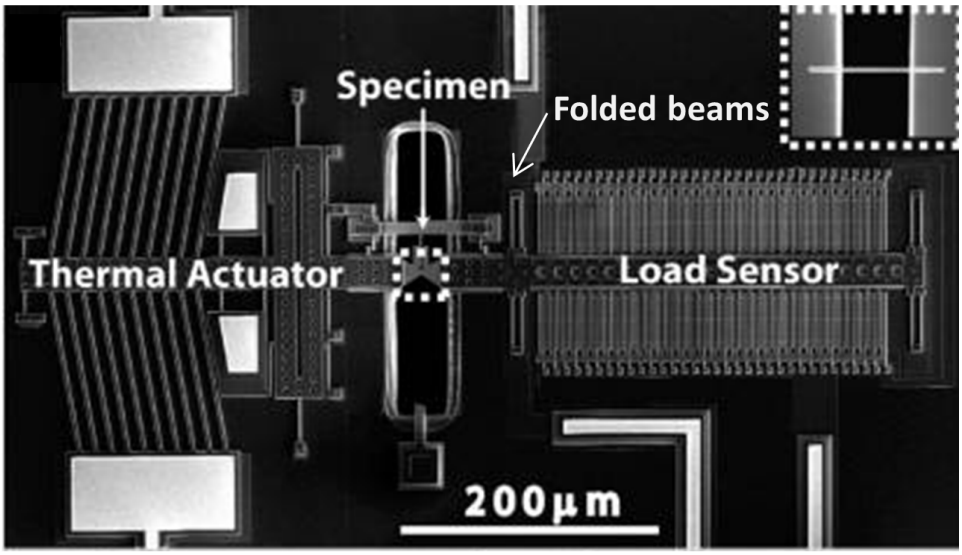

Figure 2.9: SEM picture showing the previous tensile testing device developed inside the Micro and Nanomechanics Laboratory of Northwestern University (Evanston, IL, USA) [149]

The actuator is a thermal actuator, consisting of a central freestanding body with v-shaped beams, fixed at the ends to the substrate [151]-[152]. When a voltage is applied between the v-beams, the corresponding current flow generates heat by Joule effect. Thus, the beams deflect and move the central body, which pulls the end of the specimen attached to it.
Between the sample and the v-shaped beams, there is a hollow rectangle, anchored to the substrate by short beams, which has the function to improve heat dissipation, thus reducing the temperature at the interface with

the sample.

The load sensor is a capacitive comb-drive sensor, consisting of a central freestanding body with 64 protruding fingers, which move when the sample is stretched. Such fingers are separated by a small gap of 2 μm from the corresponding fixed fingers, connected to the substrate, thus being the electrodes of a parallel of variable capacitors [153]. Their configuration reproduces a differential capacitive scheme, in order to have direct proportionality between the output of the sensor and any displacement applied to it. In particular, each movable electrode lies between two fixed ones. Thus, when the load sensor central body moves as a consequence of the thermal actuation, each movable electrode moves apart from one of its corresponding fixed electrodes, while closer to the other. Thus, there is no longer balance between the two capacitances. These are then connected to a commercial chip (Universal Capacitive Readout MS3110; Microsensors, Costa Mesa, CA), which computes the difference between them and provides as output a voltage directly proportional to the capacitance difference, which is on turn proportional to the displacement [153].

The critical element of such device is the load sensor, which was designed to have comparable stiffness to the one of the sample, in order to guarantee sufficient sensitivity. However, as emerged from the previous discussion, when the load sensor and the sample can be modeled as springs in series, with similar spring constant, the load sensor may not be able to reach stable equilibrium positions as the force transmitted through the specimen starts decreasing (e.g., shows softening). In these circumstances, instability may occur, triggering dynamic failure of the sample, thus compromising the remaining of the test. This is what likely happened during the experiment reported in [149]. Here, the device was applied to investigate a ZnO

nanowire, and the corresponding experimental behavior was compared to the results obtained from atomistic simulations. In particular, the numerical model predicted a characteristic curve characterized by load drops, but these could not be confirmed by experimental evidence, since the sample collapsed before.

As a consequence, instability results to be a very complex and dangerous issue, which causes the device of figure 2.9 to not be suitable to test samples showing softening, with a consequent reduction of its potential applications. A way to remove such problem would be the availability of a specimen either controlled in displacement at both ends or just fixed at one end and controlled in displacement at the other. Actually, either of these two configurations can be found in literature in the tensile testing apparatus proposed by [154] and [155]. In the first case, the testing apparatus involves the loading system developed by Hysitron Inc. This basically consists of a push-pull device fabricated on an SOI (Silicon-On-Insulator) wafer, with a small gap for positioning of the sample. This is actuated by an external punch which applies a compressive load on one side of the device. Such compressive action is then transferred to a system of four springs, which are in parallel with the sample, and guarantee that both its ends are pulled under a displacement control condition. The force applied by the punch is automatically recorded. However, in order to get the force on the specimen, it is necessary to subtract from the punch load the load absorbed by the device springs, which have to be carefully calibrated [154].

In the second case, the load sensor structure is substituted with a rigid element with no sensing function. Thus, both actuation and sensing are performed through the same structure, which consists of a central shuttle with inclined beams protruding from it. When a voltage is applied across the two

ends of the beams, there is current flow. By Joule effect, the current causes heat dissipation and deformation of the beams, which as a consequence displace the central shuttle. The stiffness of such structure is comparable with that of the specimen. Thus, at the same bias voltage, the delivered displacement decreases when there is a sample mounted. Such difference in displacement can then be converted into force if multiplied by the spring constant of the actuator. However, in the model reported in [156], such parameter is considered to not vary with the displacement (e.g., temperature), thus affecting the validity of the obtained results.

The configuration adopted in this second example, where the specimen is fixed at one end, could be reproduced also in the device previously described (figure 2.9) to solve its instability issue. In particular, this can be accomplished not mechanically but electrically through the implementation of an electrostatic feedback control, as reported in the present work. Here, the basic idea is to design a closed-loop scheme, able to compute and apply the correct force to maintain the load sensor at equilibrium, regardless of the force transmitted through the sample.

In spite of the complex and new electronics to implement, there is only one different mechanical element to add to the original structure, which is an electrostatic actuator.

The electrostatic actuators commonly found in MEMS devices consist of parallel electrodes, able to apply a force proportional to their transverse area. Such area depends on the thickness of the device layer, which is limited by the fabrication process.

The device of figure 2.9 was fabricated through a surface micromachining process (PolyMUMPs), which allowed for a device layer of 3.5 μm [153]. Such thickness was too small to provide a force on the order of tens of μN,

as required to break a variety of nanostructures (as shown in the next chapter). Thus, it was necessary to consider another fabrication process, able to provide a thicker device layer. In particular, the new device was fabricated through the SOI (Silicon-On-Insulator) technology, which allows for structures one order of magnitude thicker than the micromachining process previously considered.

However, the SOI introduces different limitations in the design than the PolyMUMPs. Thus, all the structures of the device have to be redesigned, even those, like the thermal actuator, which would not need any modification.

A brief description of the new design of the device will be shown in the following section, while more details will be provided in the next chapters.

2.4 The new tensile testing device

Figures 2.10, 2.11, and 2.12 show some SEM pictures of the new device. If compared to the previous design, the new one is about two times larger (1.7x0.8 mm^2), and keeps the same basic structure, consisting of a thermal actuator and an electro-capacitive element, separated by a 2 μm gap for positioning of the sample.

The thermal actuator has the same working principle as before, thus the same global architecture. In fact, it consists of ten freestanding v-shaped beams (350 μm long, 8 μm wide, and 25 μm thick, thus about one order of magnitude thicker than the previous ones), which are anchored to the substrate at locations 3) and 4), as shown in figure 2.11.

Apart from the v-beams, the actuator is also provided with a couple of short beams, anchored to the substrate in 1) and 2) to limit possible out-of-plane

movements, and a hollow rectangle, anchored at locations 5) and 6) (figure 2.11). This latter structure was already included in the previous design to improve heat dissipation. However, in order to meet the new fabrication requirements (the anchor points must lie relatively far from the freestanding region), the position and the configuration of the anchoring beams (12 in this case) had to be changed.

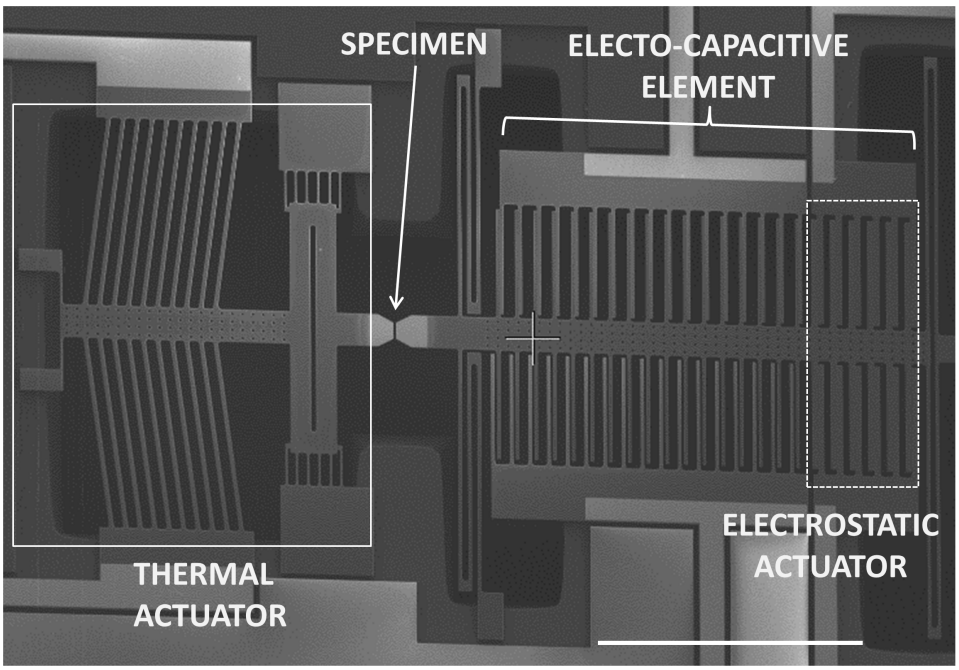

Figure 2.10: SEM picture of the present device (scale bar: 500 μm)

The electro-capacitive element consists of a an electrostatic actuator and a displacement transducer, which is capacitive and comb-drive based.
Like in the previous generation, this latter has a freestanding body (anchored to the substrate at locations 7, 8, and 9 through four folded beams) with protruding fingers (200 μm long, 7 μm wide, and 25 μm thick comb-drive

elements), which are interdigitated with other fingers, fixed to the substrate (figure 2.12).

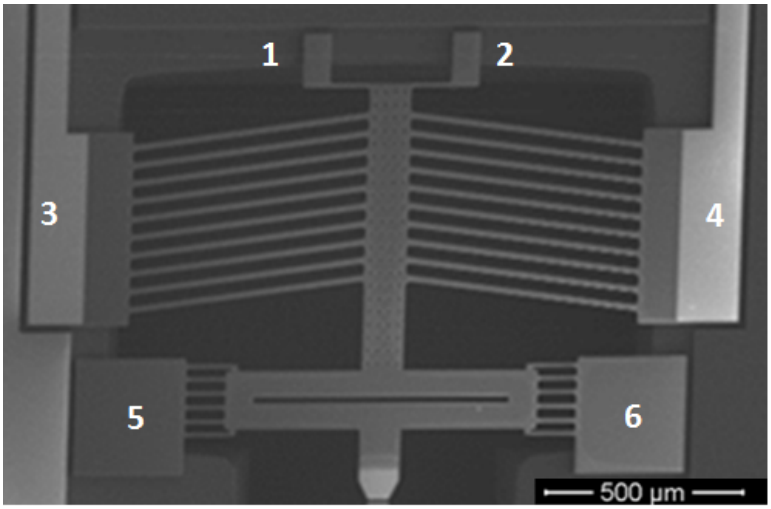

Figure 2.11: SEM picture of the thermal actuator

While the bottom folded beams in figure 2.12 have two branches, like in the previous device, the uppermost two have three branches each. The reason for such difference is the same fabrication requirement already mentioned, which forces the anchor points to be far from the freestanding region.
Also in this case, a differential capacitive scheme was implemented, in order to get a linear relationship between the displacement and the corresponding sensor output. However, because of fabrication limits, the electrodes were designed according to a different configuration, where one movable electrode still lies between two fixed ones, but the relative position between each movable finger and the corresponding fixed fingers is not the same on both side of the sensor, but inverted, as it will be shown more in detail in the next chapter.

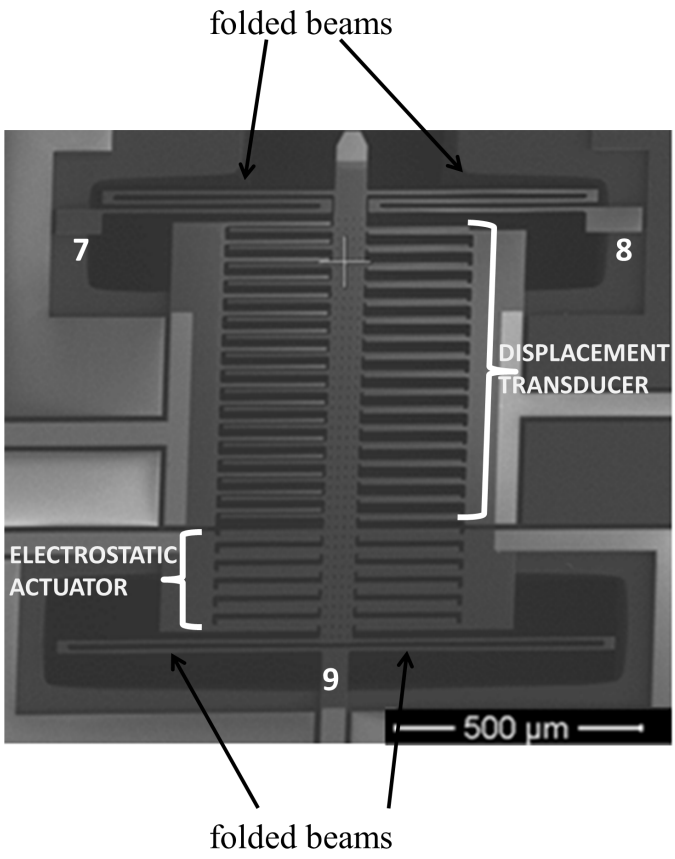

Figure 2.12: SEM picture of the new sensor

In spite of the secondary differences already reported, the main novelty of the new design is the presence of a parallel plate electrostatic actuator, consisting of 12 electrodes. These latter were positioned in order to generate a force acting along the opposite direction to the one transmitted by the sample. In fact, such actuator is interfaced with a controller (figure 2.13), which computes the correct force the actuator has to generate in order to maintain the electro-capacitive element at equilibrium, thus providing a feedback control (figure 2.14).

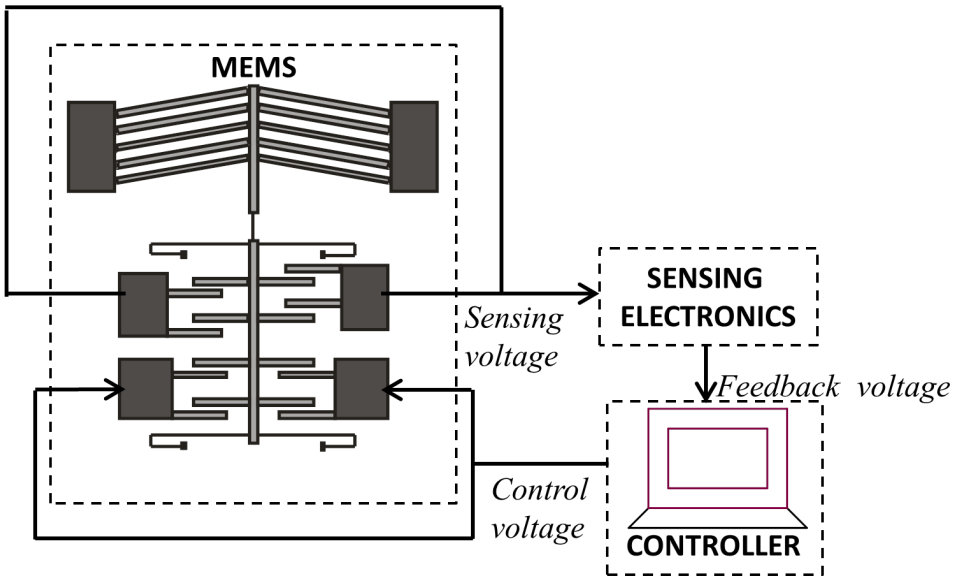

Figure 2.13: A schematic of the whole testing apparatus

The controller function is performed through the routine of a custom-made virtual instrument developed in LabView environment. Through proper electronics, this receives as input the output signal of the sensor, which is proportional to its physical displacement, and provides as output the bias voltage to the electrostatic actuator necessary to keep the balance.

Since the aim of the feedback control is to keep the equilibrium, the output of the sensor should be steadily equal to 0. Thus, it cannot be longer used for computation of the load, which is instead derived from the electrostatic force applied by the actuator.

As shown in figure 2.13, the whole testing apparatus includes several parts: the physical device, all the electronics for conveying the signals, and the routine implementing the controller. For the sake of clarity, each of them

will be separately discussed in one of the following three chapters.

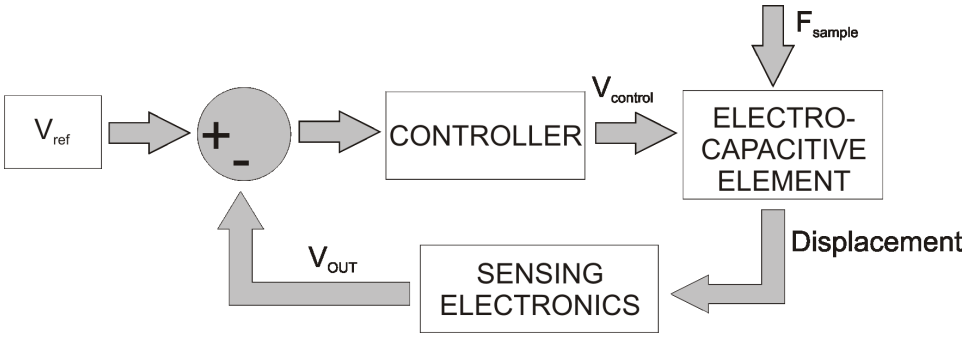

Figure 2.14: A schematic of the feedback control principle

Chapter 3

Design and fabrication

3.1 Introduction

As mentioned in the previous chapter, the novel MEMS-based testing system is composed of both hardware and software parts. The hardware part consists of the thermal actuator, the electro-capacitive element, and all the electronics needed for carrying the corresponding signals. The software part includes instead a series of routines in LabView environment, which implement a feedback control for preventing the electro-capacitive element from any significant movement. Such condition is essential to guarantee stability of the device during a test, as previously discussed.

In this chapter, attention is paid to the design of the actuating and sensing parts, while electronics and the routines for the feedback control will be illustrated in the following chapters.

3.2 The thermal actuator

As already explained, the thermal actuator has a central body with a series of inclined beams (figure 3.1). When these are biased with a voltage, the corresponding current flow generates heat by Joule effect, which as a consequence causes deformation of the beams and displacement of the central body (shuttle).

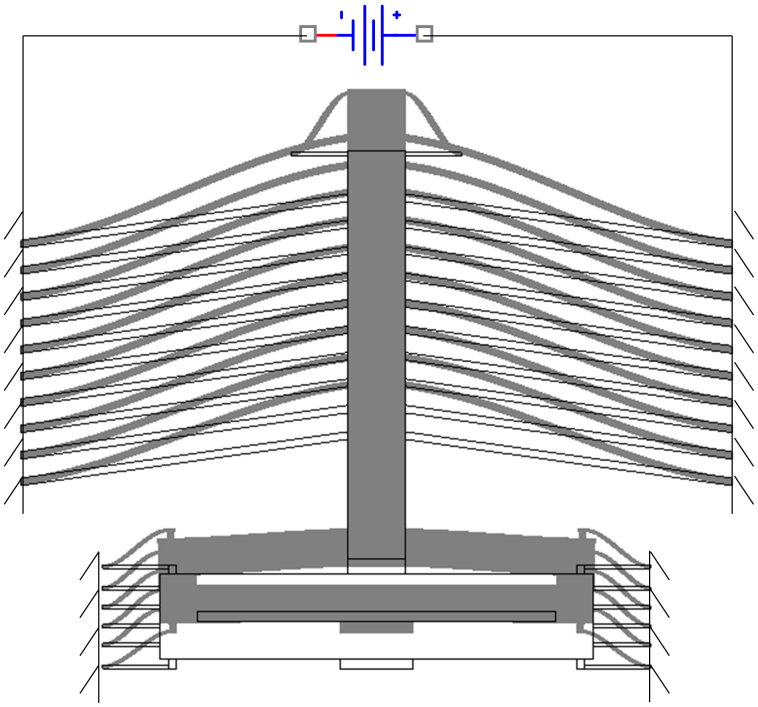

Figure 3.1: A schematic of the thermal actuator deformation

The actuator performance can be expressed on the basis of two parameters: the maximum displacement (d_A) and the axial stiffness (k_A). This latter should be as higher as possible compared to the one of the sample, in order for the actuator to not deform significantly during the test and transfer most

of the delivered displacement to the sample [159]. In fact, when there is no sample mounted, the force acting on the actuator can be expresses as:

$$F = k_A \cdot u_u \tag{3.1}$$

where k_A is the actuator stiffness and u_u its undisturbed displacement. However, when there is a sample mounted, the same force previously applied on the actuator can now be written as:

$$F = k_A \cdot u_d + k_s \cdot u_d \tag{3.2}$$

where k_s is the sample stiffness and u_d is the new displacement of the actuator end where the sample is mounted. In general, the displacement of the actuator end changes when this is connected to a sample. In particular, from the two above equations, it follows that:

$$k_A \cdot u_u = k_A \cdot u_d + k_s \cdot u_d \tag{3.3}$$

Thus, rearranging:

$$\frac{u_d}{u_u} = \frac{1}{1 + k_s/k_A} \tag{3.4}$$

In order for the thermal actuator to displace by the same amount even when there is a sample mounted, the ratio k_s/k_A should be as smaller as possible. In particular, if $k_A = 100k_s$, then $u_d = 99\%u_u$, which guarantees that tests are effectively conducted under displacement control.

As regards the sample, its stiffness can be evaluated as that of a body under tensile load:

$$k_s = \frac{EA}{L} \tag{3.5}$$

where E is the Young modulus, A the transverse area, and L the length. For example, a 2 μm long silver nanowire (E=83 GPa [184]), with circular

cross-section and 50 nm diameter, has an axial stiffness of: $k_s = 81$ N/m. A 2 μm long GaN nanowire (E=300 GPa [158]), with hexagonal cross section and diameter of 50 nm, has an axial stiffness of: $k_s = 244$ N/m. As said before, the actuator stiffness should be about two orders of magnitude bigger than k_s. Thus, if $k_A > 20000$ N/m, the thermal actuator is suitable to test a variety of materials.

The second parameter previously mentioned is the maximum displacement the actuator can guarantee, which has to be sufficiently high to bring at fracture a variety of samples. Considered that the sample gage length (L) is is equal to the gap between the actuator and the electro-capacitive element (this is a lower bound, though, since the sample cannot be fixed right in correspondence of the gap), which is 2 μm, if a fracture strain $\epsilon = 50\%$ (this is an upper bound, since usually nanowires fracture after 5-10% strain) is assumed, the corresponding displacement of the sample is: $\Delta L = \epsilon \cdot L = 1\mu m$. Thus, the actuator should guarantee such a displacement.

In order to accomplish both the requirements of high axial stiffness and maximum displacement, it is useful to develop two analytical models, which relate them to the actuator characteristic parameters (e.g., thickness, length, width, and number of v-shaped beams). However, because of the structural complexity, the analytical model (which follows the procedure described in [159]) is useful to provide only a guess set of parameters to guide the design. Then, the final design has to be carried out more accurately by a numerical modeling based on FEM analysis.

3.2.1 Analytical modeling

The thermal actuator consists of a series of v-beams, which experience all the same displacement (figure 3.2(a)). Thus, only one exemplary beam can be studied for initial analysis (figure 3.2(b)).

For simplicity, it is convenient to introduce a local reference system (ξ, η) rotated with respect to the global reference system (x, y) by an angle θ. The beam is clamped at one end, A, (where it is anchored to the substrate) and guided at the other end, B, where it is connected to the shuttle (figure 3.2(b)).

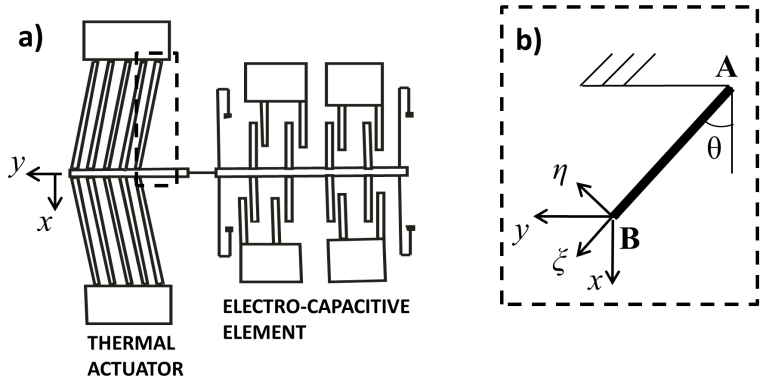

Figure 3.2: (a) Schematic of the MEMS under study, and (b) zoom in on one of the thermal actuator inclined beams

From beam theory, it follows that:

$$F_\xi = \frac{EA}{L} u_\xi \tag{3.6}$$

$$F_\eta = \frac{12EI}{L^3} u_\eta \tag{3.7}$$

In the above, F_ξ is the force applied along the beam axial direction, F_η is the force applied along the beam transverse direction, u_ξ is the displacement along the beam axial direction, u_η is the displacement along the beam

transverse direction, E is the Young modulus of the beam, A its transversal area, L its length, and I its moment of inertia. Thus, it is possible to write:

$$\begin{bmatrix} \frac{EA}{L} & 0 \\ 0 & \frac{12EI}{L} \end{bmatrix} \begin{Bmatrix} u_\xi \\ u_\eta \end{Bmatrix} = \begin{Bmatrix} F_\xi \\ F_\eta \end{Bmatrix} \tag{3.8}$$

Or, in compact form:

$$[\hat{k}]\{u_{\xi,\eta}\} = \{F_{\xi,\eta}\} \tag{3.9}$$

where $[\hat{k}]$, which is the beam stiffness matrix in the local reference system (ξ, η), while $\{u_{\xi,\eta}\}$ and $\{F_{\xi,\eta}\}$ are:

$$[\hat{k}] = \begin{bmatrix} \frac{EA}{L} & 0 \\ 0 & \frac{12EI}{L} \end{bmatrix} \qquad \{u_{\xi,\eta}\} = \begin{Bmatrix} u_\xi \\ u_\eta \end{Bmatrix} \qquad \{F_{\xi,\eta}\} = \begin{Bmatrix} F_\xi \\ F_\eta \end{Bmatrix} \tag{3.10}$$

From the geometry of the problem, it is possible to write:

$$\begin{Bmatrix} u_\xi \\ u_\eta \end{Bmatrix} = \begin{bmatrix} \cos(\theta) & \sin(\theta) \\ -\sin(\theta) & \cos(\theta) \end{bmatrix} \begin{Bmatrix} u_x \\ u_y \end{Bmatrix} \tag{3.11}$$

Or simply:

$$\{u_{\xi,\eta}\} = [T]\{u_{x,y}\} \tag{3.12}$$

where $[T]$ is the transformation matrix:

$$[T] = \begin{bmatrix} \cos(\theta) & \sin(\theta) \\ -\sin(\theta) & \cos(\theta) \end{bmatrix} \tag{3.13}$$

Similarly:

$$\{F_{\xi,\eta}\} = [T]\{F_{x,y}\} \tag{3.14}$$

If equations (3.12) and (3.14) are substituted into equation (3.9), this latter becomes:

$$[\hat{k}][T]\{u_{x,y}\} = [T]\{F_{x,y}\} \tag{3.15}$$

which can be further modified as:

$$[T]^{-1}[\hat{k}][T]\{u_{x,y}\} = \{F_{x,y}\} \tag{3.16}$$

Or, simply:

$$[k]\{u_{x,y}\} = \{F_{x,y}\} \tag{3.17}$$

where $[k]$ is the beam stiffness in the global reference system:

$$[k] = \begin{bmatrix} k_x & k_{xy} \\ k_{yx} & k_y \end{bmatrix} \tag{3.18}$$

which can be written after some passages as:

$$[k] = \begin{bmatrix} \frac{EA}{L}\cos^2(\theta) + 12\frac{EI}{L^3}\sin^2(\theta) & \left(\frac{EA}{L} - 12\frac{EI}{L^3}\right)\cos(\theta)\sin(\theta) \\ \left(\frac{EA}{L} - 12\frac{EI}{L^3}\right)\cos(\theta)\sin(\theta) & \frac{EA}{L}\sin^2(\theta) + 12\frac{EI}{L^3}\cos^2(\theta) \end{bmatrix} \tag{3.19}$$

Then, equation (3.17) can be written in extended form as:

$$\begin{bmatrix} \frac{EA}{L}\cos^2(\theta) + 12\frac{EI}{L^3}\sin^2(\theta) & \left(\frac{EA}{L} - 12\frac{EI}{L^3}\right)\cos(\theta)\sin(\theta) \\ \left(\frac{EA}{L} - 12\frac{EI}{L^3}\right)\cos(\theta)\sin(\theta) & \frac{EA}{L}\sin^2(\theta) + 12\frac{EI}{L^3}\cos^2(\theta) \end{bmatrix} \begin{Bmatrix} u_x \\ u_y \end{Bmatrix} = \begin{Bmatrix} F_x \\ F_y \end{Bmatrix} \tag{3.20}$$

The forces acting on the v-beam are the thermal load and the reaction forces:

$$\begin{Bmatrix} F_x \\ F_y \end{Bmatrix} = \begin{Bmatrix} \alpha\Delta T EA\cos(\theta) \\ \alpha\Delta T EA\sin(\theta) \end{Bmatrix} + \begin{Bmatrix} R_x \\ R_y \end{Bmatrix} \tag{3.21}$$

In the above, α is the thermal expansion coefficient of the beam material and ΔT is the temperature increase. The beam is allowed to move along y, but cannot move along the x-axis (being connected to the shuttle), corresponding to R_y=0 and $u_x = 0$. Then, if equation (3.21) is substituted into equation

(3.20), from the second matrix equation, it is possible to derive directly the displacement along the y-axis:

$$u_y = \frac{\alpha \Delta T L \sin(\theta)}{\sin^2(\theta) + \frac{12I}{AL^2}\cos^2(\theta)} \tag{3.22}$$

Similarly, from the second matrix equation, the reaction force along x is:

$$R_x = -\alpha \Delta T E A \frac{\cos(\theta)}{\cos^2(\theta) + \frac{AL^2}{12I}\sin^2(\theta)} \tag{3.23}$$

From which the reactive force in the local reference system (ξ, η) can be derived:

$$\begin{Bmatrix} R_\xi \\ R_\eta \end{Bmatrix} = \begin{bmatrix} \cos(\theta) & \sin(\theta) \\ -\sin(\theta) & \cos(\theta) \end{bmatrix} \begin{Bmatrix} R_x \\ R_y \end{Bmatrix} \tag{3.24}$$

Which simplifies as:

$$\begin{Bmatrix} R_\xi \\ R_\eta \end{Bmatrix} = \begin{Bmatrix} R_x \cos\theta \\ R_x \sin\theta \end{Bmatrix} \tag{3.25}$$

Furthermore, from the stiffness matrix $[k]$ (equations 3.18 and 3.19) it is possible to derive the beam stiffness along the y-axis (e.g., direction of actuator movement), which is defined as the ratio of the force along y to the corresponding displacement. This is:

$$k_y = \frac{EA}{L}\sin^2(\theta) + \frac{12EI}{L^3}\cos^2(\theta) \tag{3.26}$$

The thermal actuator consists of n inclined beams, which can be considered as parallel springs, since they all experience the same displacement. Thus, the global stiffness of the actuator, along the y-axis, can be calculated from the (3.26):

$$K_y = nk_y = n\left(\frac{EA}{L}\sin^2(\theta) + \frac{12EI}{L^3}\cos^2(\theta)\right) \tag{3.27}$$

Equations (3.22) and (3.27) relate the actuator stiffness and displacement to many design parameters, like the number, the width, the length, the

thickness, and the inclination angle of the v-beams, which have thus to be carefully chosen in order to accomplish both requirements of high stiffness and displacement.

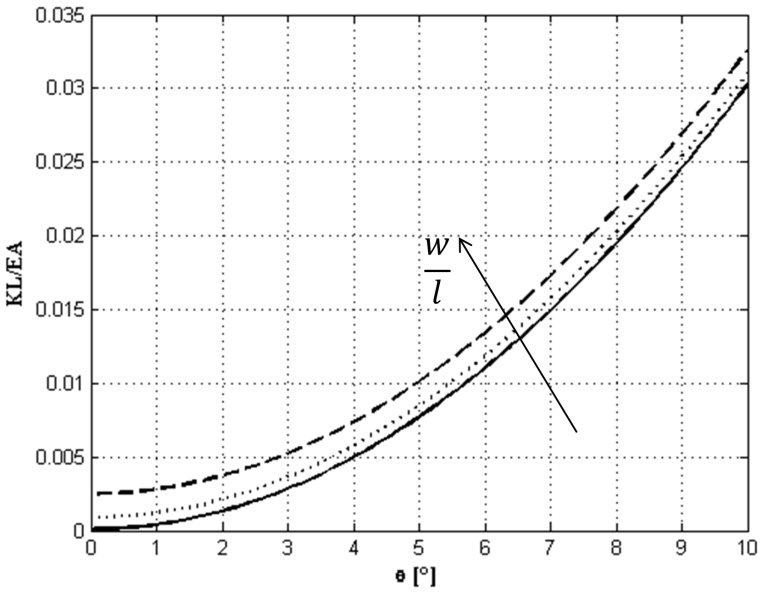

Figure 3.3: Dependence of the normalized stiffness of one v-beam on the inclination angle at varying thickness to length ratio

Figures (3.3) and (3.4) plot the normalized stiffness and displacement of one inclined beam versus its inclination angle, assuming a rectangular cross-section. It is possible to notice that while the beam stiffness is always proportional to the inclination angle, the achievable displacement first increases and then decreases. Furthermore, while the stiffness increases with the width to length ratio, the contrary happens for the displacement. Thus, a trade-off value for the inclination angle and the width to length ratio must be identified.

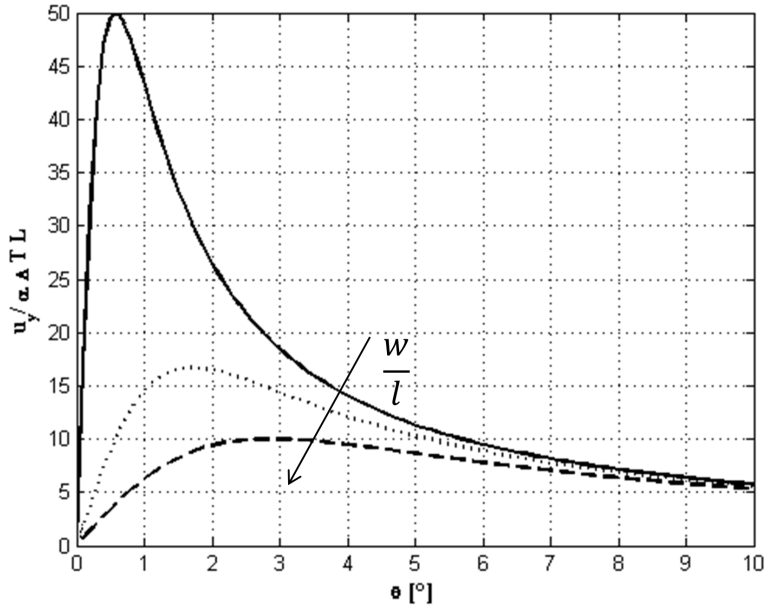

Figure 3.4: Dependence of the normalized displacement of one v-beam on the inclination angle at varying thickness to length ratio

Furthermore, from equation (3.25), it results that each inclined beam is subject to an axial force (in the local reference system) equal to:

$$R_\xi = Rx\cos\theta = -\alpha\Delta TEA\frac{\cos^2(\theta)}{\cos^2(\theta) + \frac{AL^2}{12I}\sin^2(\theta)} \tag{3.28}$$

The minus sign indicates that this is a compressive load. Thus, it is necessary to verify that such load does not exceed the critical load. In particular, for a clamped-guided beam, as the inclined beam can be modeled, the critical load before buckling is:

$$P_{cr} = \frac{\pi^2 EI}{L^2} \tag{3.29}$$

Figure 3.5 shows a comparison between the normalized compressive load on the beam, computed with equation 3.28, considering a very high temperature increase (800 °C which is above the suggested operating temperature of

silicon [159]), and the corresponding normalized critical load, as functions of the inclination angle. The most critical condition is when w/L assumes its smallest value, corresponding to 2/500 (by fabrication limits). In this case, for $\theta > 3.5°$, the compressive load is smaller than the critical one. In all the other cases, instability is avoided for a smaller θ.

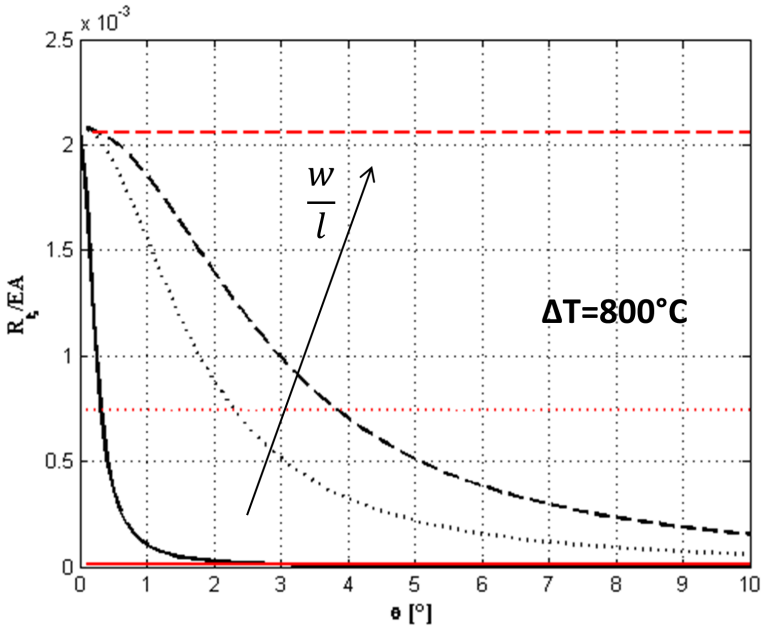

Figure 3.5: Dependence of the compressive load force (black lines) on the inclination angle of one inclined beam at varying width to length ratio, as compared to the corresponding buckling load (red lines), as functions of the inclination angle

Thus, the main constraints on the choice of the angle come from the requirements of high displacement and stiffness, which should be, as previously derived:

$K_y > 20000$ N/m

$u_y = 1\,\mu$m.

The design parameters, as the length, width, number, and inclination angle of the v-beams can be arbitrarily decided, whereas the thickness is constrained by the considered fabrication process to be 25 μm. After an optimization process carried out in order to accomplish both the aforementioned requirements, as well as to minimize the overall size of the actuator, the following values were identified:

Length of the beams, $L = 350\,\mu$m
Width of the beams, $w = 8\,\mu$m
Inclination angle, $\theta = 8°$
Number of beams, $n = 10$

On considering such values, and given that Silicon has a Young modulus of 169 GPa [160], and a thermal expansion coefficient of $2.6{\cdot}10^{-6}\,°\text{C}^{-1}$ [161], equations (3.27) and (3.22) provide the stiffness and displacement of the thermal actuator: $K_y = 38400$ N/m and $u_y = 2.87\,\mu$m for a temperature increase of 450°C. Furthermore, with reference to equation (3.28), the compressive load is 1.0 mN, which is smaller than the critical load, which is 1.5 mN for this geometry.

As regards the stress state, each beam is subjected to a compressive load and a transverse load, too, which correspond to primarily a uniaxial stress. However, the stress associated to such loads is reasonably small, being on the order of few MPa, while the maximum stress Silicon can bear is on the order of few GPa ([153],[162]).

3.2.2 Numerical modeling

For a more detailed analysis of the thermal actuator, it can be useful to consider also a numerical approach, and then compare the numerical results with those obtained with the analytical model. In this case, a commercial finite element software, like Comsol Multiphysics, is very appropriate, since it allows for solution of problems defined in different physical domains (multiphysics problems). In fact, modeling of the thermal actuator requires three different kinds of analysis: structural, thermal, and electrical. These can be carried out by the means of an already implemented module within the software, which is properly designed for performance of combined electro-thermo-structural simulations.

In order to completely define the thermal actuator behavior, the following parameters have to be set:

Mechanical domain

Elastic constants [160], $\mathrm{E_x} = \mathrm{E_y} = 169\,\mathrm{GPa}$

Poisson ratio [160], $\nu_{\mathrm{xy}} = 0.064$

Shear modulus [160], $\mathrm{G_{xy}} = 50.9\,\mathrm{GPa}$

Thermal expansion coefficient [161], $\alpha = 2.6 \cdot 10^{-6}\,^{\circ}\mathrm{C}^{-1}$

Density [163], $\rho = 2300\,\mathrm{kg/m^3}$

Thickness, $\mathrm{t} = 25\,\mu m$

Electrical domain

Resistivity [164], $\rho_0 = 1.3 \cdot 10^{-4}\,\Omega\mathrm{m}$

Thermal domain

Thermal conductivity [163], $\mathrm{k} = 130\,\mathrm{Wm^{-1}K^{-1}}$

Reference Temperature, $\mathrm{T_0} = 293.15\,\mathrm{K}$

As regards the boundary conditions, in the mechanical domain, all the v-beams were clamped at the end, where they are anchored to the substrate, while being free elsewhere. In the electrical domain, a voltage difference was applied across each v-beam, and all the other borders were considered to be electrically isolated.

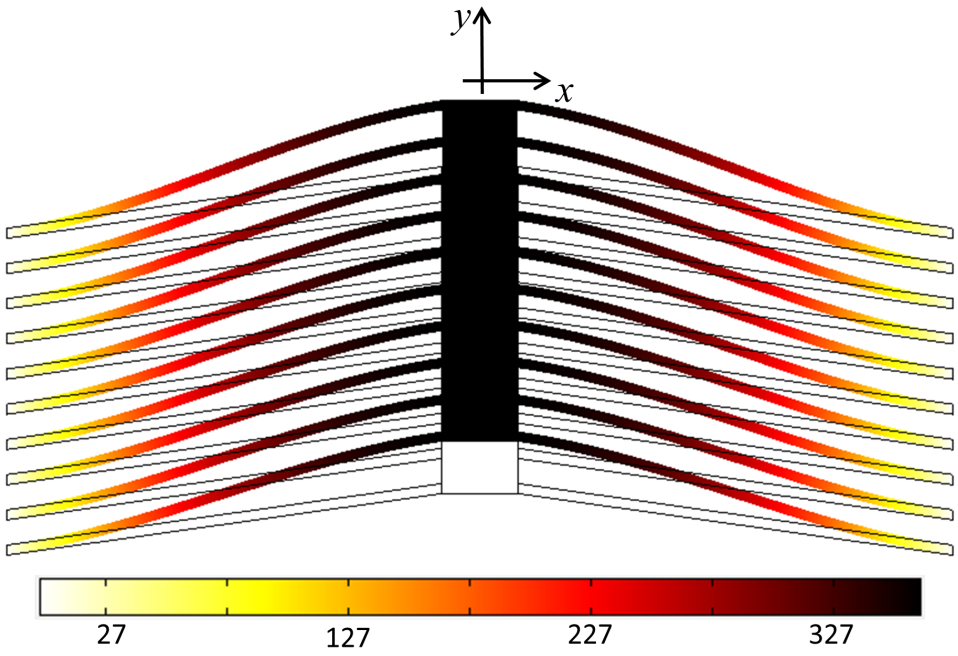

Figure 3.6: Temperature field (° C) of the thermal actuator if a voltage of 7 V is applied across its v-beams

Finally, in the thermal domain, the ambient temperature was fixed at both ends of the v-beams, where they are anchored to the substrate, which behaves like a heat sink. All the other borders were considered to be thermally isolated (e.g., convection was not considered, since the thermal actuator will be operating in vacuum).

For simplicity 2D analyses were carried out, and, because of the relatively high thickness of the studied geometry (25 μm), plane strain conditions were assumed. The modeled geometry was the same optimized geometry as resulted from the analytical analysis. Thus, it consists of 20 350 μm long, 8 μm wide, and 25 μm thick beams, inclined by 8° with respect to the x-axis. They are connected to a central 60 μm wide shuttle.

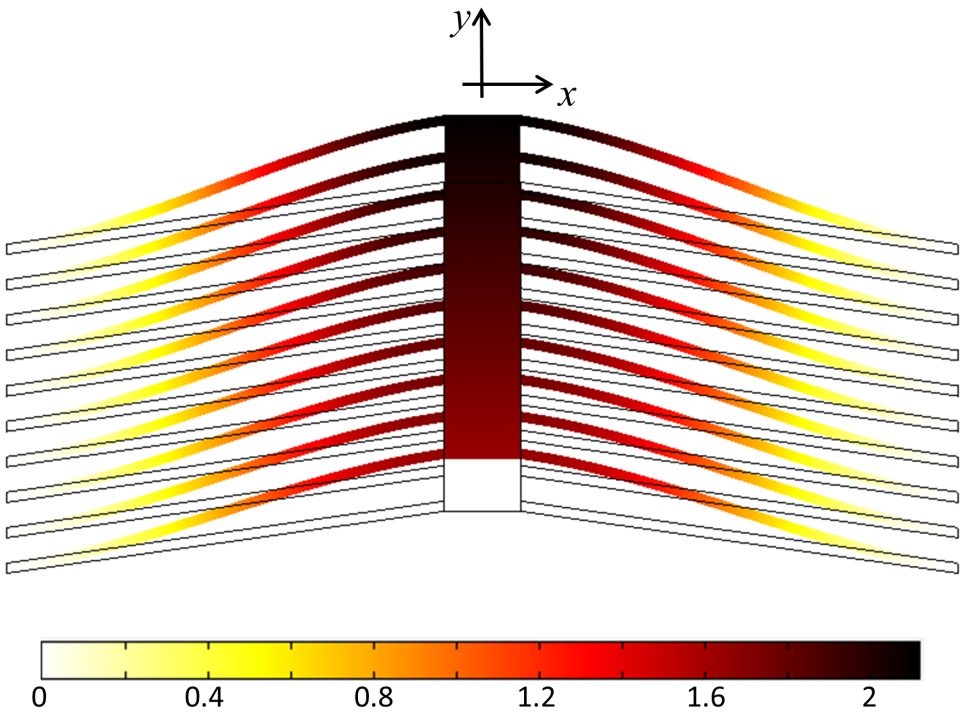

Figure 3.7: Displacement field (μm) of the thermal actuator along the y-axis when biased with a voltage of 7 V

The mesh was automatically generated by the software, and consisted of about 3000 triangular elements. All of the analyses were performed as steady-state on a PC with the following technical features: RAM 6 GB,

Intel(R) Core(TM) i7 CPU Q 740-1.73 GHz. In these conditions, the computational time was only few seconds.

Figure 3.6 plots the temperature field over the thermal actuator, when biased with 7 V. As can be seen, the temperature distribution is not uniform, and reaches a maximum of 636 K on the shuttle. With reference instead to the displacement, the numerical analysis provided a maximum displacement on the shuttle of 2.1 μm (figure 3.7).

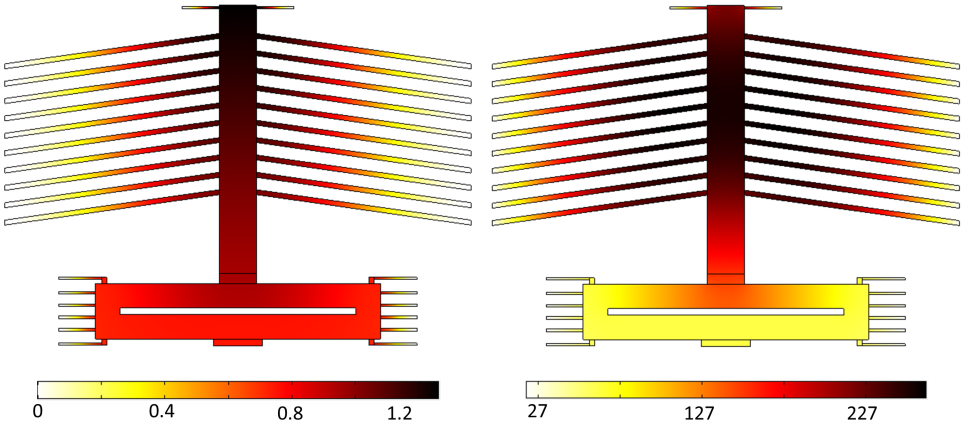

Figure 3.8: Displacement (μm) and temperature (° C) across the new thermal actuator with 7V, consisting of a dissipating structure, when biased with 7,V

In order to verify the effectiveness of the analysis, it is useful to compare the numerical results to the analytical ones, in terms of both displacement and stiffness. In particular, this latter is evaluated in the numerical model by applying an axial force to the shuttle and reading the corresponding displacement. Thus, the stiffness, which is the ratio of the force to the displacement resulted to be about 43000 N/m. If in expression (3.22) and (3.27), an av-

erage temperature of 450 K is assumed, the corresponding displacement and stiffness are 2.87 μm and 38400 N/m, respectively, which are comparable to those obtained with the numerical analysis. However, a certain difference between the numerical and analytical results is related to the presence of the central shuttle and to the temperature, which varies along the v-beams in the numerical analysis, while being constant in the analytical one.

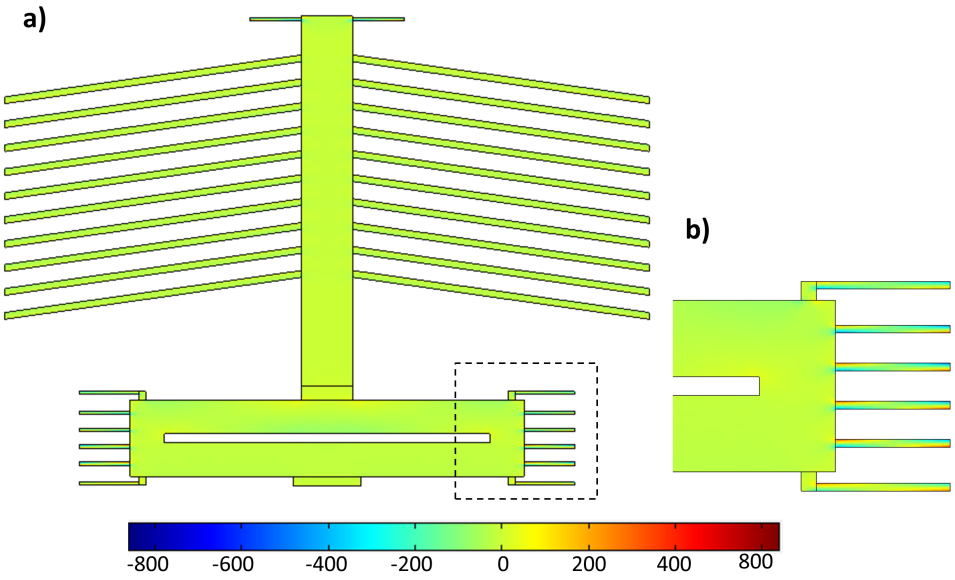

Figure 3.9: Normal stress field (MPa) over the thermal actuator (a), with a stress concentration region detailed in (b), when biased with 7V

It follows that the analytical approach is valid for a first design, which can be now refined through a numerical analysis. In fact, as can be inferred from figure 3.6, the temperature at the bottom of the thermal actuator body is quite high. This should be avoided, since this is the area at the interface with the sample. Thus, it is convenient to introduce here a dissipating structure.

This consists of a central hollow beam (90x460 μm) connected to the substrate through twelve short beams (60x4 μm), which introduce additional anchor points, thus improving heat dissipation by conduction (figure 3.8). The design validity of the new design can be inferred from figure 3.8, since for the same bias voltage as in plot of figure 3.6, the temperature at the interface with the sample (bottom region of the shuttle) is significantly lower, being only 337 K or 55° C. With reference to stress, as expected, the overall normal stress in the structure is few MPa. However, because there are many regions of stress concentration, as those close to geometrical edges, the stress can locally go up to about 600 MPa (figure 3.9). In order to reduce stress in those regions, fillets were introduced in the fabricated geometries.

The introduction of the dissipating structure decreases the actuator stiffness, which now is about 40000 N/m, still being in the range of design requirements ($>$ 20000 N/m), though. Furthermore, on improving heat dissipation, the global temperature decreases, too, thus reducing the displacement at the interface with the sample (about 800 nm). This could be further increased on applying a higher bias voltage (figure 3.10 shows the displacement and temperature at interface with the sample as functions of the bias voltage.). However, if the same analysis involving a bias voltage of 7V is repeated when considering a sample with stiffness of 100 N/m, the difference between the actuator displacement at the bottom differs by less than 1% from the displacement in the same region, when no sample is present. This means that the actuator stiffness was correctly designed.

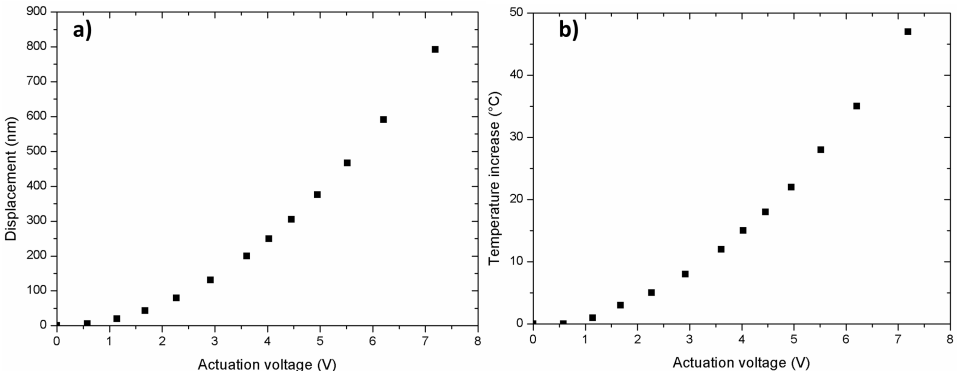

Figure 3.10: a) Displacement of the thermal actuator bottom region as a function of the bias voltage; b) Temperature increase of the thermal actuator bottom region as a function of the bias voltage

3.3 The electro-capacitive element

The main novelty in the MEMS-device reported herein is the design of an electrostatic feedback control, which has the double task to prevent the electro-capacitive element from any significant displacement, and provide measurement of the force acting on the specimen. Such functions are performed by the means of a capacitive displacement transducer and an electrostatic actuator, which define the structure of the electro-capacitive element (figure 3.11).

The displacement transducer provides measurement of the axial displacement, and has a capacitive comb-drive configuration. This is provided with a central shuttle and 34 protruding fingers, which move when the sample is stretched by the thermal actuator. Such moving electrodes are interdigitated with corresponding fixed electrodes anchored to the substrate, and arranged as a parallel of variable capacitors, whose capacitance changes as the sensor moves.

The electrostatic actuator is interfaced to a controller (which will be described in more details in the next chapters), and is able to apply an electrostatic force along the opposite direction to that of the displacement delivered by the thermal actuator. This consists of 12 additional fingers, which are the electrodes of a parallel plate electrostatic actuator.

Both the sensor and the actuator will be described in more details in the next sections.

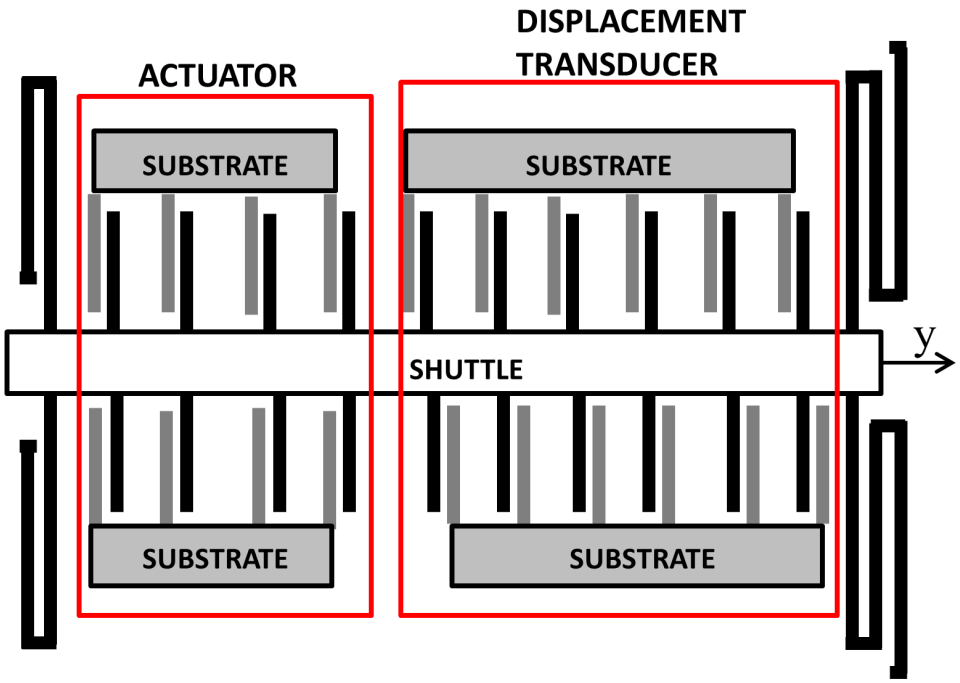

Figure 3.11: Schematic of the electro-capacitive element, consisting of an electrostatic actuator and a displacement transducer

3.3.1 The displacement transducer

The transducer is a capacitive comb-drive sensor, implementing a differential scheme, which offers as main advantage a linear relationship between the capacitance variation and the displacement (e.g., force) undergone by the sensor body.

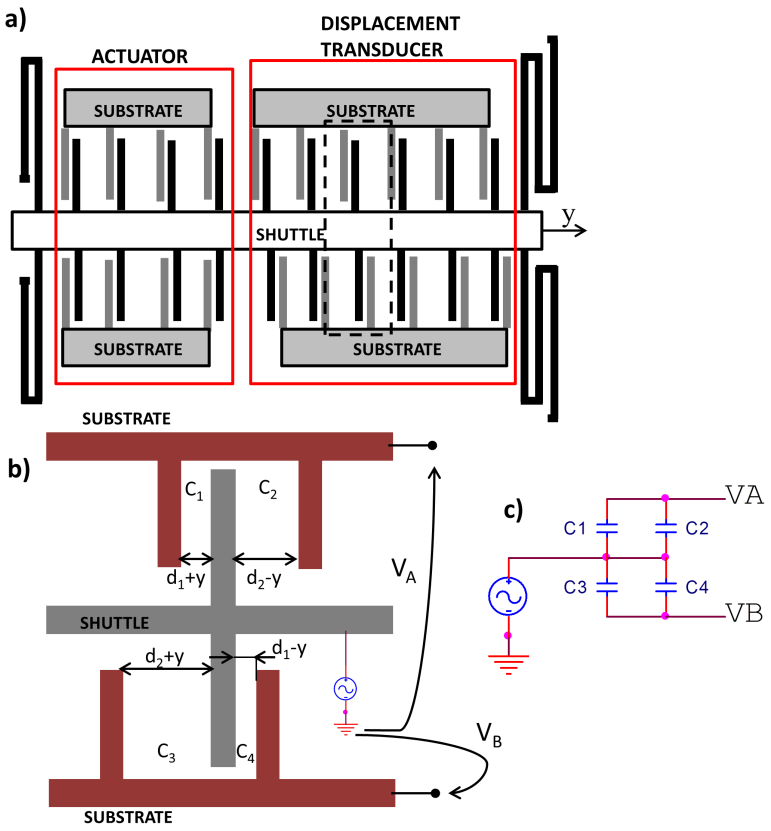

Figure 3.12: (a) Schematic of the electro-capacitive element, (b) schematic of an exemplary unit of capacitive transducer, (c) the equivalent electrical circuit representing the single unit in (b)

Between two movable fingers there is one fixed finger [162]-[165], which is not equally spaced from its neighboring movable fingers (the reason for this will be explained later) (figure 3.12).

Furthermore, the position of the fixed fingers with respect to the moving ones is not the same on both sides of the sensor (figure 3.12). In this way, as the central shuttle moves, the global capacitance on one branch increases, while the one on the other branch decreases.

An exemplary unit of the sensor consists of a pair of movable electrodes and their closest fixed neighbors. At rest, the capacitance is the same over the two branches of the unit. Thus, the output of the sensor is zero. However, any displacement y, caused by the sample when stretched by the thermal actuator, causes the following capacitive change within the unit (figure 3.12), neglecting fringe effects:

$$\Delta C = (C_1 + C_2) - (C_3 + C_4) \tag{3.30}$$

$$= \epsilon A \left[\frac{1}{d_1 - y} + \frac{1}{d_2 + y} \right] - \epsilon A \left[\frac{1}{d_1 + y} + \frac{1}{d_2 - y} \right] \tag{3.31}$$

where ϵ is the permittivity of air and A is the transverse area of the comb-drive elements. With some simplification, ΔC can be expressed as:

$$\Delta C = \epsilon A \left[\frac{2y}{d_1^2 - y^2} - \frac{2y}{d_2^2 - y^2} \right] \tag{3.32}$$

If $y^2 << d_1^2 << d_2^2$, it follows simply that:

$$\Delta C = 2\epsilon A \frac{y}{d_1^2} \tag{3.33}$$

Thus, the global capacitance change affecting the sensor, considering all its fingers is:

$$\Delta C = 2N\epsilon A \frac{y}{d_1^2} \tag{3.34}$$

being N the number of movable fingers on one side.

Thus, the displacement can be derived from measurement of a capacitance. If the device works in open-loop configuration, the sensor displacement provides the acting force (which is the same as the one experienced by the sample) if multiplied by the spring constant of the sensor[1]:

$$F = k_{LS} \cdot y \tag{3.35}$$

where k_{LS} is the equivalent stiffness of the four folded beams (figure 3.13), supporting the sensor shuttle (which can be considered as a rigid body, because of its size, which is about 60x900 μm).

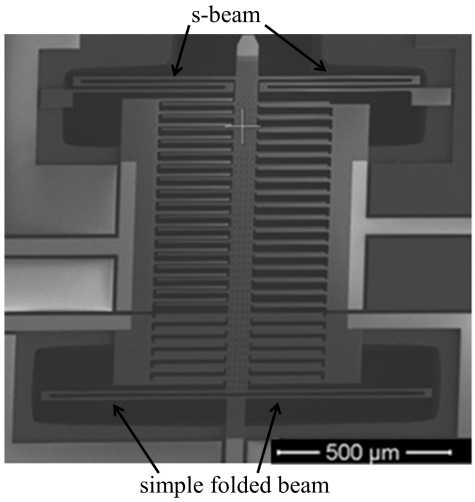

Figure 3.13: The four beams supporting the load sensor shuttle

Each beam consists of either 2 (simple folded beams) or 3 branches (s-shaped beams). Thus, the stiffness (k) of each beam has to be calculated as the

[1]In normal working conditions, the feedback control is active, thus preventing any movement of the sensor.

equivalent stiffness of 2 or 3 springs (each corresponding to one branch) in series:

$$k = \frac{1}{n}\frac{Ew^2t}{L^3} \tag{3.36}$$

being w, t, and L the width, the thickness, and the length of the supporting beams, E the Young modulus, and n the number of branches belonging to the beam. Then, the overall stiffness of the sensor can be computed as the sum of the stiffnesses of the four supporting beams, which behave like springs in parallel.

In order to improve the sensor sensitivity, its stiffness should be as smaller as possible, while the capacitance change induced by a displacement should be as higher as possible. As regards the beams stiffness, this depends on the beam size, which has to respect some fabrication limits. In fact, the thickness is forced to 25μm, while the length can be up to 500 μm, if the width is not less than 6 μm, in order to avoid curling problems.

The choice of the sensor stiffness should depend on the sample to be tested, since in an open-loop configuration they behave as springs in series. Thus, smaller the sensor stiffness, higher the displacement transferred to the sensor, meaning smaller deformation undergone by the specimen. A good compromise between sensor sensitivity and specimen strain can be obtained with a sensor stiffness of 25-30 N/m [153], which corresponds to a force sensitivity of 25-30 nN. In order to get such value, considering that both the s-springs and the simple folded beams contribute with the same spring constant, they should have the following size:

Length of the s-beam, $L_s = 420\,\mu$m

Length of the folded beam, $L_f = 480\,\mu$m

Width of the beams, $w = 7\,\mu$m

Thickness of the beams, $t = 25\,\mu$m

Under these conditions, the sensor stiffness is 26 N/m.

With reference to stress state, each branch of either the folded or s-beams undergoes a transverse load. In particular, the most stressed branch is the one fixed at one end to the substrate. The maximum stress in its most critical point is then:

$$\sigma = \frac{M \cdot w/2}{I} \tag{3.37}$$

The most stressed branch can be modeled as a clamped-guided beam, loaded at the guided end with a force F, which produces a maximum moment (M) of $F \cdot l/2$, being l the length of the beam [166]. In the present case, considering the previous parameters, and a maximum force of 100μN (which is the maximum force the present device is assumed to work with) $\sigma_{max} = 90$ MPa, which is well below the fracture stress of Silicon, being few GPa [162]-[153].

However, the design of the transducer springs plays a minor role in the present device, since this is supposed to work in a closed-loop configuration (e.g., the sensor should not move). Thus, the springs are marginally stressed during a test. Nevertheless, it can be useful to design the transducer to work in open loop configuration, too.

Thus, the most significant option to improve the sensor sensitivity (e. g., the capacitance change given by equation 3.34) is to decrease the gap between the fixed and the movable fingers (d_1), and increase their transverse area (A). For fabrication limits d_1 cannot be smaller than 2μm. Thus, $d_1 = 2\mu$m. Furthermore, in order for the (3.34) to be valid, d_2 should be much bigger

than d_1. However, bigger d_2 larger the structure of the load sensor and, thus, the overall size of the device. As a trade-off, d_2 is chosen to be 20 μm. Another way to increase the sensor sensitivity is to increase the electrodes area (A), which is:

$$A = l \cdot t \tag{3.38}$$

where l and t are the length and the thickness of one electrode, respectively. The thickness of the displacement sensor is the thickness of the MEMS structural layer, which cannot be larger than 25 μm for fabrication limits. The length is chosen in order to not exceed the length of the actuator. Thus, 200 μm can be considered as a good value. Considering the aforementioned dimensions, and a number of fingers equal to 34, according to the (3.34) the sensor sensitivity results to be about 0.38 fF/nm (which is one order of magnitude bigger than the sensitivity of the load sensor in the previous design [153]).

In order to detect the capacitance difference characterizing the transducer, the current flowing in each branch is amplified, and then the difference between these two signals is acquired, and used to compute the proper voltage to be applied to the electrostatic actuator in order to keep the balance.

3.3.2 The electrostatic actuator

The electrostatic actuator is a parallel plate actuator, whose function is to apply the necessary force to keep the transducer body at rest (figure 3.14). Like the transducer, it consists of a central shuttle, with protruding electrodes interdigitated with corresponding fixed electrodes.

When a voltage difference is applied between the moving and fixed plates, the moving electrodes come close to these latter, thus moving the actuator

body. Since the force to be generated has to act in the opposite direction to the one stretching the sample, the location of the fixed electrodes with respect to the corresponding movable ones is the same on both sides.

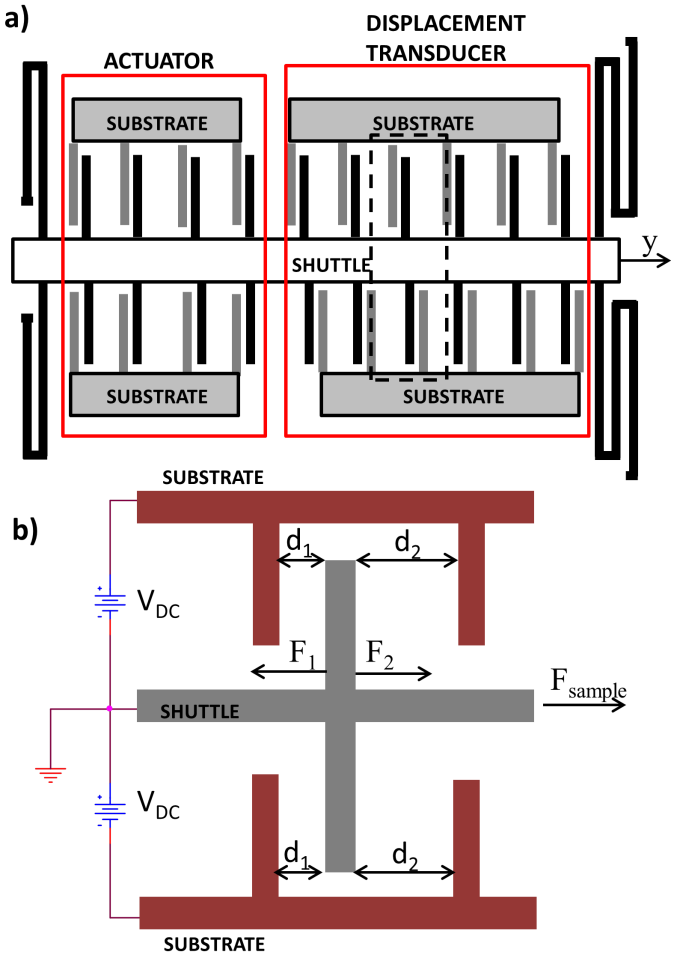

Figure 3.14: (a) Schematic of the electro-capacitive element, and detailed in (b) an exemplary unit of the electrostatic actuator

In order to derive an expression for the force this electrostatic actuator can

generate, it is useful to start the analysis from considering a simple unit (figure 3.14(b)). When a DC voltage is applied between the fixed and the moving electrodes, two electrostatic forces act on the shuttle in opposite direction. They are [167]:

$$F_1 = \frac{1}{2}\epsilon V^2 \frac{lt}{d_1^2} \tag{3.39}$$

and

$$F_2 = \frac{1}{2}\epsilon V^2 \frac{lt}{d_2^2} \tag{3.40}$$

In the above, ϵ is the vacuum permittivity, V the applied DC voltage, l and t are the electrode length and thickness, respectively.

In order to minimize spurious effects, F_2 should be as smaller as possible with respect to F_1, acting in the same direction of the tensile load. Since such forces scale with the inverse of the square distance between the moving and the fixed electrodes, it is sufficient that d_2 is one order of magnitude bigger than d_1. Furthermore, in order to achieve higher forces, d_1 should be as smaller as possible. The fabrication process limits all the features to be bigger than 2 μm. Thus, the following parameters are chosen:

- $d_1 = 2\,\mu$m
- $d_2 = 20\,\mu$m

The global force generated on the sensor shuttle, taking into account all the electrodes is:

$$F_A = \frac{1}{2}N\epsilon V^2 \frac{lt}{d_1^2} \tag{3.41}$$

being N the number of electrodes. In the present design,

N=12

which allows for generation of an actuating force of about 100 μN at V=40V, which is sufficient to break a variety of nanowires. For example, considering a

silver nanowire (Young modulus of 83 GPa [184]) with circular cross-section and diameter of 100 nm, and gage length of 4 μm, the force to be applied to reach 5% strain is about 31 μN, or for a GaN nanowire (Young modulus of 300 GPa [158]) with hexagonal cross-section and diameter of 70 nm, and gage length of 4 μm, the force to be applied to reach 5% strain is about 48 μN (for simplicity assuming elastic behavior until fracture in both cases). When the actuator is biased, the moving fingers move toward the fixed ones, and the shuttle of the whole electro-capacitive element moves accordingly. Thus, on neglecting the stretching of this latter (which can be considered rigid according to the present geometry), the shuttle can be considered to come back to its initial position.

3.4 Other versions of the new testing device

The device previously described (figure 3.15a) was slightly modified in order to design a small variety of devices, each with only one difference with respect to the basic structure. In particular, there are four alternative versions.

In the first case, the variation is the absence of the electrical isolation of the sample from the thermal actuator and the sensor. This is a kind of safety design, which can be fabricated with the standard and well-assessed SOI process; whereas, the insulating feature requires a modification in the classical process flow (shown in the next section), which is adopted for the first time for production of the device previously described.

In the second chip, the v-shaped beams of the thermal actuator are inverted, in order to apply a compressive load to the sample instead of a tensile load (figure 3.15b)

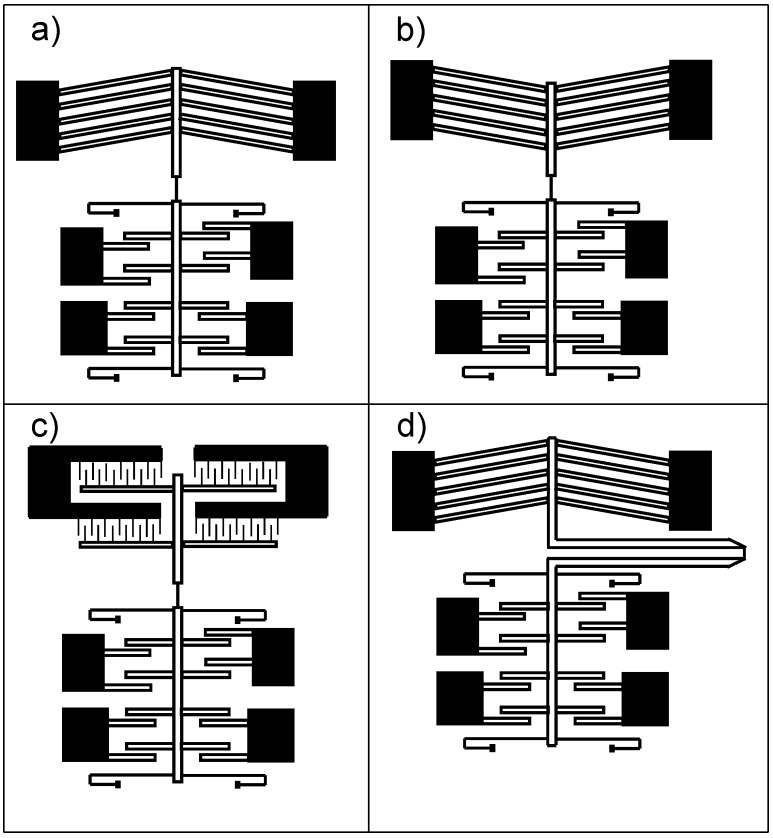

Figure 3.15: Schematics of the designed devices

The third chip has a parallel comb-drive actuator instead of a thermal actuator (figure 3.15c). This was introduced in order to have the possibility to perform dynamic tests. From a structural point of view, it is provided with nine rows, each containing 60 parallel freestanding electrodes, connected to a central shuttle, and interdigitated with corresponding fixed electrodes. Thus, when a voltage is applied between the fixed and movable electrodes, an electrostatic force is generated, which moves the actuator body, and thus the specimen end attached to it. However, unlike the electrostatic actuator

implemented in the electro-capacitive unit, where the electrodes move along a transverse direction, in this case they move parallel, with no gap variation. Such electrodes are 20 μm long, 2μm thick and wide, and the corresponding force they can generate is:

$$F = \frac{1}{2} N \epsilon_0 \frac{t}{d} V^2 \tag{3.42}$$

where N=1080 is the number of electrodes, ϵ_0 the vacuum permittivity, t the electrodes thickness, d the gap between a movable and a fixed electrode, and V the bias voltage. When applying a voltage of 40V, the corresponding force is about 96μm, which is sufficient to break a variety of nanostructures, as shown in the previous section.

The last device has no electrical isolation of the sample, but in correspondence of the area where it should be attached, there are two protruding arms, which behave like a tweezer (figure 3.15d). Those are about 300μm long and are completely freestanding. This is a new feature introduced with the aim to pick the sample up directly with the chip, without using an external manipulator[2].

3.5 Fabrication process

As already anticipated, the process considered for fabrication of the present MEMS is Silicon-On-Insulator (SOI). Such process was chosen since it provides a device structural layer with thickness of tens of micrometers, which is necessary for the electrostatic actuator belonging to the electro-capacitive element to generate sufficient force to break the sample. Fabrication was carried out by an external foundry, the MEMSCAP (Crolles Cedex, France),

[2]The procedure for mounting a sample on the device will be shown in the last chapter.

and even if this is a standard process in microfabrication practice, each company has developed its own protocols. Thus, this section illustrates the SOI process flow as particularly performed by the MEMSCAP [168].

Figure 3.16: Initial SOI structure

The initial structure from which fabricating the device is a wafer (whose generic cross-section is shown in figure 3.16) with three layers:

1. On top, there is either a 10 μm or 25 μm-thick Silicon layer, which is the structural layer of the device. This usually includes its major features, like its freestanding and movable parts;

2. In the middle, there is a 2 μm-thick layer of buried Silicon Oxide. This is an insulating layer, which can provide electrical insulation between features on the silicon layer, which is instead conductive;

3. A 400 μm-thick layer of Silicon, which is the substrate of the device, with supporting and handling function.

SOI process consists of a standard sequence of deposition and photolithography operations, shown in figure 3.17 with reference to the cross-section of a generic MEMS device. However, before analyzing each step in details, it is worth to mention that the flow in figure 3.17 shows an additional custom step (step n.5) which is not included in the standard process. Such step was

properly designed in this work and introduced for fabrication of the present device. The steps of the fabrication process are listed below and shown in figure 3.17:

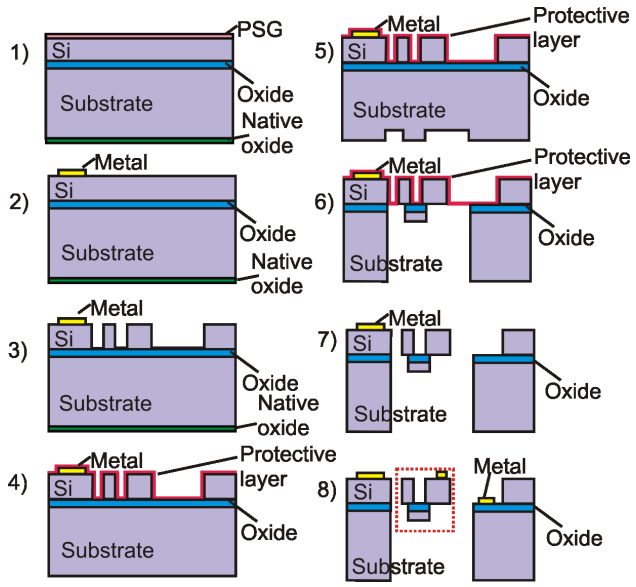

Figure 3.17: Steps of SOI fabrication process: 1) Doping of the Silicon structural layer with PSG; 2) first metal deposition; 3) etching of the Silicon structural layer; 4) removal of the protective layer; 5) partial etching of the substrate with removal of the native oxide layer; 6) final etching of the substrate; 7) release of the freestanding structures; 8) second metal deposition, where highlighted, with a dashed line, those freestanding structures electrically isolated while still mechanically connected.

1. Deposition of a phosphosilicate glass layer (PSG) for doping of the Silicon structural layer. PSG is then removed (figure 3.17(1));

2. First metal deposition for definition of connection pads and traces (figure 3.17(2));

3. Patterning of the silicon structural layer through DRIE (Deep Reactive Ion Etching) (figure 3.17(3)), in order to define the main features of the device;

4. Deposition of a protective layer on the silicon structural layer (figure 3.17(4));

5. Partial etching of the Silicon substrate (additional step with respect to the standard flow) (figure 3.17 (5));

6. Patterning of the Silicon substrate by DRIE, while the silicon structural layer is still covered by the protective layer (figure 3.17 (6));

7. Removal of the protective layer and release of the freestanding structures on the silicon structural layer (figure 3.17(7));

8. Second metal deposition for definition of metal features with coarser tolerance. This layer was used to pattern a film of gold in the area where the specimen will sit. (figure 3.17(8)).

The additional step (n. 5 in figure 3.17) adopted for fabrication of the present device is necessary in order to fabricate freestanding structures, which are electrically isolated, while still mechanically connected. This was considered necessary in the design reported herein, since in this way it is possible to electrically isolate the regions where the sample is mounted (thermal actuator shuttle on one side and displacement sensor shuttle on the other) from the remaining of the device. Such solution can be in prospective very important, since it provides a separated electrical access to both ends of

the sample. This is a necessary requirement for performance of coupled electromechanical tests in future.

3.6 The masks

In order to define the proper features of the present device, each layer of the SOI wafer had to be carefully designed. To this aim a specialized software, L-edt (by Tanner Tool) was used. This in fact provides drawing tools for definition of the pattern (mask) which has to be reproduced on each layer of a MEMS device.

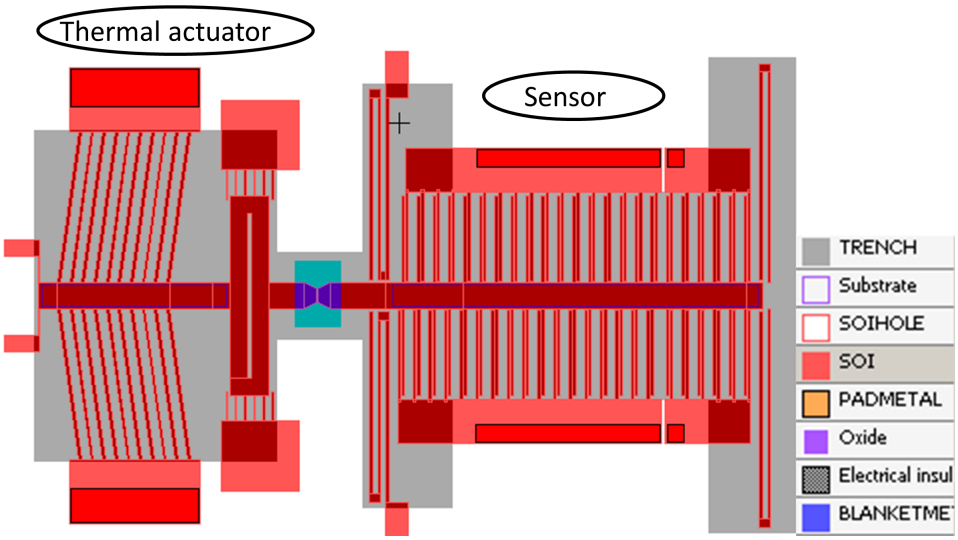

Figure 3.18: One of the testing device designed in L-edit environment

The requirements which have to be accomplished for definition of the proper masks for the present device are:

- Since both the electro-capacitive element and the thermal actuator have to be freestanding structures, they had to be totally included within the structural Si layer, and the substrate beneath had to be completely etched;

- The two branches of the actuator inclined beams, the two sets of fixed fingers belonging to the displacement transducer, the two sets of fixed fingers belonging to the electrostatic actuator, and the shuttle of the electro-capacitive element, had to be connected through conductive lines to separate pads. These pads provided connections between the MEMS features and external instrumentation;

- In order to obtain fine fabrication tolerances, all the pads and the conductive lines were defined during the first step of the SOI process (first metal deposition).

L-edit allows for definition of features on six levels:

1. TRENCH. Here, it is possible to draw the portion of Si substrate which has to be removed;

2. SUBSTRATE. It allows for definition of the substrate boundary. In the present design such layer is not considered;

3. SOIHOLE. This layer is used for definition of etching holes on the Si structural layer. The holes are in general introduced in freestanding features, in order to improve etching of the layers underneath;

4. PADMETAL. This allows for definition of metal features with fine tolerance;

5. OXIDE. This allows for definition of features on the oxide layer. It is not used in the present design;

6. BLANKETMETAL. This allows for definition of metal features fabricated with coarse tolerance.

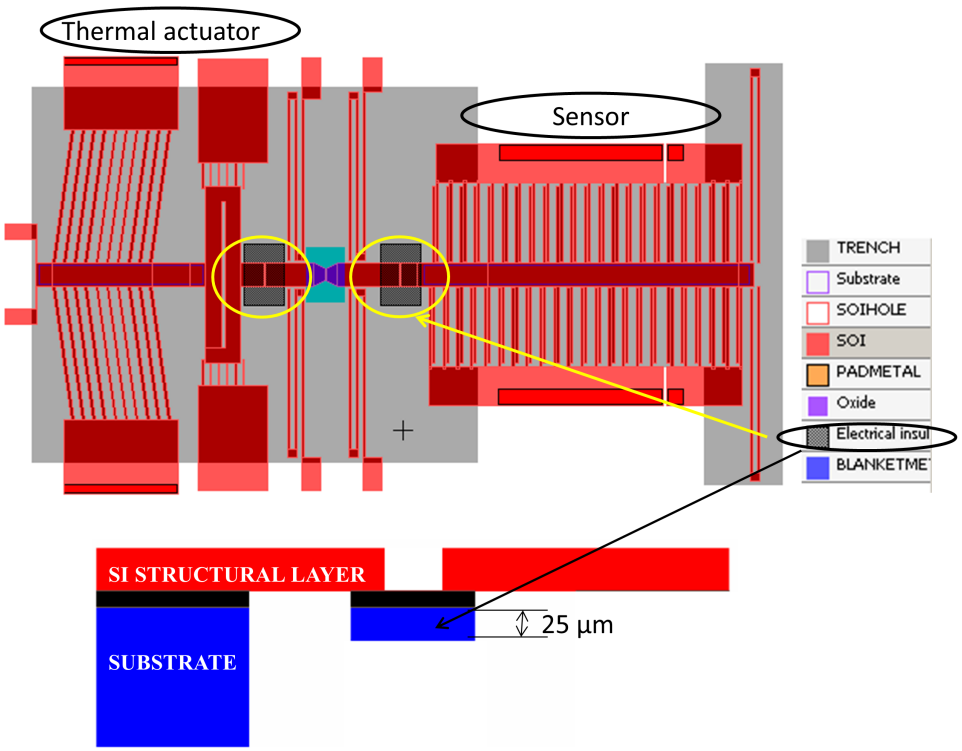

Figure 3.19: Testing device designed in L-edit environment, which allows for electrical insulation of the sample

Figure 3.18 shows how the present MEMS device with no sample electrical isolation looks like in L-edit environment. This was designed using the usual layers adopted in the standard process, and following all of the steps shown in figure 3.17, except step n.5. However, as already mentioned, such process had to be slightly varied in order to guarantee sample isolation, which is

possible with the availability of freestanding structure electrically isolated, while still mechanically connected. Since there is just one insulating (e.g., oxide) layer, the only way to accomplish such requirement is to not completely remove the substrate underneath the region of interest (figure 3.19), thus introducing step n.5 (figure 3.17) in the standard process flow.
In L-edit environment this is done by the introduction of an additional layer, which defines the area of only partial etching of the substrate, which is in correspondence of the region where the sample is attached to the actuator and the sensor (figure 3.19).

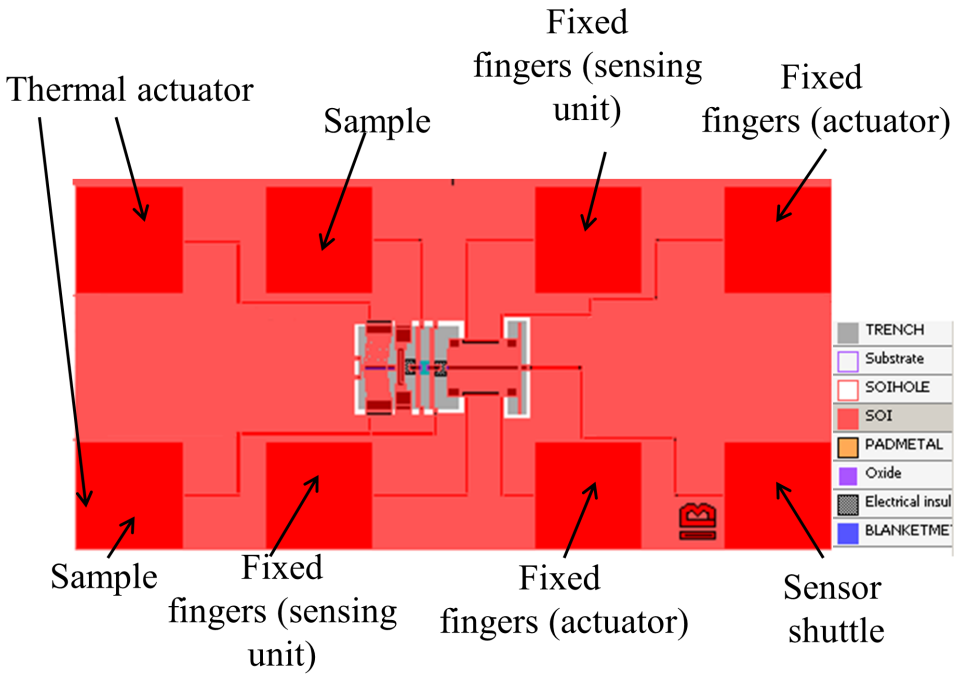

Figure 3.20: Routing of the MEMS device

As said, it is necessary to connect each device structure to a separate pad through proper routing, as visible in figure 3.20, which shows both the con-

ductive lines and the pads corresponding to the thermal actuator, displacement sensor, and electrostatic actuator of the device in central position.

3.7 The dies

The overall size of the devices is less than 2x1 mm^2, and they are fabricated from an SOI wafer, which is thousands of millimeters square. Thus, many devices can be accommodated on the same wafer. For ease of handling and designing, it is common practice to divide the wafer in several units (dies). Each die has an area of 9x9 mm^2. In the present design, three different dies were designed (labeled on the chip with proper deposition of metal as die A, die B, and die C), each including a specific number and variety of MEMS devices (figures 3.21, 3.22, and 3.23). Dies B and C contains six devices, while die A eight devices. All of the dies have a subdicing line at the middle, which allows to easily divide one half from the other after fabrication. In particular, the right subdie A has two additional horizontal subdicing line, to facilitate separation of those devices with the tweezer protruding arms (figure 3.21).

Figure 3.21: Die A

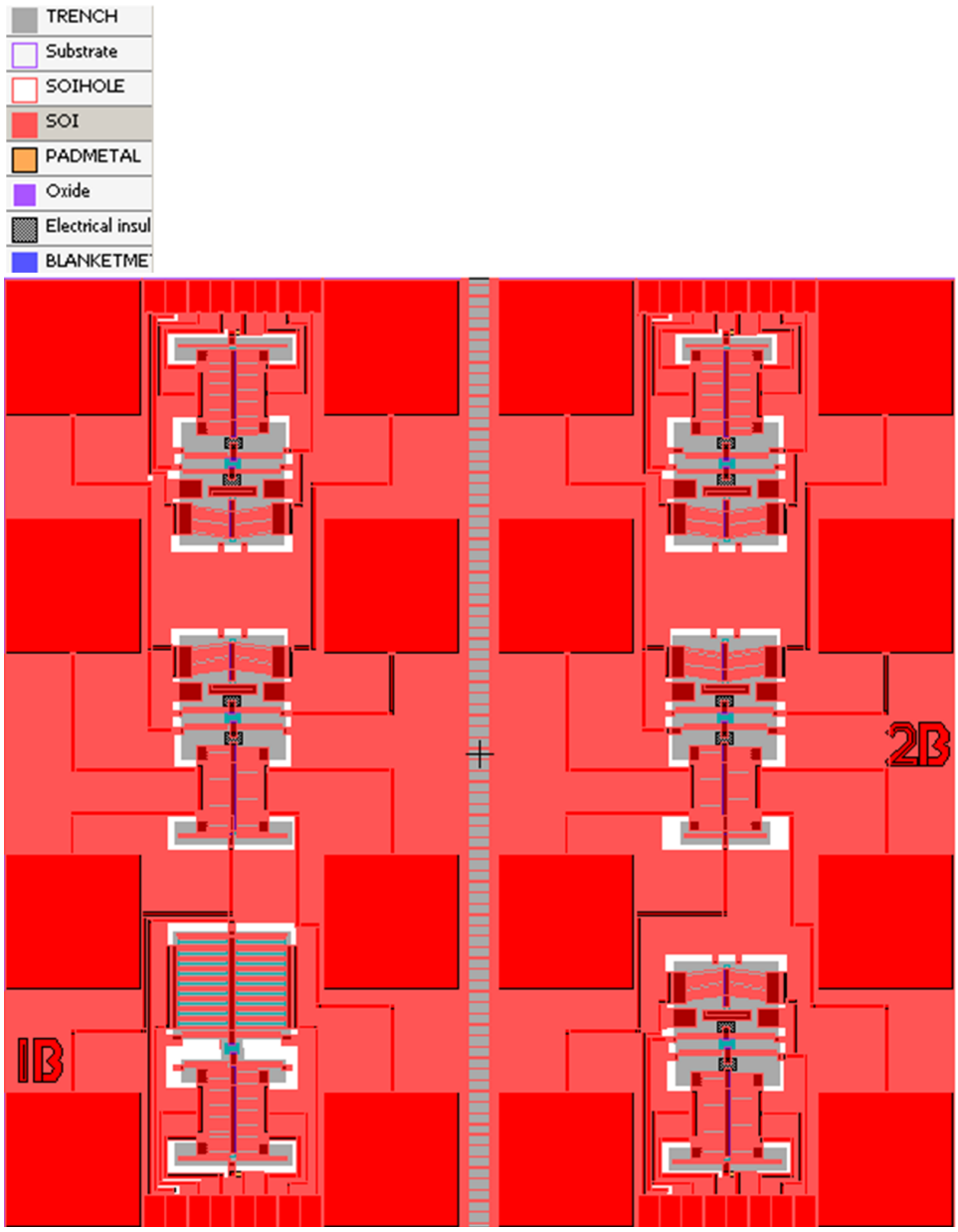

Figure 3.22: Die B

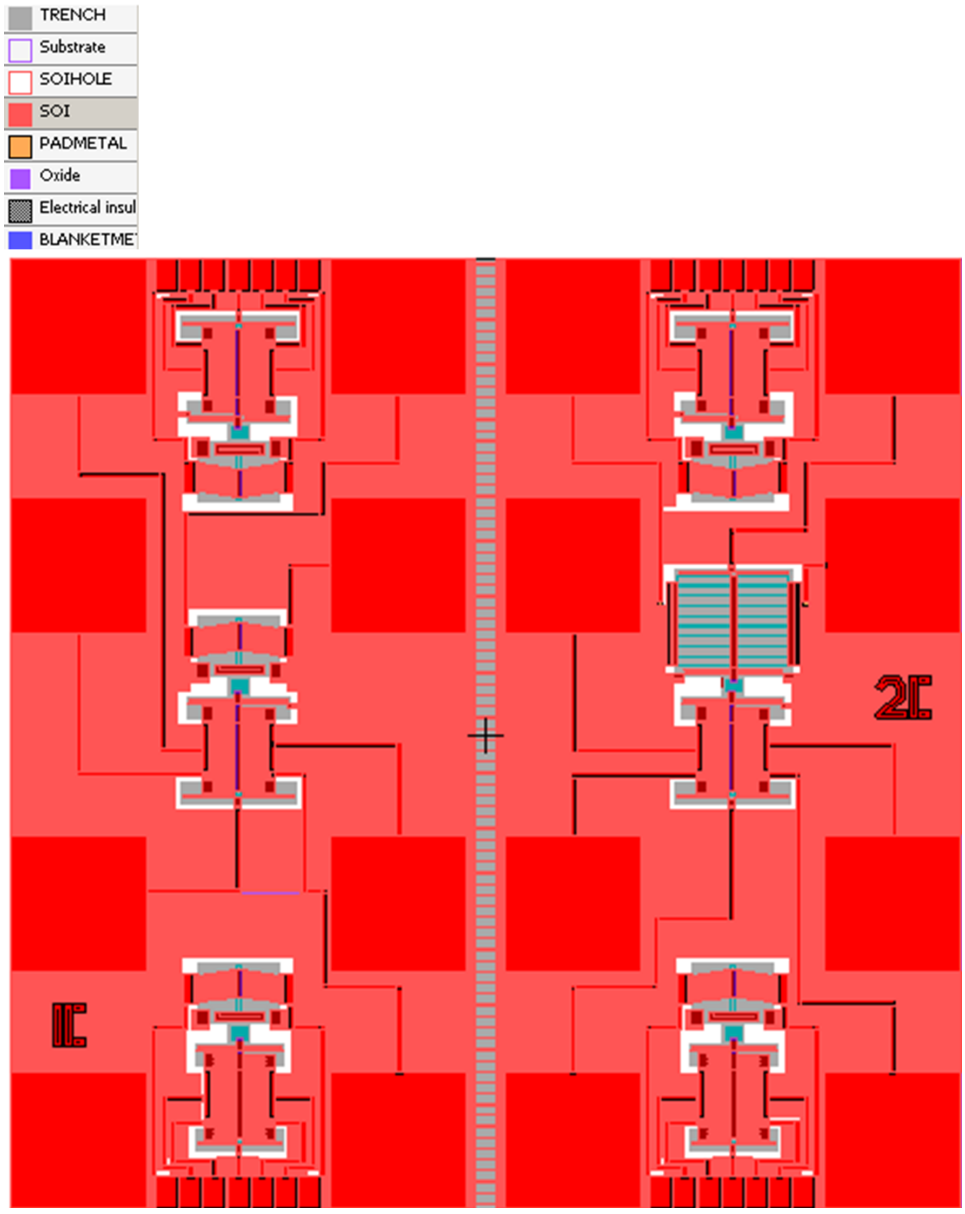

Figure 3.23: Die C

Chapter 4

Feedback control loop for load measurement

4.1 Feedback control systems in MEMS devices

Introduction of feedback systems has become common practice in MEMS devices, including accelerometers [170], gyroscopes [171], micromirrors [172], actuators [173], and positioners [174]. In fact, even if the implementation of closed-loop schemes increases the system complexity, this is counterbalanced by the dramatical improvement of the device performance, in terms of bandwidth, linearity, and resolution.

Figure 4.1 shows the basic working principle of a closed-loop system with a position feedback control. In particular, some external excitation (like the acceleration to be measured in an accelerometer) moves the system of interest (e.g., the seismic mass of an accelerometer/gyroscope, a micromirror) away from its equilibrium position, thus causing a displacement. Then, from the knowledge of such displacement, a properly designed controller deter-

mines what is the force which has to be applied to the system to bring it back to rest.

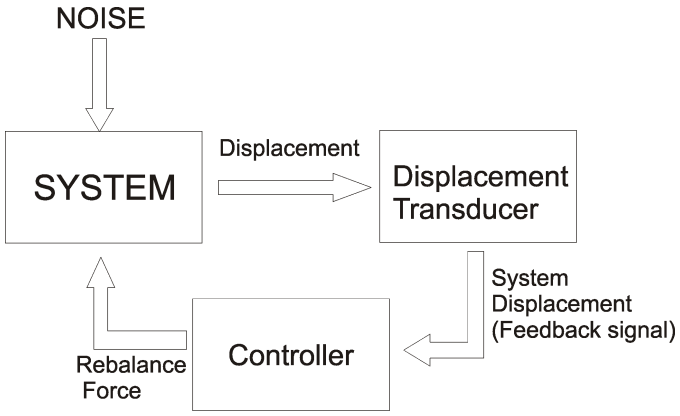

Figure 4.1: Basic working principle of position feedback control

In MEMS applications, the nature of the balance force is usually electrostatic, since electrostatic actuators can be easily and effectively fabricated within microdevices. More complex is instead the actual implementation of the feedback branch.

First of all, a necessary condition is to have on-chip displacement sensing capability [175]. In fact, only in this way it is then possible to provide the information of the system displacement as input to the controller.

The controller can be designed according to different architectures. The simplest one includes low-order controllers, like proportional (P) or proportional-integral-derivative (PID) controllers. The main advantage they offer is the ease of implementation, even if a correct tuning of their parameters can be difficult to achieve, and the high non-linearity of some applications require more sophisticated solutions [176]. Nevertheless, in most of the cases, a PID

provides a good trade-off between performance and design complexity [173]. With reference to PID working principle, a signal proportional to the system displacement is compared to a reference value corresponding to the equilibrium position. Then, the difference between these two signals is provided as input to the controller, which on turn computes the signal (e.g, electrostatic force in the case of position feedback control) to be applied to the system in order to bring it back to equilibrium.

In open-loop schemes of for example position transducers or accelerometers, the external excitation is the unknown quantity to be measured, and this can be directly determined from a measurement of their sensing element displacement. However, on switching to a closed-loop scheme, such measurement procedure is no longer possible, being the sensing element constantly at its rest position[1]. In this case, the information about the external excitation, which is rejected like a noise, can be tracked through the variation of the balance force. This in fact varies according to the noise, and is proportional it.

4.2 Feedback control system in the testing device

As already mentioned, position feedback control of the specimen side connected to the displacement sensor can enhance the performance of the device. Figure 4.2 shows how a position feedback control system of the displacement sensor is implemented in the present application.

In this case, the external disturbance (which has to be rejected) is the displacement induced on the electro-capacitive element by the sample, when this is stretched by the thermal actuator. Then, in order for the electro-

[1]Even if a slight variation from the equilibrium position can be allowed.

capacitive element to maintain its initial position, the force transmitted through the sample is balanced by the electrostatic force generated on biasing the electrostatic actuator with a proper voltage computed by the controller.

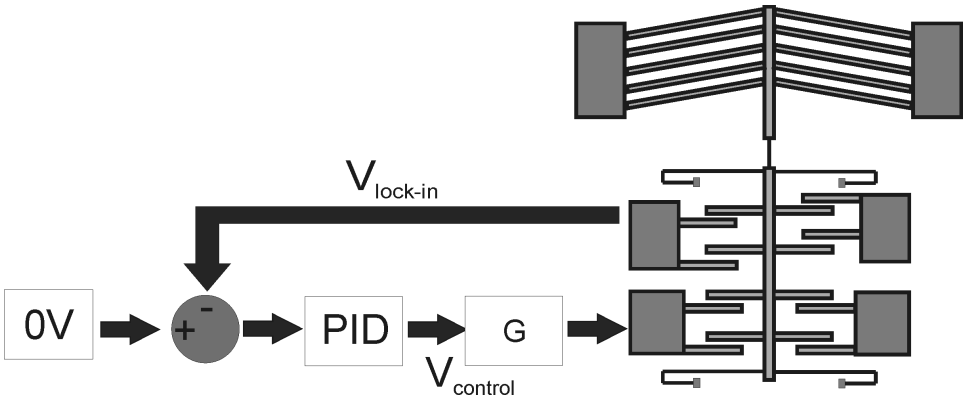

Figure 4.2: Working principle of the position feedback control system implemented in the present device

When there is no sample (e.g., the sample is not stretched), the two branches of the displacement sensor are balanced, and the output voltage on the lock-in amplifier[2], which is connected to them, is 0V. As opposed to that, when the sample transmits a force to the load sensor, its two capacitive branches are no longer balanced and, as a consequence, there is a change in the lock-in amplifier output. Thus, the 0V output of the lock-in amplifier can be chosen

[2]As it will be explained with more details in the next chapter, the two branches of the displacement sensor are connected with an appropriate electrical circuit to a lock-in amplifier. This provides as output a voltage, which is proportional to the capacitance variation produced by the displacement sensor. Then, since this capacitance variation is proportional to the sensor displacement, the lock-in amplifier output voltage is proportional to this, too.

as reference voltage, corresponding to the equilibrium state. In particular, the actual lock-in amplifier output voltage (feedback variable indicated as $V_{lock-in}$ in figure 4.2) can be compared to 0V, and the difference between them (e.g., 0V-$V_{lock.in}$) is the parameter the controller has to consider in order to decide what is the voltage to apply to the electrostatic actuator (control variable), in order to reject the external disturbance (e.g., the cause of the electro-capacitive element displacement).

Figure 4.3: The data acquisition card used to acquire and generate voltages in the present design

Furthermore, since the electro-capacitive unit is kept at equilibrium, even though subjected to two forces (the electrostatic force generated by the actuator and the force transmitted by the sample), it follows that such two forces are equal. Thus, the control voltage, which is related to the corresponding electrostatic force generated by the actuator, provides a measurement of the force on the sample.

As regards the controller, it was decided to consider a PID, because of the good compromise between ease of design and efficiency, as it comes from the

literature analysis shown in the previous section.

All of the operations the controller has to perform are carried out inside virtual instruments (VI), properly designed in LabView®. Since such operations require acquisition and generation of signals from/to systems (e.g., the device or other instrumentation, like the lock-in amplifier) which are outside the software environment, the personal computer running the LabView VIs is interfaced to a data acquisition card compatible with this software. This is the model NI6009 by National Instruments, as shown in figure 4.3. This can be directly connected to a laptop through a USB port, and is provided with a variety of sockets for accommodation of terminals for acquisition and generation of signals (they are aligned and numbered on both sides of the card). However, since this card is not able to apply voltages higher than 5V, its output is amplified by a custom-made amplification circuit, in order to provide the electrostatic actuator[3] with bias voltages up to 40V.

4.3 Virtual instruments developed in LABVIEW® environment

The software considered for implementation of the controller was LabView. This in fact is a graphical programming environment which is particularly suitable to exchange signals with external instruments. In this particular case, this was interfaced with the data acquisition card previously shown, which makes available in the software routines the thermal actuator bias voltage and the lock-in amplifier output voltage, while being able to apply

[3]In chapter 3, it was shown that the maximum force generated by the electrostatic actuator when biased with 40 V is 100μN, which is sufficiently high to balance the force needed to break a variety of material samples.

the computed control voltage. In particular, two routines (Virtual Instruments) were programmed with the following tasks:

- The feedback control VI acquires and records the input voltage to the thermal actuator (which was varied manually) and the output voltage from the lock-in amplifier. This latter is then given as input to the PID controller implemented into the PID VI, and receives from it the voltage which the DAQ card is indicated to apply;
- The PID VI receives as input the lock-in output voltage and perform all the necessary computation to define the bias voltage of the electrostatic actuator to guarantee the balance of the electro-capacitive unit.

Both of these VIs will be discussed in details in the following sections.

4.3.1 Virtual instrument for feedback control

The block diagram of the implemented feedback control VI is shown in figure 4.4. One of its main components is the block called 'DAQ ASSISTANT'. This in fact allows for interface with the data acquisition card. In particular, by double-clicking on its icon, a dialog window opens, which allows for choice of either acquisition or generation of a voltage signal. Furthermore, it is possible to choose which terminals are involved in the process. In the present design, the same 'DAQ ASSISTANT' allows for acquisition of two signals, referring to the voltage applied to the thermal actuator pads and the output voltage of the lock-in amplifier, respectively. Both of the signals are then visualized in graphical format (wavechart blocks called 'VTA' and 'Vlock-in', respectively) and recorded in a text file for further processing ('Write to MeasurementFile2').

The lock-in output voltage is then compared with a reference voltage (Vref), and the difference is visualized in graphical format, recorded into a a file, and given as input to the PID block, which will be described in more details in the next section. This receives other three input values, which correspond to the gain of the proportional term, the gain of the integral term, and the gain of the derivative term necessary to define the PID controller. These are specified by the user.

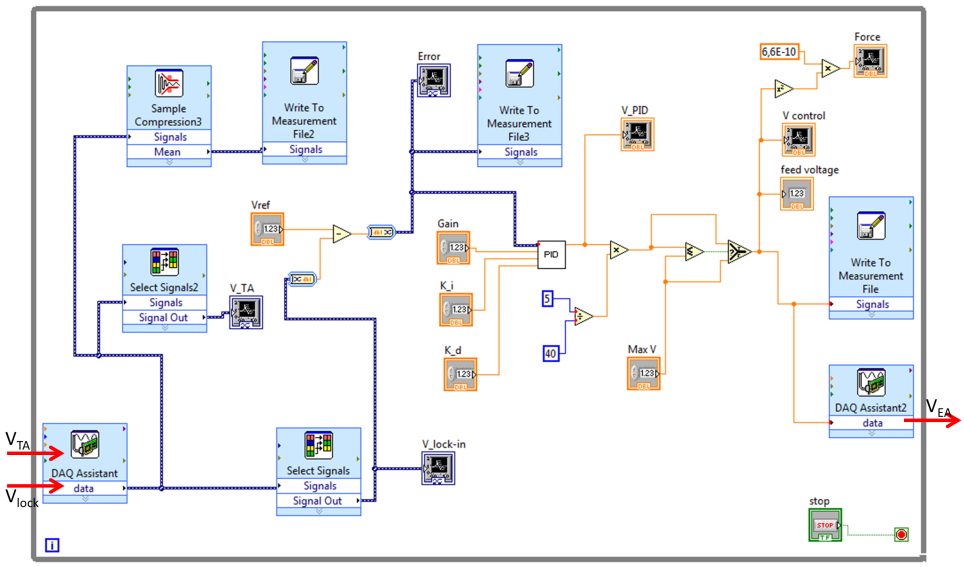

Figure 4.4: Block digram of the VI implementing the complete closed-loop

The output signal of the controller is then divided by a scaling factor. This is necessary since the data acquisition card is not able to generate signals higher than 5V. Thus, since the maximum voltage to be applied to the electrostatic actuator is 40V (in order to apply sufficiently high forces, as already shown in chapter 3.), the value computed by the controller has to be scaled by 8. Furthermore, in order to have a better control on the generated

voltage, the scaled signal is compared to a reference value, which can be 5V or less. In particular, especially during preliminary tests on the device in presence of a sample, such reference value is set to 1-2V in order to be sure to not apply too much force to the sample. In fact, the reference value is compared to the scaled PID output voltage, and the smaller between them is visualized, recorded in a text file and, finally, generated by the data acquisition card ('DAQ ASSISTANT2'). The square of this same voltage is then multiplied by a constant in order to compute the corresponding electrostatic force, which is applied by the actuator, and visualized in graphical form.

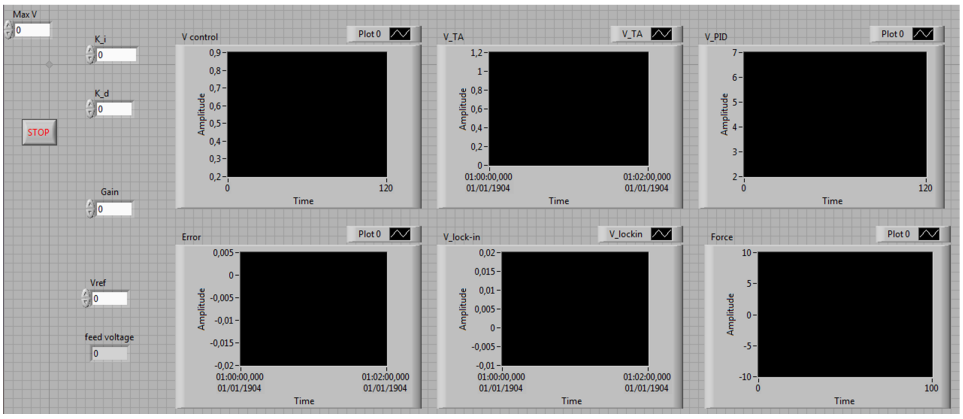

Figure 4.5: Front panel of the VI implementing the feedback control system

Figure 4.5 shows the front panel corresponding to the block digram described up to now. This is the actual interface between LabView operations and the physical user. In particular, in this environment the user can see six tables, reporting the time evolution of the thermal actuator bias voltage, the lock-in output voltage, the error signal (e. g., minus the lock-in output voltage), the control voltage, the (scaled) control voltage effectively applied by the

card, and the electrostatic force.

Furthermore, it is possible to enter the values for parameters, like the reference voltage to be compared with the actual lock-in voltage, the maximum voltage which has to be applied, the gain of the proportional term, the gain of the integral term, and the gain of the derivative term of the PID.

In particular, the real time plotting of the signal of interest is useful for a better monitoring of the system during the test.

4.3.2 Virtual Instrument for PID simulation

The controller implemented in the present VI follows the architecture of a classical proportional-integral-derivative (PID) controller (figure 4.6).

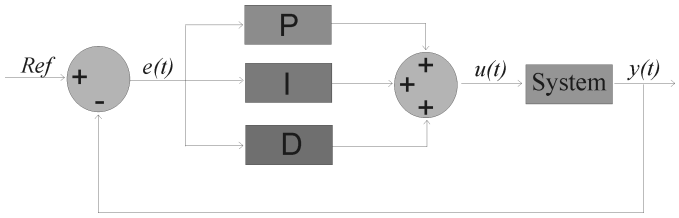

Figure 4.6: Architecture of a PID controller

In particular, the signal of interest ($y(t)$), which is proportional to the system displacement, is compared to a reference value, corresponding to no displacement. The difference between them ($e(t)$) is then provided as input to the controller. This multiplies, integrates, and derivates such error function $e(t)$, and sums all the results from these operations ($u(t)$). The output of the controller is then provided to the system (e. g., the electrostatic actuator) in order to bring it back to the initial equilibrium position.

The PID transfer function consists, thus, of the sum of three terms:

$$u(t) = K_p \cdot e(t) + K_i \int_0^t e(\tau)\mathrm{d}\tau + K_d \frac{\mathrm{d}}{\mathrm{d}t} e(t) \tag{4.1}$$

being K_p the proportional gain, K_i the integral gain, and K_d the derivative gain.

The block diagram of the PID VI is reported in figure 4.7.

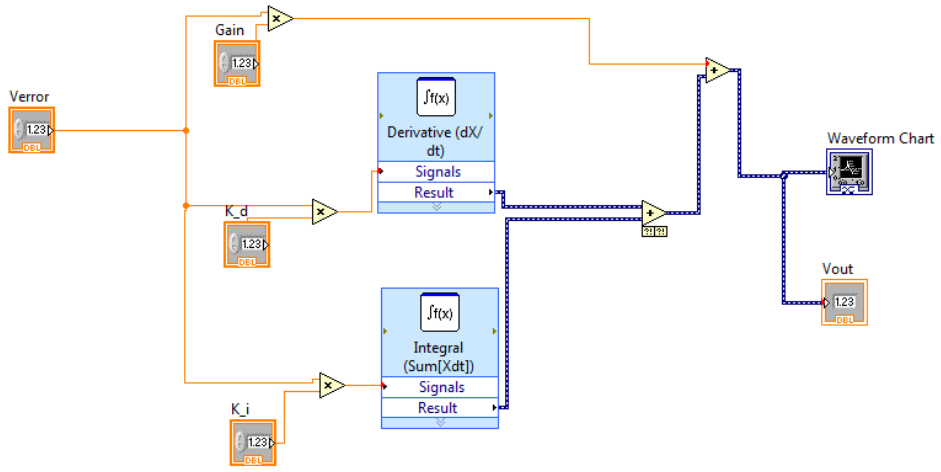

Figure 4.7: Block digram of the VI implementing the PID controller

This contains three main blocks which perform a product by a constant (Gain), integration and product by a second constant (Ki), and derivation and product by a third constant (Kd) of the input signal (V_{error}), and provides as output the sum of the results of these mathematical operations (V_{output}). For completeness, there is also a block for visualization of the output in graphical format (Waveform chart block).

The values of the constants K_p (proportional gain), K_i (integral gain), K_d (derivative gain) depend on the characteristics of the system under control, and can be tuned with different approaches. Among these, two very com-

mon techniques are known as methods of Ziegler-Nichols [177].

According to the first of these techniques, the system in open-loop configuration (e. g., without the controller) (figure 4.8a) is stimulated by a step excitation, and from the analysis of its response (figure 4.8b), the delay time L and the time constant T can be identified, as shown in figure 4.8c. From L and T, K_p, K_i, an K_d can be computed as:

$$K_p = 1.2\frac{T}{L^2}$$
$$K_i = 0.6\frac{T}{L^2}$$
$$K_d = 0.6T$$

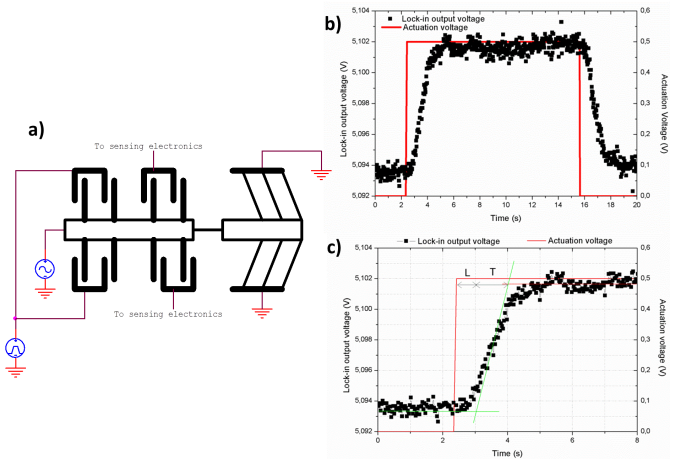

Figure 4.8: a) Electrical connections for tuning the PID parameters according to the first Ziegler-Nichols method; b) Step response of the closed-loop system, whose initial section is detailed in c)

As regards the second method, first both the integral and derivative gain are

set equal to zero. Then, the proportional gain is increased until the onset of instability (e.g., high oscillation). Then, the oscillation period (P_{cr}) and amplitude (K_{cr}) are recorded and used to compute the values of K_p, K_i, an K_d, according to the following expressions:

$$K_p = 0.6 \cdot K_{cr}$$
$$K_i = 1.2 \frac{P_{cr}}{2}$$
$$T_d = 0.075 K_{cr} P_{cr}$$

In the present case, the first methodology was adopted, as it will be shown with more details in the application reported in the next chapter.

4.4 Amplification circuit

The data acquisition card is able to provide as output voltage signals not higher than 5V. Since the voltage needed to keep the displacement sensor at its equilibrium position is expected to be much higher during a real test, it is necessary to amplify such signal. Furthermore, as it will be explained in the next chapter, the shuttle of the electro-capacitive unit is biased with an AC voltage for implementation of the displacement transducer sensing scheme. Thus, in order for the electrostatic actuator to apply a DC electrostatic force only, it is necessary to bias its fixed electrodes with the control DC voltage plus the same AC voltage applied to the movable electrodes. Thus, the amplification circuit receives as input both the AC voltage and the DC voltage coming from the card. Then, the DC voltage has to be amplified by a gain of 8 as shown later on, and then be summed to the AC voltage.

Both of the input signals pass through an operational amplifier (OP-AMP) in follower configuration, which provides an output equal to the input. Then, the AC voltage is the input of an OP-AMP, working as inverter with gain 1, whereas the DC voltage generated by the data acquisition card is inverted and amplified by a gain which is the inverse of the scaling factor multiplying the control voltage computed by the controller in the feedback control VI.
In order to amplify the signal by a significant amount, high voltage OP-AMPs are considered, which work with a bias voltage of ±45V in differential mode[4]. Thus, the gain (e.g., the scaling factor in the feedback control VI) is:

$$G = \frac{\text{Max amplified voltage}}{\text{Max DAQ card voltage}} = \frac{40\text{V}}{5\text{V}} = 8 \tag{4.2}$$

Finally, both the inverted AC voltage and the inverted and amplified DC voltage are given as input to an operational amplifier, which gives as output their inverted sum, thereby being the sum of the AC voltage and the DC voltage amplified by a factor of 8.
The output of the OP-AMP circuit passes through a high resistance, before being applied to the fixed fingers of the electrostatic actuator. This is a precaution, which avoids high current flowing across the load sensor, in case of accidental collapse of the movable fingers against the fixed ones.
However, in the actual implementation of the circuit, the AC signal resulted to be dramatically attenuated. This could be related to the nature of the circuit itself (including also the device), which consists of resistors and capacitors, working as a low-pass filter, able to attenuate high frequency signals, like the present AC voltage[5]. Thus, for design convenience, it was

[4]The bias voltage of an OP-AMP determines the maximum voltage it allows as output.

[5]The frequency of the AC signal is the same as the one of the lock-in amplifier reference signal, which is 10 kHz.

decided to ignore the AC voltage, when considering the voltage to be applied to the electrostatic actuator. In fact, the amplitude of the AC voltage is small ($1V_{RMS}$) and is not able to affect the performance of the electrostatic actuator.

4.5 Trial test of the feedback control VI

In order to verify the effectiveness of the implemented VIs, a simple trial test was performed.

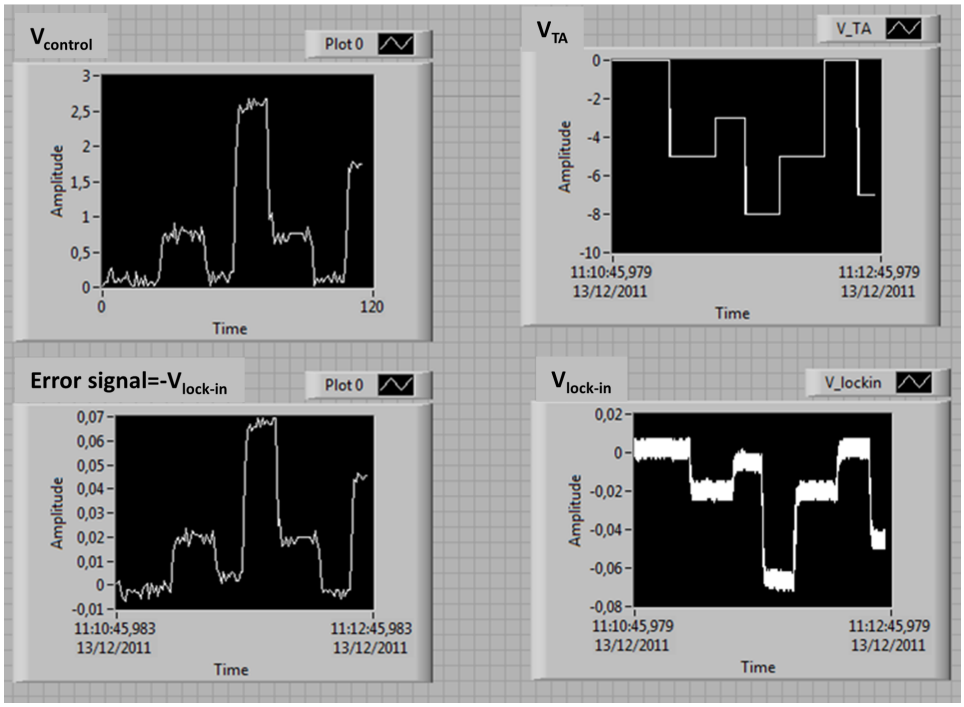

Figure 4.9: Real-time visualization of the signals monitored during a test on a sample

This involved a device with a sample mounted on it and provided with all of the connections which will be shown in more details in the next chapter. During such test, the thermal actuator was biased with a varying voltage, and the lock-in output voltage was recorded, accordingly. Furthermore, the error function (e.g., the input to the PID controller) and the voltage computed by the PID were acquired, too.

These four signals were monitored on real-time through the feedback control VI (figure 4.9). It is possible to notice that the lock-in output voltage follows the variation of the voltage applied to the thermal actuator. Thus, higher the voltage applied to the thermal actuator, higher the displacement of the load sensor and higher the capacitance variation across its two branches. Furthermore, if the lock-in output voltage increases, also the difference between it and the reference voltage (e.g., 0V) increases and, as a consequence, also the voltage generated by the PID. However, it should be noted that for simplicity in this test, only the proportional gain was set different from zero, while the integral and derivative gains were considered to be zero. For this reason, the lock-in output voltage is not zero, but follows the thermal actuator bias voltage.

Chapter 5

Electrical apparatus for interfacing the testing device with external instrumentation

5.1 Introduction

Because of the small size of the designed testing device (figure 5.1), it was necessary to develop an appropriate system of electrical connection to interface the MEMS sensitive parts to the required external instrumentation. In particular, the electrical connections to be established can be listed as:

- The two ends of the thermal actuator with an external DC power supply (figure 5.2). This latter should be able to provide a voltage on the order of 1-10 V, which corresponds to a current given by (considering

the first Ohm's law):

$$I = \frac{V}{R_{th}} \tag{5.1}$$

being R_{th} the resistance of the thermal actuator. In a first analysis, this can be computed as the double of the equivalent resistance corresponding to the inclined beams on one side (the equivalent resistance of the inclined beams on one side can be considered in series with the equivalent resistance of the inclined beams on the other side). Then, the inclined beams on one side can be considered all to be in parallel.

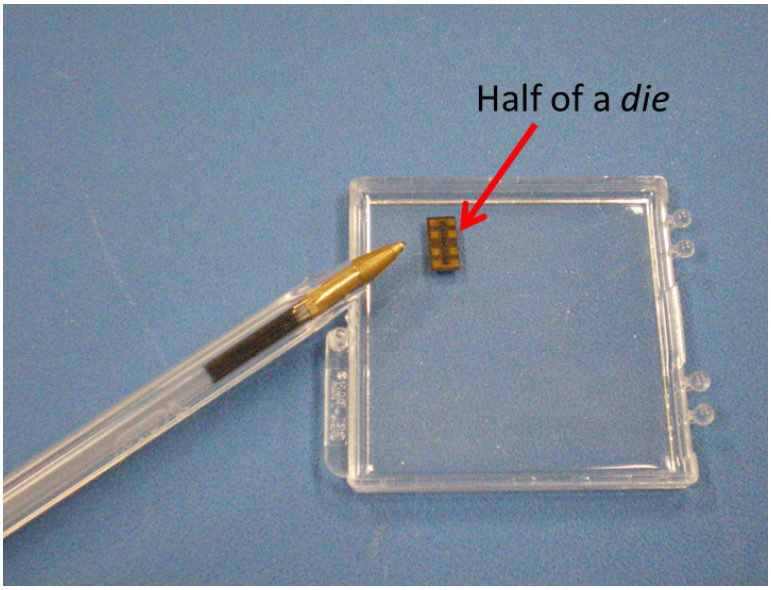

Figure 5.1: Half of a die after fabrication

Thus, the equivalent resistance is:

$$R_{eq} = \frac{R}{10} \tag{5.2}$$

where R is the resistance of one inclined beam, which can be computed

according to the second Ohm's law as:

$$R = \frac{\rho \cdot l}{A} \tag{5.3}$$

where $\rho = 1.3 \cdot 10^{-4}\Omega$m [164] is Silicon resistivity, $l = 350\mu$m is the beam length and A =8x25 μm^2 is the beam area. With these values, the total thermal actuator resistance is $R_{th} = 45\,\Omega$, providing a current on the order of tens of mAs, when the actuator is biased with 1-10 V. However, this is a reference value, while the real resistance (e.g., absorbed current) can be slightly different, since the actuator structure includes other elements than the only inclined beams considered above.

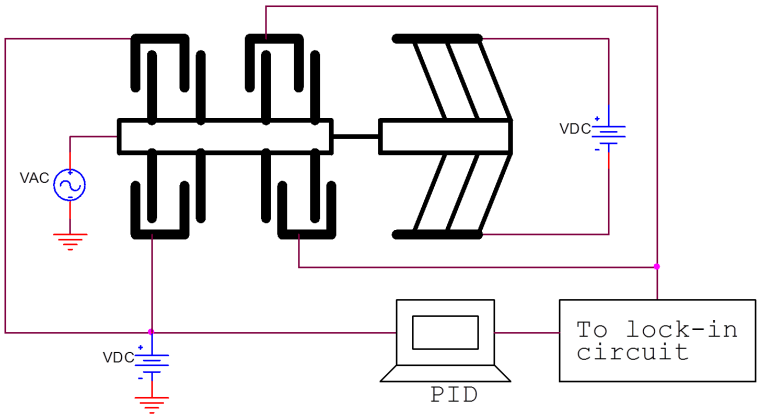

Figure 5.2: Schematic of the main connections required by the device for a correct functioning

- The two branches of the displacement sensor movable fingers and the corresponding fixed fingers with a lock-in amplifier (such connection is indicated as lock-in circuit in figure 5.2), which is able to provide an output voltage proportional to the capacitance change across the

sensor.

- The two branches of the movable fingers of the electrostatic actuator and the corresponding fixed fingers with the data acquisition card (a battery in figure 5.2), which applies to them the DC voltage computed by the controller (for sake of clarity, details about the amplification circuit which amplifies the card output are not drawn in figure 5.2).

The following sections will provide more details about the configuration of such electrical connections, which are schematically reported in figure 5.2. Furthermore, since the device can operate either in air (especially for carrying out some calibration operations) or under electron microscopes (SEM/TEM), different electrical apparatus had to be developed. However, all of them implement the same connections as in figure 5.2 and involve the same external instrumentation, which will be illustrated separately in the following sections.

5.2 Apparatus for connection of the testing device with external instrumentation

After fabrication, a certain number of dies were available for experiments, each containing either 6 or 8 devices (as shown in the previous chapter). Each die could be divided in two subdies, each containing either 3 or 5 devices, as shown in figure 5.3, which refers to subdie 1B. Each device (e. g., its sensitive parts) is connected to own pads, which are electrically isolated from the ones of the others. However, it was not possible to divide each subdie in smaller components to physically separate each device from its neighbors. Thus, during experiments a whole subdie was manipulated, even

if only one device was active.

In this work, only the device occupying the central position was considered for tests. In fact, its pads are easier to reach, since they are bigger (1.4 x 1.4 mm^2) and placed along the periphery of each die (red numbered squares in figure 5.3, and golden squares in the picture of figure 5.1).

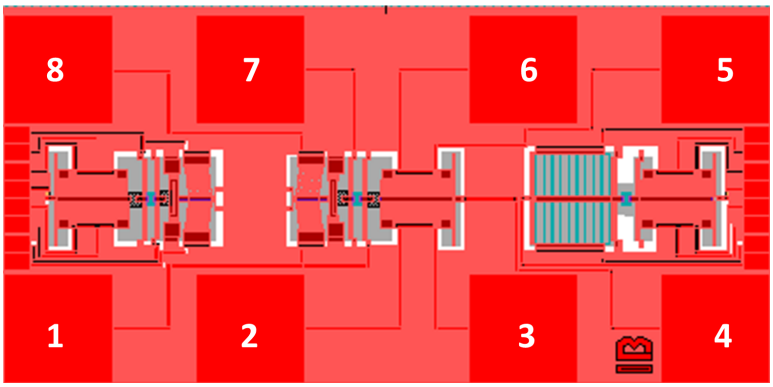

Figure 5.3: Schematic of subdie 1B

In particular, with still reference to figure 5.3, pad n.1 is connected to the sample and thermal actuator branch corresponding to the minus terminal of the power supply, pad n.2 is connected to one branch of the sensor fixed electrodes, pad n.3 is connected to one branch of the electrostatic actuator fixed electrodes, pad n.4 is connected to the sensor shuttle, pad n.5 is connected to the other branch of the electrostatic actuator fixed electrodes, pad n.6 is connected to the the other branch of the sensor fixed electrodes, pad n.7 is connected to the other side of the sample, and, finally, pad n.8 is connected to the other branch of the thermal actuator.

The whole subdie (containing the device of interest in central position) was accommodated inside a small groove on a metallic board (figure 5.4a), and fixed there by the means of appropriate SEM clips, each being in contact

with one of its eight square pads.

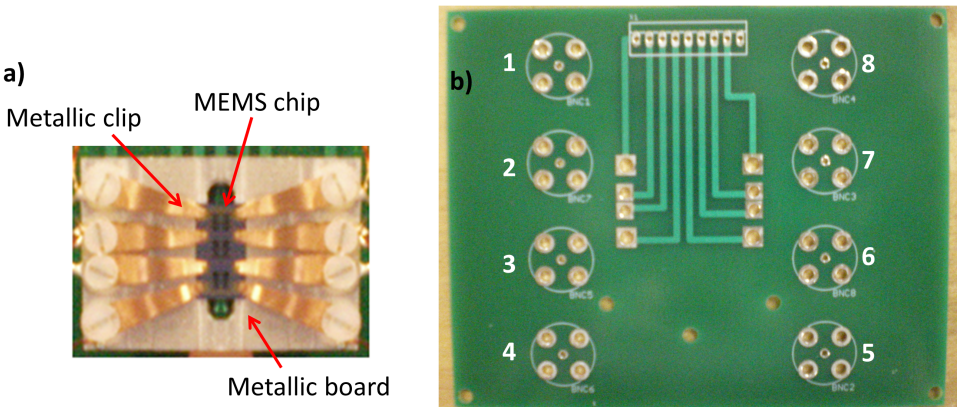

Figure 5.4: (a) Metallic board with a groove spanning in the midst for accommodation of a subdie, and (b) the printed circuit board (PCB) designed for accommodation of the metallic board

In order to easily connect the clips with other instruments, the metallic board is fixed on a custom-designed printed circuit board (PCB) (figure 5.4b) through plastic screws and nuts for isolating the clips from the board. Furthermore, this latter is provided with eight BNC sockets, each being welded to a small header in the middle. Each header is then connected to the corresponding SEM clip through a little copper wire. On the same PCB there is on top a series of small sockets with welded pins, each connected to one of the BNC socket, and thus to one of the clips. These are then used to provide connection in the arrangement for SEM measurements, as shown later. Under the MEMS metallic board, there is another metallic platform mounted on the PCB, which was used as sample holder (figure 5.5). The copper tape visible on the PCB is a sort of conductive path which helps imaging of the sample under SEM, when it is picked up and brought from

the sample holder to its final position on the chip. Finally, it is worth to notice that the MEMS metallic holder is fixed to the PCB by the same screws, which fix the clips on the MEMS pads (5.5).

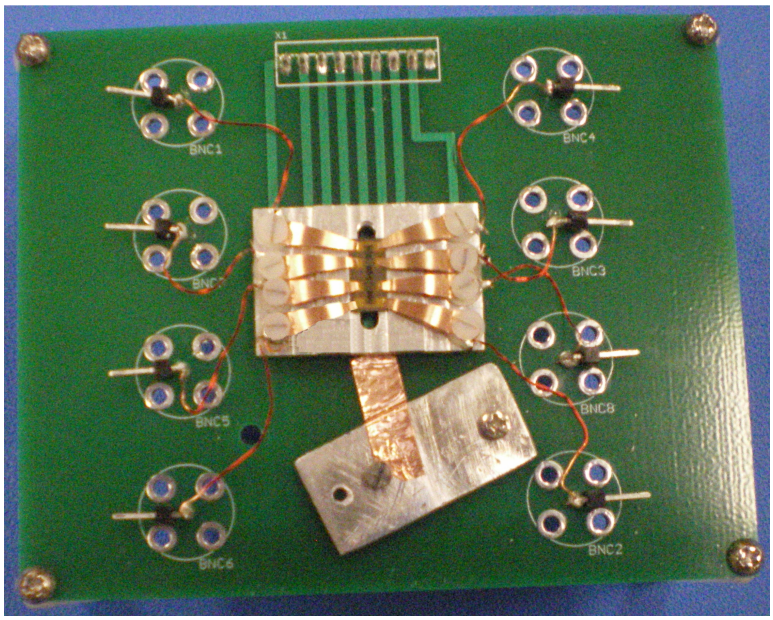

Figure 5.5: The PCB with the MEMS holder fixed on top

5.2.1 Arrangement for measurements in air

Some preliminary tests on the designed device were performed in air. Thus, all the electrical connections previously described had to be arranged for this application. In particular, the experimental set-up to be used included a Faraday cage to shield the MEMS in addition to the complete PCB previously described (figure 5.6).

The Faraday cage was provided with BNC connectors, each welded to one terminal on the PCB corresponding to one clip (pad) on the MEMS board.

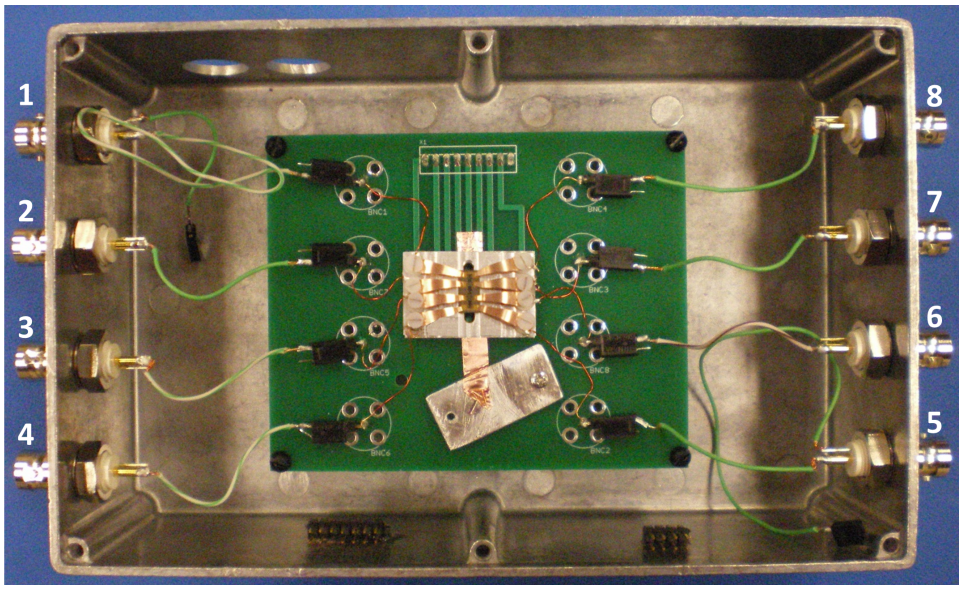

Figure 5.6: Faraday cage to shield the MEMS for measurements in air

More specifically, as shown in figure 5.6:

- Connector 1 refers to one side of the sample and the branch of the thermal actuator, being connected to the minus terminal of the power supply;
- Connector 2 refers to one branch of the sensor fixed fingers;
- Connector 3 refers to one branch of the electrostatic actuator fixed electrodes;
- Connector 4 refers to the sensor shuttle;
- Connector 5 refers to the other branch of the electrostatic actuator fixed electrodes;
- Connector 6 refers to the other branch of the sensor fixed fingers;

- Connector 7 refers to the other sample side;
- Connector 8 refers to the other thermal actuator side.

Each instrument was then connected through BNC cables to the proper BNC connector on the Faraday cage.

5.2.2 Arrangement for *in situ* SEM testing

Because of the relative small size of the SEM chamber, the arrangement used for measurements in air was not suitable for SEM application, and however the metallic shield was not necessary, since the SEM chamber is already a kind of Faraday cage. Thus, it was necessary to develop a different setup. This included the PCB and metallic MEMS holder, as before. Then, in addition, a proper connector was assembled, consisting of eight thin cables, each ending (on one side) with a small header enclosed within a plastic cover, provided with perforations in correspondence of them. Such component was fixed on the uppermost part of the PCB in correspondence of the series of little metallic pins, in order to establish a contact between each little cable and the corresponding pin on the PCB, which is on turn connected to one of the clips (figure 5.7). The other end of the cables were enclosed within a ceramic cylindrical element, which was screwed to one side of the connector shown in figure 5.7. The other side was instead provided with a board with BNC connectors, and each of them resulted to be connected to a proper pad on the MEMS chip, through the thin cables and pins, previously described. Such connector was compatible with one of the flanges placed on the SEM chamber. Thus, it was screwed inside a proper opening on the SEM, such that the connector with the thin cables (figure 5.7) remained inside the chamber, while the BNC connectors remained outside, in order

to provide connection with the proper external instrument. In particular, such connectors were assembled with the following correspondence:

- Connector 1 refers to one branch of the sensor fixed fingers;
- Connector 2 refers to the sensor shuttle;

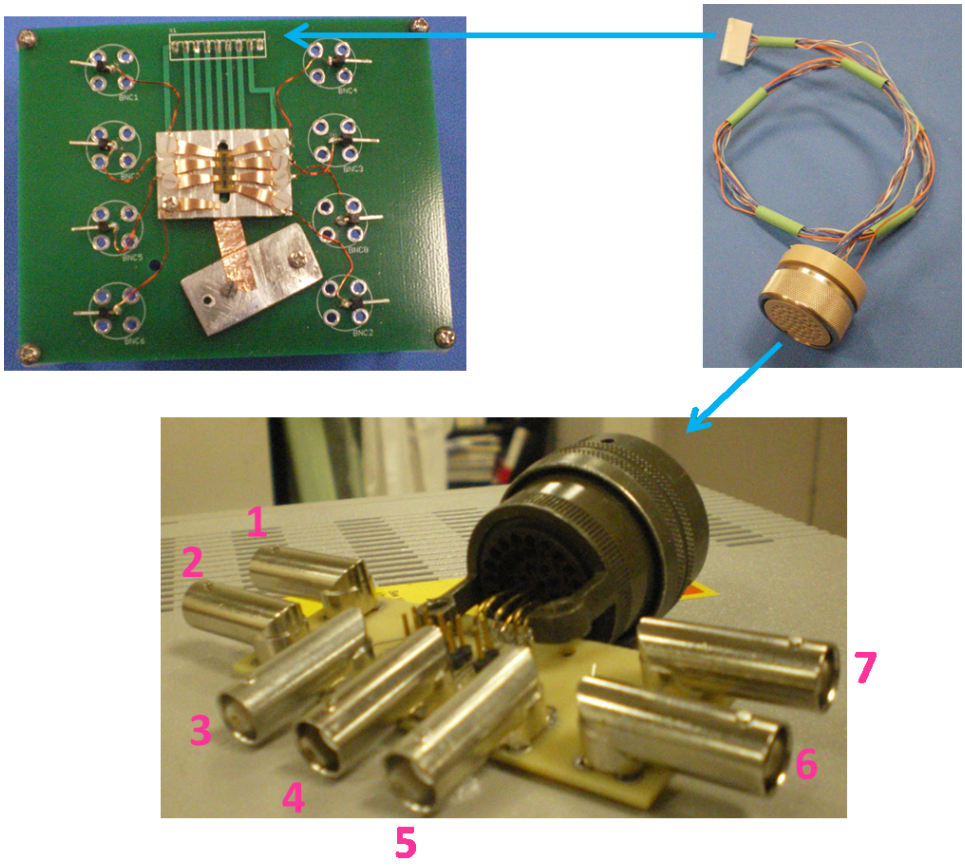

Figure 5.7: Arrangement for *in situ* SEM testing

- Connector 3 refers to the other branch of the sensor fixed fingers;

- The shield and the internal signal of terminal 4 were connected each to either end of the thermal actuator, in order for the branch connected to one side of the sample to be on the shield (e. g., which was connected to the minus terminal of the power supply);
- Connector 5 is connected to the other side of the sample;
- Connector 6 refers to one branch of the electrostatic actuator fixed fingers;
- Connector 7 refers to the other branch of the electrostatic actuator fixed fingers. It is shorted to connector 6 by a copper wire welded at the bottom of the board.

The PCB holding the MEMS chip was placed inside the SEM by the means of a metallic stub, screwed at its bottom, which was able to fit a proper opening on the sample holder, protruding from the base of the SEM chamber.

5.2.3 Arrangement for *in situ* TEM testing

The SEM setup was not compatible with TEM, because their chambers differ for some key features (e.g., this latter is much smaller and has flanges of different size to guarantee connection between external elements and the sample which is inside). Thus, also for this application, a proper setup was assembled (figure 5.8a). In this case, the chip was accommodated (up side down and then fixed with removable little clips) inside a proper groove (figure 5.8b) placed at one end of a cylindrical arm, which can fit the TEM chamber. At the bottom of the MEMS cavity (figure 5.8b), there are eight small golden pins, each being in contact with one pad. These small pins are connected to wires running all along the arm, each ending with one long rigid

connector. Such connectors were then screwed inside appropriate sockets, welded on a custom-made printed circuit. Each socket was then wired to an SMC plug, and an SMC-BNC coaxial cable was used to connect each plug (e.g., pad on the MEMS chip) to the corresponding instrument (figure 5.8a).

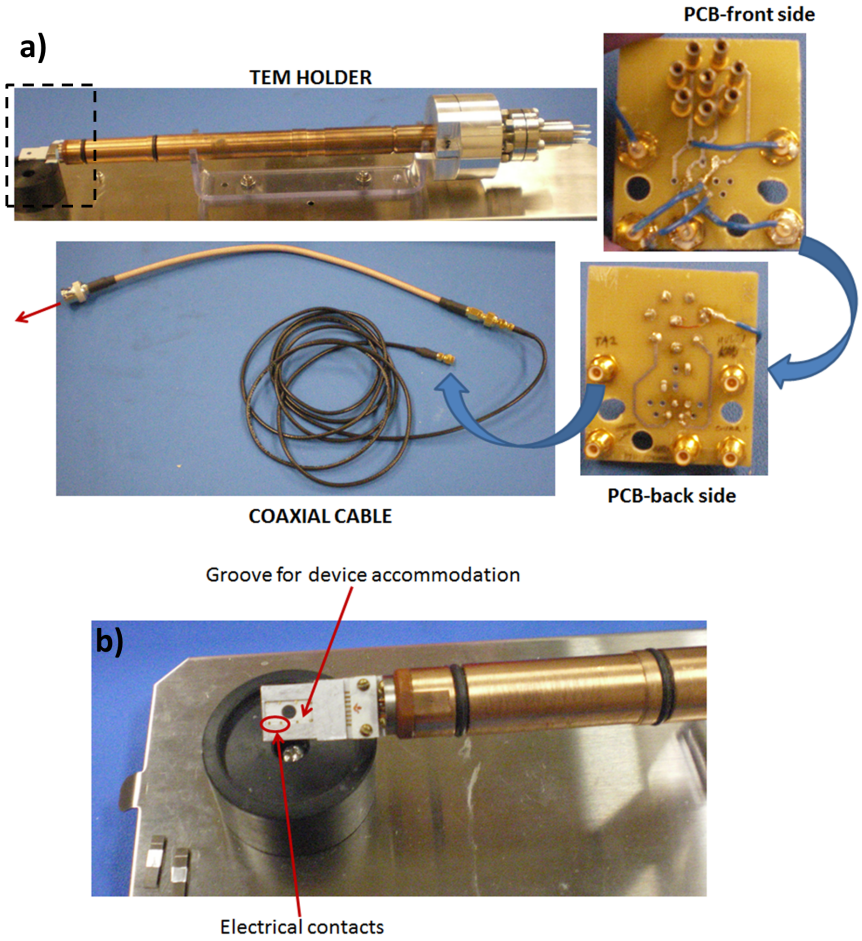

Figure 5.8: a) Setup for *in situ* TEM experiments, including a TEM holder ending with a cavity accommodating the MEMS chip detailed in b)

5.3 External instrumentation

All of the arrangements previously shown provide electrical access to all the MEMS sensitive features.

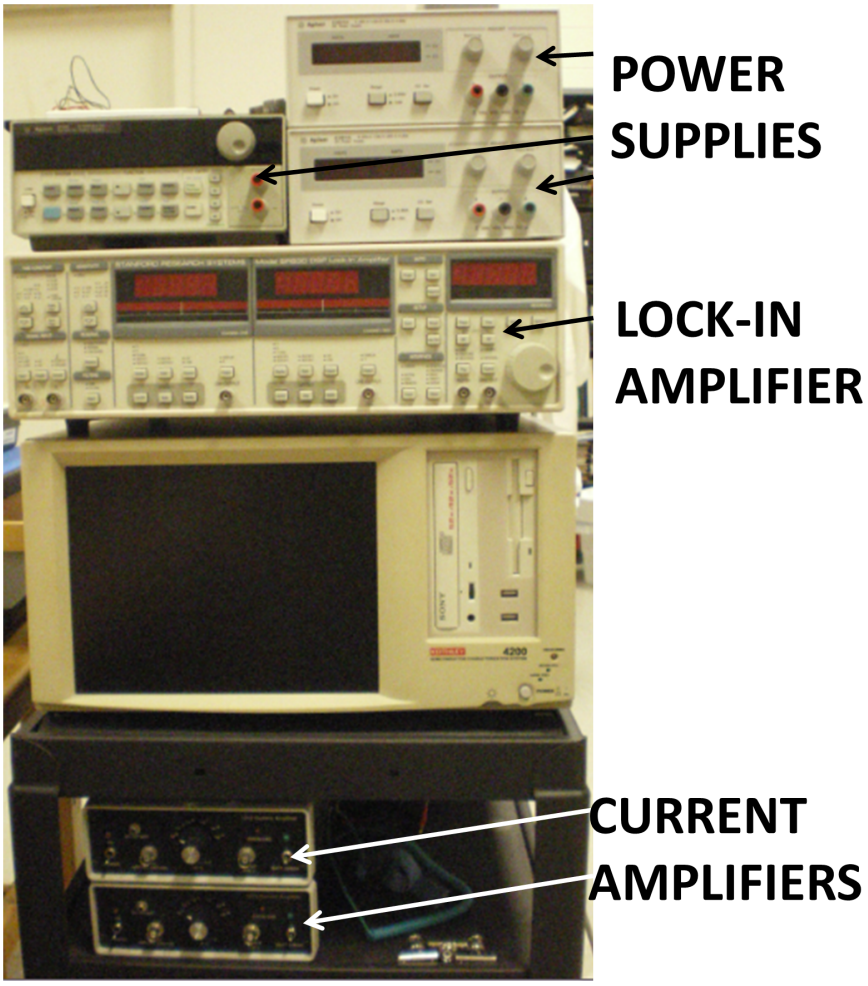

Figure 5.9: External instrumentation to be interfaced with the MEMS chip

For a correct functioning, these had to be interfaced to proper external instrumentation. In particular, this included (figure 5.9):

- One DC power supply, which allowed a fine increase of the generated voltage, which was used to bias the thermal actuator;
- Two current-pre-amplifiers and a lock-in amplifier, which was used to receive the voltage signals coming from the two branches of the displacement sensor (the lock-in amplifier was also used to apply the AC voltage needed by the sensing scheme, which will be shown in the next subsection);
- A personal computer for implementation of the controller routine;
- A data acquisition (DAQ) card to generate the control voltage computed by the controller routine, and to record the voltage applied to the thermal actuator and the lock-in amplifier output voltage;
- An amplification circuit to amplify the control voltage generated by the DAQ card;
- Two DC power supplies able to generate high voltage (40V) for biasing the amplification circuit.

In the following subsection, more details will be provided to the electrical circuit implementing the sensing scheme of the displacement sensor.

5.3.1 The lock-in amplifier

Different electrical circuits could be considered for providing a voltage signal proportional to the capacitance change of a capacitive displacement transducer. However, in this work, a scheme including a lock-in amplifier was adopted, since it had been proven to provide much higher sensitivity than other configurations [165].

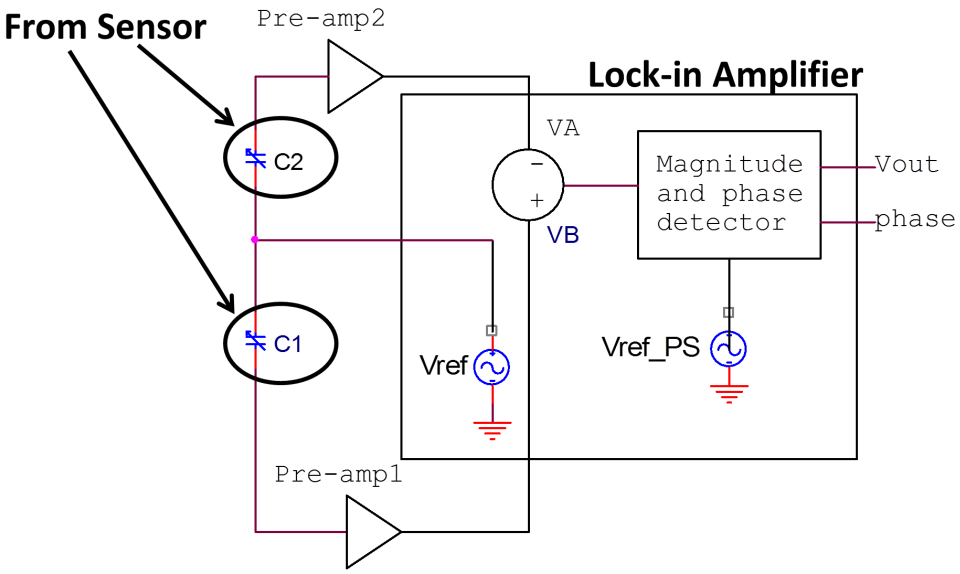

Figure 5.10: Electrical scheme for detection of the capacitance variation occurring across the displacement sensor when a displacement is applied

For the purpose of the present design, the lock-in amplifier had to work in differential mode, since it had to perform a subtraction between the signals coming from either branch of the displacement sensor. However, for proper functioning, it received each of the signals of interest after these had been amplified by current pre-amplifiers, as shown in figure 5.10, which illustrates the complete electrical scheme for reading the sensor capacitance variation. According to such scheme, the output voltage is proportional to the capacitance change according to the following equation (5.4):

$$\mathrm{V_{lock}} = G \cdot 2\pi f_{ref} \frac{V}{\sqrt{2}} \Delta C \tag{5.4}$$

In the above, G is the gain of the current pre-amplifiers carrying the signals to the lock-in amplifier, $\Delta C = C_2 - C_1$ is the capacitance variation between

the sensor branches, which has to be measured, $\sqrt{2}$ is introduced because the output signal is displayed as RMS, V_0 and f_{ref} are the amplitude and the frequency of the reference AC signal of the lock-in amplifier, respectively. The lock-in amplifier receives as input two signals, V_A and V_B from the current pre-amplifiers, each connected to one branch of the load sensor. Such voltages are:

$$V_A = -GC_1 \frac{dV_{ref}}{dt} \tag{5.5}$$

and

$$V_B = -GC_2 \frac{dV_{ref}}{dt} \tag{5.6}$$

Thus, the input signal to the lock-in amplifier is:

$$V_{in}(t) = -G\Delta C \frac{dV_{ref}}{dt} = G\Delta C\, V_0 \omega_{ref} \sin(\omega_{ref} t) \tag{5.7}$$

being $V_{ref} = V_0 \cos(\omega_{ref} t)$ the reference voltage of the lock-in amplifier. The output signal is multiplied by a reference signal (V_{ref_PS}), and then filtered in order to obtain equation (5.4).

5.4 The complete electrical scheme

As a summary, it is useful to show in one scheme the complete electrical circuit which was adopted during the tests, including the MEMS chip and all the external instrumentation (figure 5.11).

In this figure, the main elements to be properly connected are the MEMS block (where indicated its terminals: TA for thermal actuator, LS for displacement sensor, FD for electrostatic actuator, SH for shuttle, and GND for ground), the lock-in amplifier, the two current preamplifiers, which are drawn as triangles, the data acquisition (DAQ) card (where indicated its terminals: ai0 for acquisition of the voltage applied manually to the thermal

actuator, GND for ground, ai1 for acquisition of the output voltage from the lock-in amplifier, and ao1 for the output voltage to be applied to the electrostatic actuator), the amplification circuit (OP-AMP block, where indicated its terminals: OUT for the amplified voltage, which is the output of the circuit, V+ and V- for the terminal where applying the bias voltage to guarantee a correct functioning of the circuit, IN for the input voltage signal to be amplified, and GND for ground), the fine power supply to bias the thermal actuator with a voltage increased manually by the operator during a test, and the two coarse power supplies needed to bias the amplification circuit.

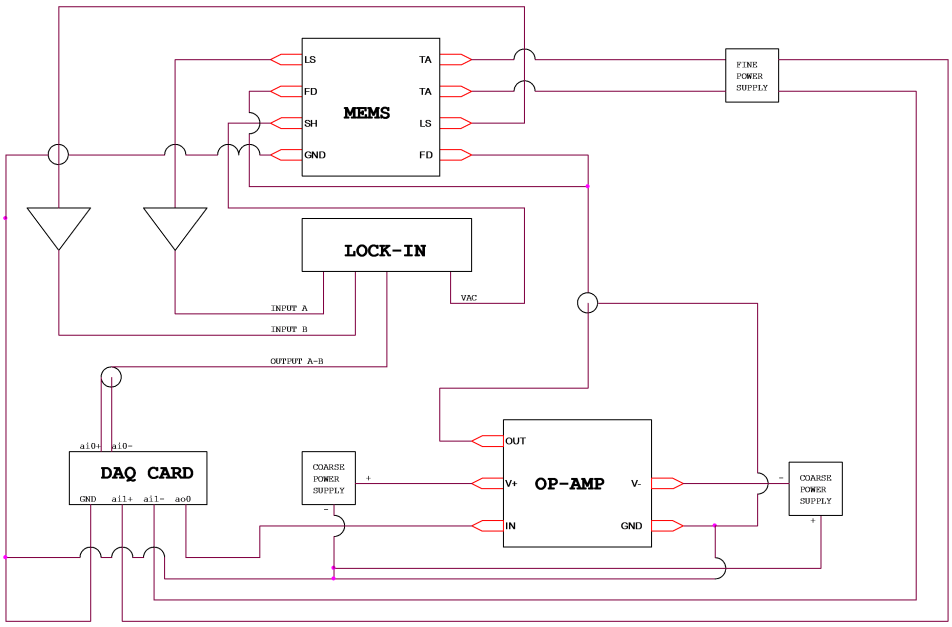

Figure 5.11: Complete electrical scheme implemented to perform tests with the present experimental apparatus, showing connections between the device (MEMS) and all the required external instrumentation

The personal computer which run the routine implementing the feedback control was not drawn in the figure, in order to simplify the representation of the scheme. However, for completeness it should be placed near the DAQ card block, receiving from it the lock-in output voltage and providing as output the information about the voltage the card has to generate.
A critical element, which can affect the correct functioning of an electrical circuit, is the choice of the ground signal. In this case the circuit ground was considered as the reference potential of the input signal to the preamplifiers (which is the same as the reference voltage of lock-in input and output signals). Also the MEMS substrate (indicated as GND terminal of MEMS block) was connected to the circuit ground in order to avoid flowing of eddy current.

5.5 Procedures for testing the device

The tensile tests performed with the experimental apparatus presented above were conducted under displacement control. In particular, the operator increased manually the voltage to bias the thermal actuator with, and at each step a picture of the sample was recorded, in order to derive its deformation after image processing. The corresponding load was instead extracted from the voltage computed by the controller in order to keep the displacement sensor at equilibrium.
The aim of the test is to obtain a stress-strain curve for the material sample. However, such information had to be extracted from the available data, which included the voltage applied to the thermal actuator, the output voltage from the lock-in amplifier, and the control voltage. In order to properly use such data, it was necessary to know the real behavior of both the actu-

ating and sensing parts of the device, as compared to design expectations. In particular, three kinds of test were performed in order to characterize the device, before considering it for tests on samples:

- Thermal actuator. A relationship was determined to relate the bias voltage to the corresponding displacement which is delivered. In particular, the experimental data were compared to those obtained from a numerical analysis, as shown in chapter 3;
- Electrostatic actuator. A relationship was determined between the bias voltage and the corresponding delivered displacement. The experimental data were compared in this case to the results obtained from an analytical model. In particular, the relationship determined herein was used later for characterization of the displacement sensor;
- Displacement sensor. The sensor was tested in order to find a calibration curve relating the displacement to the corresponding capacitance change.

The tests for characterization of both the actuators and sensor were conducted under the SEM with no sample mounted.

5.5.1 Testing of the thermal actuator

Performance of the thermal actuator was evaluated on the basis of the displacement at the bottom (e.g., the region where samples are usually attached) generated by a bias voltage varied in the range 0-7V, with steps, each corresponding to an absorbed current of 4 mA. Such test was conducted under SEM, with no sample, in order to reproduce the same operating con-

ditions, then available during tests with a sample[1]. In order to characterize the thermal actuator, this was biased with a DC voltage, while keeping grounded all the other structures (e.g., electrostatic actuator and displacement sensor) (figure 5.12a).

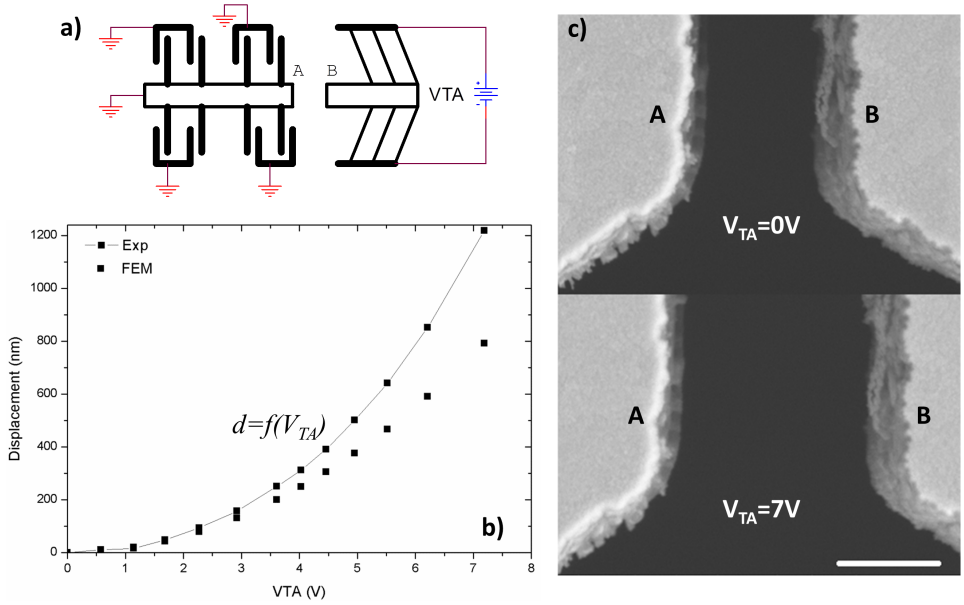

Figure 5.12: Thermal actuator: a) Electrical circuit for testing of the thermal actuator; b) Comparison between experimental and numerical data; c) Two pictures of the device taken when biasing the thermal actuator with different voltages (scale bar: 2μm)

At each step, a picture of the gap between the thermal actuator and the displacement sensor (segment AB in figure 5.12c) was recorded, and later processed for determining the displacement of the thermal actuator bottom

[1]In air, there is much more heat dissipation then in vacuum. Thus, the displacement generated by the same bias voltage is smaller in air than in SEM

region. In particular, to this aim a MATLAB scrip implementing a cross-correlation algorithm was considered. It was a custom-made routine which allowed derivation of the displacement of a selected region in a picture with respect to the same region in a reference picture. In this case, the reference picture was the picture taken at the beginning of the test for a bias voltage of 0V.

Figure 5.12b shows a comparison between the experimental data and those obtained in chapter 3 from numerical analyses, carried out with Comsol Multiphysics.

Experimental data were then fitted by a power function of the third order, thus providing an expression (which is a calibration curve) for relating the displacement delivered at the bottom region (e.g., the region at the interface with samples) to the bias voltage, which was useful during a test on a sample, for evaluating the thermal actuator expected displacement even for voltages not considered during this calibration procedure.

There is a good agreement between experimental and numerical results for a bias voltage below 2V. Then, the two sets of data diverge up to a difference of 35% for 7V, corresponding to a displacement of about 800 nm (which was the maximum voltage considered during tests on samples).

The difference between experimental and numerical data could be related to the geometry of the actuator, which could vary from design because of fabrication tolerances. However, since the main difference is for higher voltages, thus higher operation temperature, this could be related to the physical parameters considered in the analysis, which were modeled to not vary with temperature.

Finally, it is worth to notice that performances of the thermal actuator varied slightly from one chip to another. Thus, it was preferred to repeat the

testing procedure showed above each time a new MEMS was considered for experiments.

5.5.2 Testing of the electrostatic actuator

The electrostatic actuator was tested in order to derive a relationship between the bias voltage and the corresponding displacement, which was then used to characterize the displacement sensor, as shown in the following section. In order to derive such relationship, a DC voltage was applied between the fixed and moving electrodes of the actuator, while keeping grounded all the other structures (figure 5.13a). This test was conducted with no sample mounted. Thus, at each step a picture of the gap between the thermal actuator (which was fixed, being not biased) and the displacement sensor shuttle was recorded. The sequence of pictures taken during the test was then compared with the initial reference picture in order to get the displacement at each step. Such information was extrapolated by using the same MATLAB script used to analyze the thermal actuator, as previously shown.
At each step, the actuator reached an equilibrium position, thus requiring the sum of the forces acting on it to be zero. In absence of sample, as in this case, the actuator is subject to an electrostatic force, due to the bias voltage, and to an elastic force, exerted by the supporting springs, which act against the movement. The electrostatic force is:

$$F_{LSA} = \frac{1}{2} N \epsilon_0 \frac{AV^2}{(d_0 - y)^2} \tag{5.8}$$

being N the number of electrodes, ϵ_0 the vacuum permittivity, A the transversal area of one electrode, V the bias voltage, y the displacement, and d_0 the nominal distance between a pair of movable and fixed fingers, while the

elastic force is instead:

$$F_{elastic} = k \cdot x \tag{5.9}$$

where k is the elastic constants, characterizing such beams.

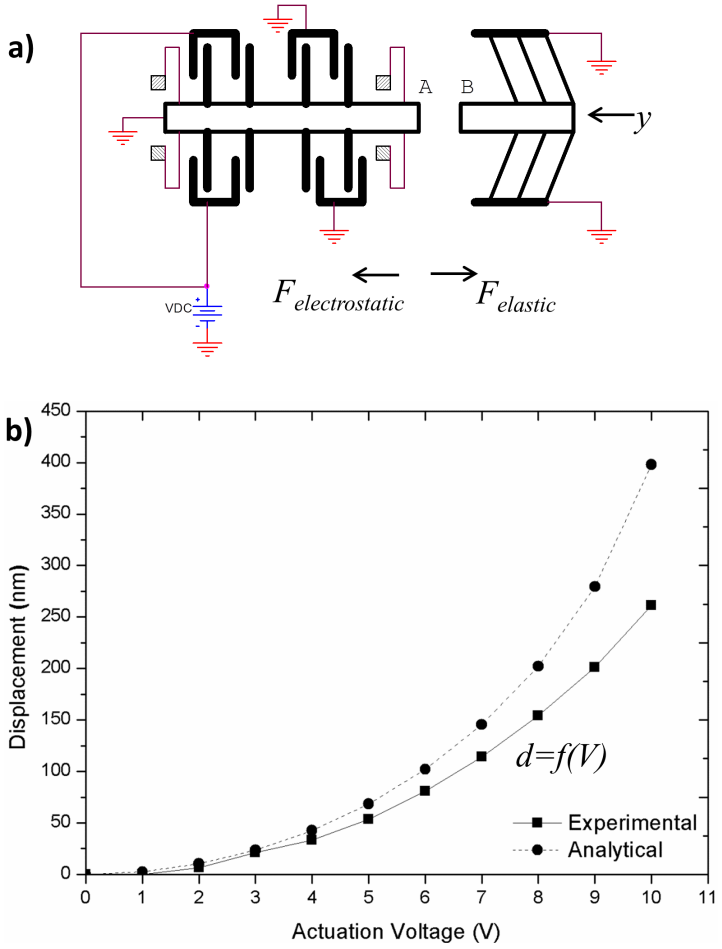

Figure 5.13: Electrostatic actuator: a) Electrical circuit implemented during the test; b) comparison between experimental and analytical data

Equilibrium condition requires that:

$$k \cdot x = \frac{1}{2} N \epsilon_0 \frac{AV^2}{d_0^2} \tag{5.10}$$

By solving this non-linear equation, the displacement corresponding to each value of the bias voltage could be determined analytically.

Figure 5.13b provides a comparison between the displacement (evaluated in correspondence of segment AB in figure 5.13a, which is the device gap) generated by the electrostatic actuator as a function of the bias voltage. Especially for higher voltages, the two curves diverge (with a difference up to 50%), providing the analytical curve an overestimation of the generated displacement.

This can be easily explained because of fabrication tolerances, which cause the gap between a couple of fixed and moving electrodes not to be equal the design value, but around 25% more. As can be inferred from equation 5.8, the displacement scales with one over the gap square, thus significantly affecting the actuator performance. Then, also other parameters, like the length, the width, and the thickness of the electrodes play a role in determining the delivered electrostatic force (e. g., displacement), and a difference between the design and real geometry after fabrication can further explain the difference between the two curves in figure 5.13b.

Furthermore, by fitting the experimental data with a polynomial curve (of the second order), a calibration curve for the actuator can be inferred, and this was used for characterization of the displacement sensor, as shown next.

It is worth to notice that the bias voltages considered during testing of the electrostatic actuator were in the range 0-10V, even if higher voltages where then used during tests with a sample. It was not possible to go beyond such value in this case, since when there is no sample mounted, the maximum

voltage which can be applied is limited by the phenomenon of pull-in. In particular, in systems which can be modeled as a capacitor in series with a spring, equilibrium requires the forces acting on the system to be equal to zero. However, when the capacitor is biased with a voltage higher that a critical voltage (pull-in voltage), the elastic force cannot longer balance the elastic force. Thus, the two plates of the capacitor collapse[2]. The pull-in voltage can be computed as [150]:

$$V_{pull-in} = \sqrt{\frac{k\, d_0^3}{2\, \epsilon\, A}} \tag{5.11}$$

where k is the stiffness of the spring supporting one plate of the capacitor, d_0 the initial gap between the capacitor electrodes, ϵ is air permittivity, and A the electrodes transversal area. If in this equation, the parameters of the electrostatic actuator are substituted, it results that $V_{pull-in} = 14$ V. However, considering fabrication tolerances which can affect the real geometry of the actuator, it was preferred to not go beyond 10V as a safety voltage. Finally, unlike the test for characterization of the thermal actuator, this test on the electrostatic actuator could be conducted either in air or under SEM, since it behaves in the same way in both conditions. However, in order to exploit the high displacement resolution of SEM pictures, this test was performed under SEM, too.

5.5.3 Testing of the displacement sensor

For testing the displacement sensor it was necessary to displace the electrocapacitive unit and record the corresponding capacitance variation. The

[2]Such phenomenon was already recalled in chapter 1, when discussing characterization of micro-components by the M-test

capacitive unit was moved through its electrostatic actuator, being biased with a DC voltage, while keeping grounded the thermal actuator, and being the sensor electrodes connected to a lock-in amplifier, according to the sensing scheme previously shown, and synthetically reported in figure 5.14.

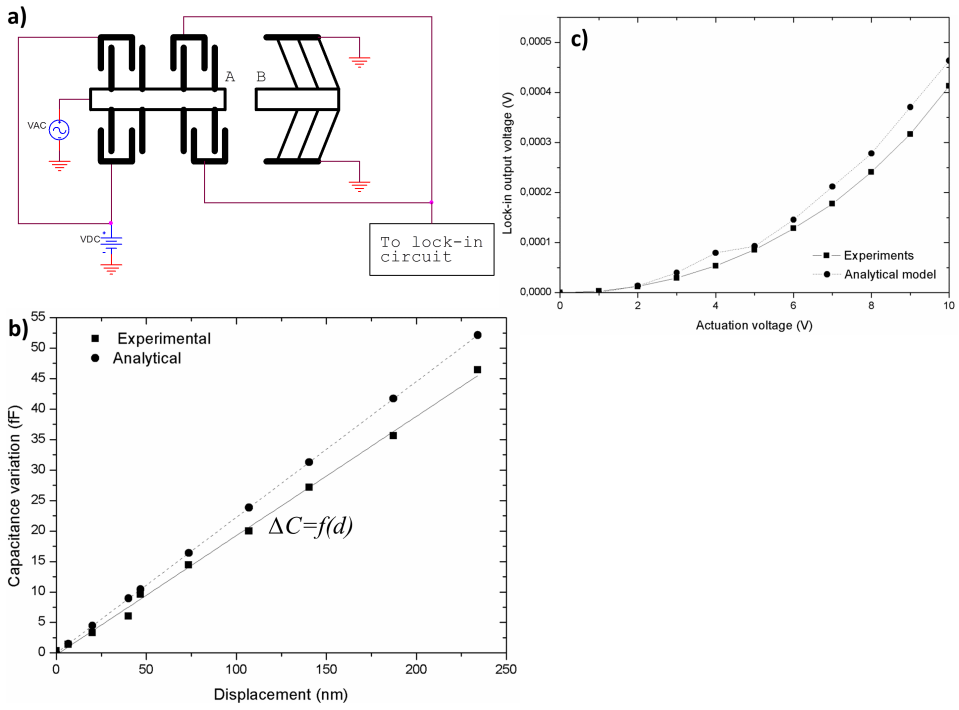

Figure 5.14: Displacement sensor: a) Electrical circuit for testing of the displacement sensor; b) Comparison between the capacitance change-displacement relationship determined both analytically and experimentally; c) The lock-in amplifier output voltage as a function of the voltage biasing the electrostatic actuator. Experimental results are compared to the analytical ones

At each actuation step, a picture of the device gap (segment AB in figure

5.14a) was recorded and then compared to the reference picture taken at the beginning of the test. Such comparison was performed by a cross-correlation MATLAB script, as already mentioned in the previous subsections. Furthermore, at each step, also the lock-in output voltage was recorded, too. In particular, from the previous sections, it is known that such output voltage is related to the capacitance variation as:

$$V_{lock} = 2\pi f_{ref} V_0 \, G \, \Delta C \tag{5.12}$$

from which it follows that:

$$\Delta C = \frac{V_{lock}}{2\pi f_{ref} V_0 \, G} \tag{5.13}$$

being G the gain of the current pre-amplifiers, f_{ref} and V_0 the frequency and the amplitude of the lock-in AC reference voltage, respectively. In the case of the present experiments, such parameters were set as:

$G = 10^4$
f_{ref} =10 kHz
$V_0 = \sqrt{2}$ V

Furthermore, in chapter 3, it was shown that for small displacement:

$$\Delta C = 2N\epsilon_0 A \frac{y}{d^2} \tag{5.14}$$

being N the number of comb-drive fingers on one side, A their transversal area, ϵ_0 the air permittivity, and d the initial gap between a fixed and a moving electrode. The displacement delivered to the sensor was determined from the calibration curve of the electrostatic actuator previously derived, in order to obtain from the previous equations two analytical relationships,

each relating either the lock-in output voltage or the capacitance change to the displacement, respectively.
The experimental data were then compared to the analytical results, as shown in figure 5.14b-c.

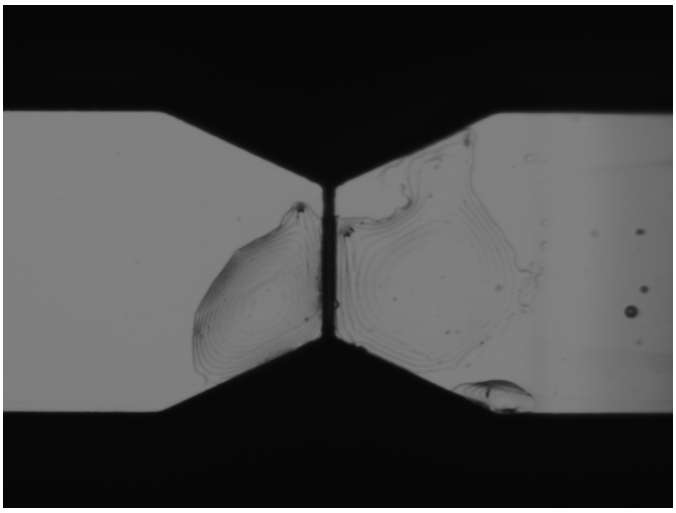

Figure 5.15: Optical microscope picture of the epoxy drop deposited to bridge the displacement sensor and the thermal actuator

From this it is possible to notice that the experimental curves matched well the analytical ones, with a maximum error of less than 20%. Then, from data fitting, it is possible to derive a linear expression for relating the capacitance change to the displacement, which was later used in tests with samples.
The same characteristic relationship capacitance change-displacement was obtained with another testing configuration, considered for comparison. In this second case, the sensor shuttle was moved through the thermal actuator, while bridging the gap in between. In particular, a droplet of epoxy was deposited through a manipulator in correspondence of the gap, in order to cover it (figure 5.15). Because of the high stiffness of the thermal actuator

body, it was then reasonable to consider that the displacement sensor moved by the same amount as the thermal actuator bottom region, when it was free during calibration.

Chapter 6

Application of the device for *in situ* SEM tensile testing of nanostructures

6.1 Procedures for *in situ* SEM tensile testing of nanostructures with the developed MEMS device

The MEMS device described in details in the previous chapters allows for *in situ* SEM/TEM[1] tensile testing of nanostructures. In particular, this is suitable for testing especially of one-dimensional nanostructures, like nanotubes and nanowires, but also two-dimensional nanostructures, like thin films, can be tested if their size is compatible with that of the device.

[1]The structure of the experimental setup for TEM measurements was shown in the previous chapter, but its application was not reported herein.

The displacements which can be generated on the sample can be above 1 μm, while the gage length[2] is 2-4 μm, and the maximum load[3] which can be considered is 100μN. The strain rate is usually on the order of $6 \cdot 10^{-4}$ (as in other uniaxial tests performed on micro/nanosamples [178]-[179]), which is limited by the time response of the PID controller[4]. The tests are conducted at room temperature under displacement control with a uniaxial tensile load, which can be manually increased. Thus, all of the mechanical properties which can be derived from tensile tests can be derived on using the present device, too. In particular, typical mechanical properties of interest are the Young modulus, the yield and ultimate stress, and the fracture strain.

Before performing tests on a sample, a number of preliminary tests have to be conducted. In particular, there are some of these tests which have to be always repeated when considering a new sample (like the sample preparation and tuning of the PID controller). Then, other procedures, like the calibration of the device actuators and sensor, have to performed once for the same device.

6.1.1 Tests for device calibration

Before considering the device for tests on samples, it is necessary to perform some preliminary tests on the thermal actuator, the electrostatic actuator, and the displacement sensor, in order to derive their calibration curves. In particular, the calibration curve of the thermal actuator defines a relation-

[2]This can be slightly larger than the gap between the thermal actuator and the electrocapacitive unit, depending on how the sample is fixed on the device.

[3]This value could be further extended by assembling an amplification circuit with higher gain.

[4]Faster the PID controller time response, higher the achievable strain rate.

ship between its bias voltage and the corresponding delivered displacement, the calibration curve of the electrostatic actuator defines a relationship between its bias voltage and the corresponding generated displacement, which is then necessary to find the calibration curve of the sensor, which provides a relationship between the displacement and the magnitude of the lock-in amplifier output voltage. All of these operations can be performed according to the procedures shown in the previous chapter.

6.1.2 Sample preparation

First of all, a sample with characteristics compatible with the device features listed above should be chosen for a test. Then, it has to be properly prepared in order to be placed onto the device.

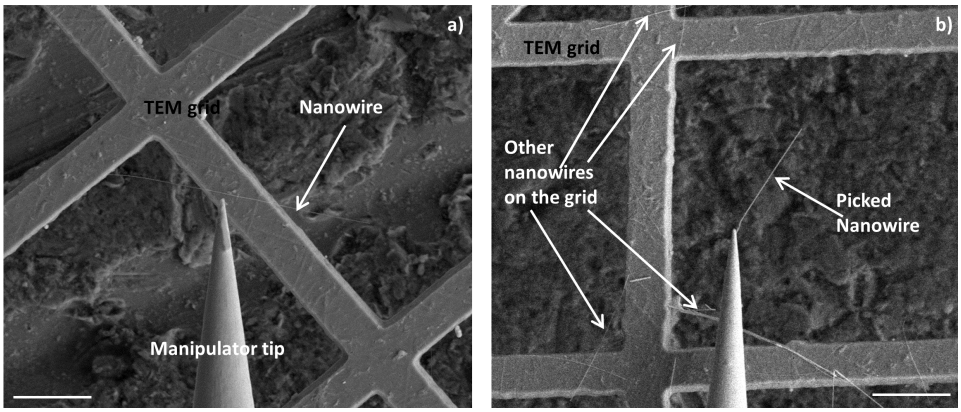

Figure 6.1: a) The micromanipulator tip approaching a nanowire on a TEM grid, and after picking it up (b) (scale bar: 10 μm)

In particular, the sample of interest should lie on a suitable support which can be fixed (for example through copper tape) to the metallic sample holder screwed to the printed circuit board, where also the MEMS sup-

port is screwed[5]. In fact, sample mounting has to be carried out under SEM, since high magnification is required.

In order to provide more details, it is useful to consider a practical case, where the sample is a nanowire. For simplicity, it is convenient to have availability of a wide number of similar nanowires of the material under investigation, dispersed on a TEM grid. Then, a nanowire suitable for testing can be chosen among all the available ones. This should have the desired physical dimension and should be properly positioned on the grid in order to be easily picked up with the help of a manipulator tip (compatible with the SEM chamber).

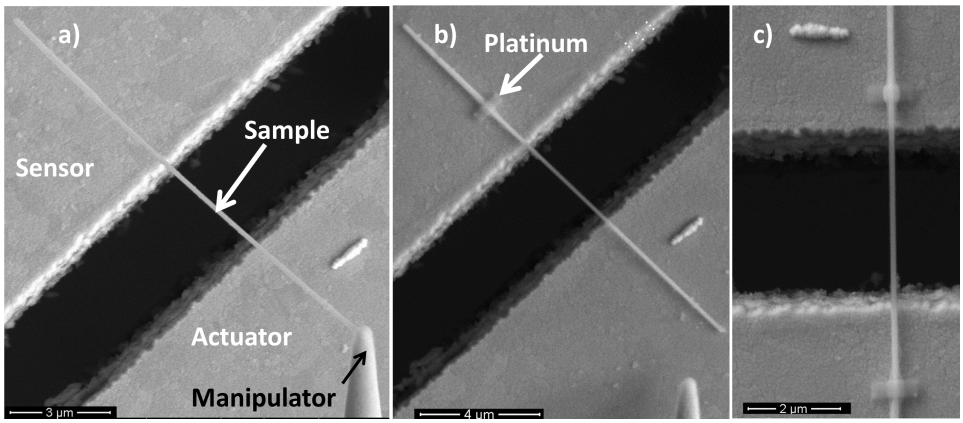

Figure 6.2: Steps for mounting of a sample onto the device: a) The manipulator tip is brought close to the device in order for the nanowire to fall down on it; b)-c) Fixing of the nanowire by the means of e-beam deposition of Platinum

In particular, the micromanipulator tip approaches the nanowire of interest.

[5]This was described in details in the previous chapter during the presentation of the SEM experimental setup.

If the electrostatic force between the tip and the nanowire is higher than the adhesion force between the nanowire and the grid, as usual, the nanowire jumps on the manipulator tip (figure 6.1).

At this step, it is convenient to take a high magnification picture of the sample, in order to measure later its diameter.

Then, with extreme care, the manipulator tip has to be moved away from the TEM grid and brought close to the device. Here, it is necessary to move the tip in order for the nanowire to fall down onto the device just across the gap between the thermal actuator and the displacement sensor. After a contact is established, the nanowire is fixed at both ends by the means of e-beam Platinum deposition (figure 6.2).

Different problems may arise during this mounting operation. First, there may be difficulties in lifting the nanowire up from the TEM grid. Such inconvenience can be solved by welding one end of the nanowire to the manipulator tip by e-beam Platinum deposition. However, such welding should not be too strong, since it must be broken later, when the nanowire has to be attached to the device.

Second, welding of the nanowire to the device can be challenging, since it is difficult to realize under SEM whether the sample is or is not in contact on both sides of the device. In this case, many steps of Pt deposition may be required.

Thus, proper positioning of the sample is a delicate task which may require many hours and good manipulation skills.

6.1.3 Tuning of the PID controller

As mentioned in chapter 4, the parameters of the PID controller (the proportional gain (K_p), the derivative constant (K_d), and the integral constant (K_i)) have to be correctly identified. In this work, the procedure for tuning such constants follows the Ziegler-Nichols method. It is based on the study of the step response of the open-loop system, from which the delay time L and the time constant T can be derived (figure 6.3).

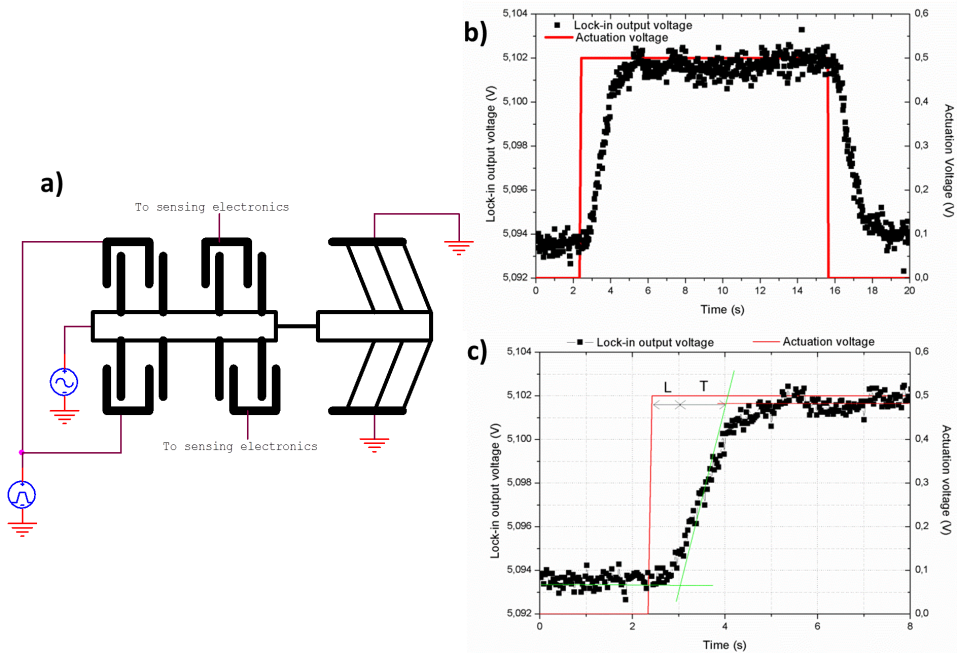

Figure 6.3: a) Electrical connections for tuning the PID parameters according to the Ziegler-Nichols method; b) Step response of the open-loop system, whose initial section is detailed in c)

These two constants allow for derivation of K_p, K_d, and K_i according to the

following formulas [177]:

$$K_p = 1.2\frac{T}{L^2}$$
$$K_d = 0.6\,T$$
$$K_i = 0.6\frac{T}{L}$$

In this case, the open-loop system is made of the electro-capacitive unit, the nanowire, and the thermal actuator (which however is not active), and is excited by a step voltage biasing the electrostatic actuator, causing a displacement of the sensor.

From the analysis of the step response, it is possible to derive T and L (figure 6.3), and then K_p, K_d, and K_i. However, this set of initial values do not necessary has to be the one effectively used during the test. In fact, these values can be experimentally refined in order to achieve the desired closed loop response. The closed-loop scheme consists of the electro-capacitive unit, the PID controller, the nanowire, and the thermal actuator. The PID controller should react in the shortest possible time, in order to restore the balance as soon as an external disturbance is applied (e.g., a displacement of the electro-capacitive unit).

In order to evaluate the closed-loop response, the closed-loop system is excited through the thermal actuator, which generates a sufficiently small displacement, able to produce a detectable change in the lock-in voltage, while not significantly stretching the nanowire (e.g., few nanometers displacement).

Figure 6.4 shows how the variation of the integral constant can produce a faster closed-loop response. However, as known from the literature, the increase of the integral constant can also introduce instability inside the

system, as visible from the last step, which corresponds to the highest gain and shows the onset of oscillations. Thus, a trade-off value must be found. A similar experimental tuning of the proportional and derivative constants can be performed, too.

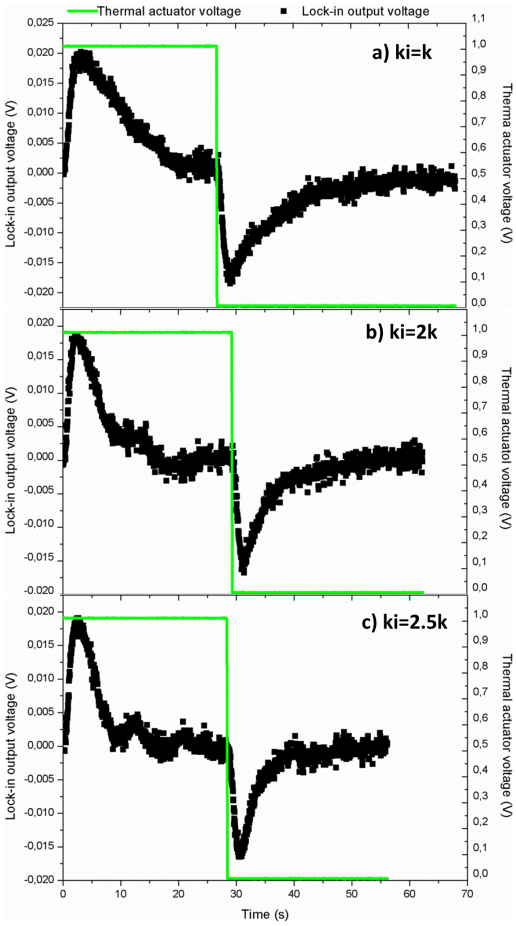

Figure 6.4: Step response of the device in closed-loop configuration at varying value of the PID integral constant: a) Initial K_i, b) Double K_i, c) Initial K_i multiplied by a factor of 2.5.

However, the tuning of the PID controller must be repeated each time a new test is prepared on a different nanowire, since the system response depends on the nanowire itself.

6.1.4 Testing control tools

Monitoring of the test progress is performed by the means of the feedback control VI, shown in chapter 4. This in fact offers a graphical interface, showing real-time evolution of the main signals involved, which are the lock-in amplifier output voltage, the thermal actuator bias voltage (which is controlled manually), and the control voltage applied to the electrostatic actuator. In this way, it is possible to verify that everything is working as expected, and, if necessary, it is possible for the operator to adjust some parameters without interrupting the test.

6.2 Application of the device for mechanical characterization of silver nanowires

In order to assess the effectiveness of the device previously described, this was used for testing of penta-twinned silver nanowires, for which reference values of the Young modulus (80-100 GPa [180]-[181]) and ultimate strength (in the order of few GPa [180]) are already available in the literature.
In the following, first an overview of the different techniques developed for testing silver nanowires is shown, then, attention is paid to testing of such nanowires with the present device. In particular, all of the obtainable information is shown for an exemplary case, while in the next section the data reduction process is reported, and the results of three different tests in terms of stress-strain curve are collected and discussed.

6.2.1 Overview of other methods for mechanical testing of silver nanowires

Due to their extraordinary electrical, optical, and mechanical properties, nanostructures, like metallic nanowires, are attracting increasing interest as potential building blocks in the next generation of electronic devices [182]-[184]. Among them, particularly attractive is silver, which shows the highest thermal and electrical conductivity at the nanoscale [185].

Many studies have been performed on silver nanowires, in order to determine its main mechanical properties, like the Young modulus and the yield strength. A common test involves the atomic force microscope (AFM) [186]. In this case, a solution of silver nanowires is dispersed over a silicon wafer with holes on the surface, in order to end up with nanowires suspended over a hole. Then, the AFM cantilever tip is brought into contact with the nanowire midpoint and moved downwards, in order to apply a bending load. From knowledge of both the force and the displacement, the Young modulus can be inferred by using proper expressions derived from the classical beam theory. Obviously, one of the stringent condition for an effective bending test, like the one mentioned herein, refers to the boundary conditions. In fact, it is necessary to verify each time that the nanowire adheres well to the substrate for the hypothesis of clamped ends to apply.

Another typical technique is acoustic atomic force microscopy (AFAM), which was already described in the first chapter. As before, the sample is still a nanowire suspended over a perforated substrate. The tip of the AFM is brought into contact with the sample midpoint, and then from measurement of the resonance spectrum, the Young modulus is derived [187].

Alternatively, an AFM was used to perform nanoindentation tests. In this

case, the load is applied through the AFM cantilever tip, which leaves on the sample an indentation area. The applied force can be directly measured through the same AFM, which can then be used also to scan the indentation area, after each step. Thus, an indentation stress-strain curve can be derived [182].

The literature offers also an example of tensile tests on silver nanowires, which were carried out with the tensile testing device described in detail in chapter 2 [180].

The performed studies have brought to very interesting results. In fact, beyond the scale effect, already observed in other kind of materials, sample's nanostructure has been found to play a role on the global mechanical behavior.

Atomic arrangement depends on the fabrication technique adopted for sample synthesis. It may follow either a bottom-up or a top-down approach. In the first case, the sample is extracted from a bulk structure with lithography or mechanical reduction [188]. In the second case, nanowires are grown by for example chemical or molecular assembly [188].

It has been shown that when synthesized by bottom-up techniques, silver nanowires acquire a unique structure, characterized by multiple twins. Such nanowires exhibit higher yield strength and lower ductility than twin free nanowires. This is due to the presence of twins which hinder the dislocation movement [189].

The standard hardening techniques used at the macroscale are not effective when considering nanocomponents. Such conventional techniques involve incorporation of inclusions and grain-boundary hardening. However, this first option is not feasible in the case of nanowires, since inclusions may be easily expelled [181]. Thus, playing with nanowires nanostructure can be

the key for modifying their global mechanical behavior.

In particular, for a correct tuning of the mechanical behavior of nanowires it is necessary a good control of their crystal structure [184]. Nevertheless, an intense work of mechanical characterization is required, too. However, in spite of the number of studies about silver nanowires, the data available in the literature still show a significant dispersion [188]. Furthermore, discussion is still open about the mismatch between the results, especially about the size effect on the Young modulus, obtained with experiments and numerical analysis, based on molecular dynamics (MD) [190]. Such mismatch can be related to the presence of contaminants, as oxide, during experiments, which is obviously neglected in the numerical simulations. Thus, further work is still required.

6.2.2 Testing of silver nanowires with the present MEMS device

As said in chapter 3, five different types of device were designed, each with a specific feature. Herein, only the tensile testing devices with a thermal actuator were considered, postponing the study of the others to a next future. Some preliminary tests were conducted with the tensile testing device not provided with electrical isolation of the specimen. However, these showed a constant drift in the lock-in amplifier voltage. Such drift might be related to the SEM electron beam, which, being directed to a metallic sample (as silver), could induce spurious effects in the sensing region of the device, which is connected to it. Such hypothesis is confirmed by the absence of drift when instead the tensile testing device with electrical isolation of the sample is

considered. All of the tests reported in the following were carried out with this latter device.

In order to explain with sufficient details how to process all the information available from a test with the present MEMS device, it is convenient to refer to an exemplary case. This involved a silver nanowire with a diameter of 71 ± 4 nm and gage length of $3.5 \pm 0.3\,\mu$m.

As already anticipated, during the test, three signals were monitored: the voltage applied to the thermal actuator, which was increased continuously such that the strain rate was about $6{\cdot}10^{-4}$, the lock-in output voltage (feedback voltage), and the control voltage applied to the electrostatic actuator (6.5).

As the voltage applied to the thermal actuator increases (e.g., the delivered displacement increases) (figure 6.5a), the control voltage applied to the electrostatic actuator (figure 6.5b) increases, accordingly, while the lock-in amplifier output voltage remains reasonably steady (figure 6.5c), meaning that the electro-capacitive unit keeps its equilibrium position. In fact, the lock-in amplifier output voltage is proportional to the displacement, and can be calculated as shown in the previous chapters as:

$$\mathrm{V_{lock}} = G \cdot 2\pi f_{ref} \frac{V}{\sqrt{2}} \Delta C \tag{6.1}$$

where G is the gain of the current pre-amplifiers carrying the signals to the lock-in amplifier, ΔC is the capacitance variation, which has to be measured, $\sqrt{2}$ is introduced because the output signal is displayed as RMS, $\mathrm{V_0}$ and $\mathrm{f_{ref}}$ are the amplitude and the frequency of the reference AC signal of the lock-in amplifier, respectively. By inverting such equation ΔC can be derived. Then, from the calibration curve of the displacement sensor, the corresponding displacement can be inferred.

Using such procedure, and considering the lock-in amplifier output voltage during the whole test (figure 6.5c), it can be realized that the electrocapacitive unit oscillates around equilibrium within a range of about less than ±10nm (with respect to a maximum displacement of about 600nm). Such sensitivity is comparable to the resolution of the well known force-balance accelerometer ADXL-50, developed by Analog Devices [191]. However, the factor which mainly affects the system resolution is the electrical noise, which sometimes could be lowered down in order to have a displacement resolution of ±5nm.

In regard to the control voltage (e.g., the electrostatic force applied to the displacement sensor), this does increase monotonically up to a certain value. After that it remains almost stable. This means that no additional force is required to further stretch the sample, which thus has reached a plastic plateau, as previously reported [180].

The monitored signals contain all the information required for derivation of the full stress-strain curve of the sample, as shown in the following.

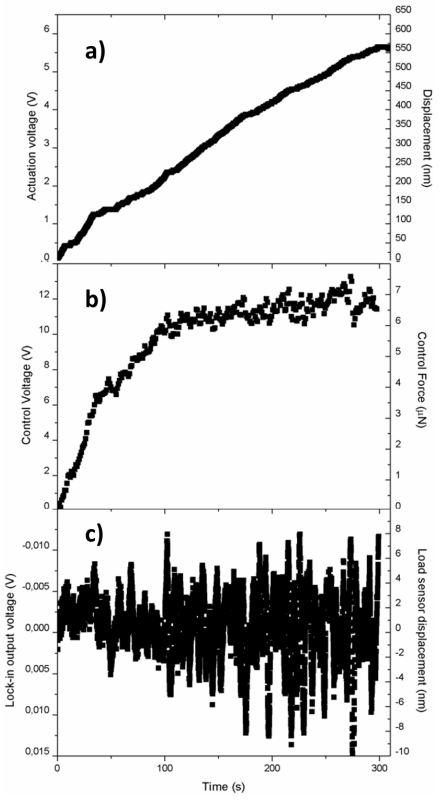

Figure 6.5: The signals monitored during the test: a) the voltage applied to the thermal actuator (and the corresponding displacement determined from its calibration curve), b) the control voltage and the corresponding electrostatic force, and c) the lock-in amplifier output voltage and the corresponding displacement of the electro-capacitive unit

6.3 Discussion of the results

Now, it is interesting to show the procedures for data reduction, in order to derive the sample stress-strain curve on the basis of the information previously shown.

6.3.1 Displacement measurement

The displacement undergone by the nanowire can be evaluated from successive real-time SEM pictures taken during the test (figure 6.6).

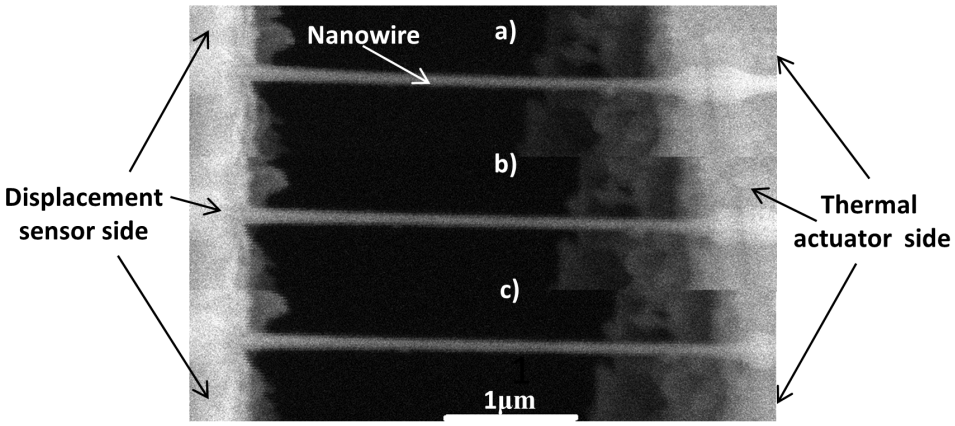

Figure 6.6: The nanowire at a) 0% strain, b) 3.8% strain, and c) 16% strain.

In particular, using the same correlation algorithm implemented inside a MATLAB code, which was already used to derive the displacement undergone by the device during calibration, it is possible to determine what is the relative displacement of the two ends of the sample. Such displacement can be compared to the displacement delivered by the thermal actuator. There are no SEM pictures available for the thermal actuator during the test, but the bias voltage was recorded. Thus, from the calibration curve it is possible

to identify what is the displacement corresponding to the applied voltage.

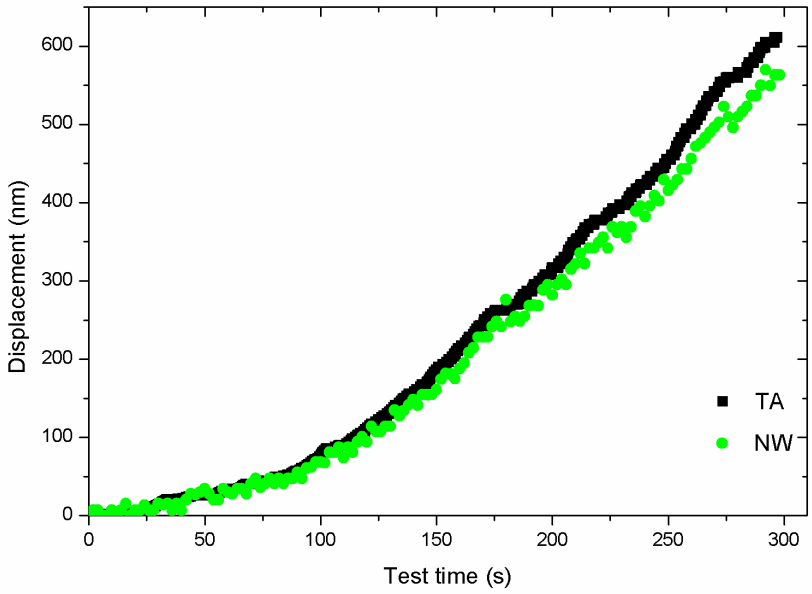

Figure 6.7: Comparison between the nanowire displacement (green line) and the expected displacement delivered by the thermal actuator (black line), as functions of the testing time.

Figure 6.7 reports a comparison between the sample displacement and the expected displacement of the thermal actuator, as functions of time. The curves show good agreement, meaning that almost all the displacement delivered by the thermal actuator was effectively transferred to the nanowire. This is a further confirmation that the electro-capacitive unit did not move significantly during the test. However, there is a slight mismatch between the two curves at the end. This may indicate that the strain rate might be too high at that step of the test. In fact, probably the actuator did not have

sufficient time to reach the displacement, recorded instead during calibration, which was performed in quasi-static condition.
From the displacement it is then possible to derive the strain undergone by the sample. This can be computed as the displacement divided by the gage length. Considering both the error on the initial gage length and the one on the sample displacement computed through the images, the resulting strain error was 0.05%, as average.

6.3.2 Load measurement

In the current design, the displacement sensor is not allowed to undergo any significant deflection if the feedback control is correctly implemented. The controller computes the voltage to be applied to the electrostatic actuator in order to balance any other external disturbance, like the force transmitted through the sample.
Thus, such a voltage changes as the external force changes, and can be used to measure this latter.
In fact, the electrostatic force (F) corresponding to the voltage (V) applied to the electrostatic actuator is:

$$F = \frac{1}{2}\epsilon N \frac{A}{d^2} V^2 \tag{6.2}$$

where ϵ is air permittivity, N the number of electrodes, A their transversal area, and d the gap between two adjacent electrodes, which can be considered to be equal to the initial value, since the electro-capacitive unit does not significantly move during the test.
The force can then be converted into stress. In this case, an engineering stress is considered, which can be computed as the force over the initial cross-sectional area of the sample, which is assumed to be constant [180].

The error on the stress, considering both the error on the area measurement and force, was about 0.2GPa.

6.3.3 Stress-strain curve

A deeper insight into the sample's behavior comes from the analysis of its stress-strain curve (figure 6.8).

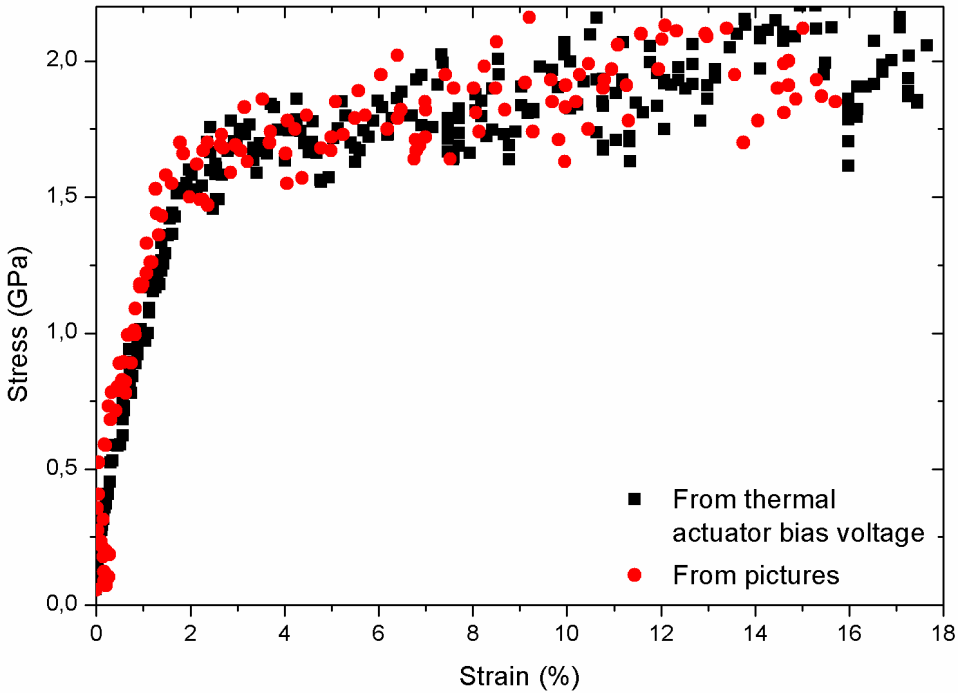

Figure 6.8: Stress-strain curve of the tested silver nanowire. In one case the strain is evaluated from SEM pictures of the sample (red circles), in the second case the strain is derived from the thermal actuator bias voltage (black squares)

In particular, figure 6.8 shows a comparison between two curves, one where the strain was evaluated through SEM pictures of the sample while testing,

and the other, where the strain was evaluated from the thermal actuator bias voltage and calibration, as explained in the previous section. These two almost overlap, except at the end where the second one extend to slightly higher strains. This can be explained recalling the difference between the sample displacement evaluated through SEM pictures, and the displacement derived from thermal actuator calibration. In particular, such difference was significant only at the end of the test, thus justifying the 2% difference in fracture strain. However, it is convenient to refer to the curve obtained using calibration of the thermal actuator, since it offers more resolution especially at the beginning of the test. Thus, this will be considered in the following discussion.

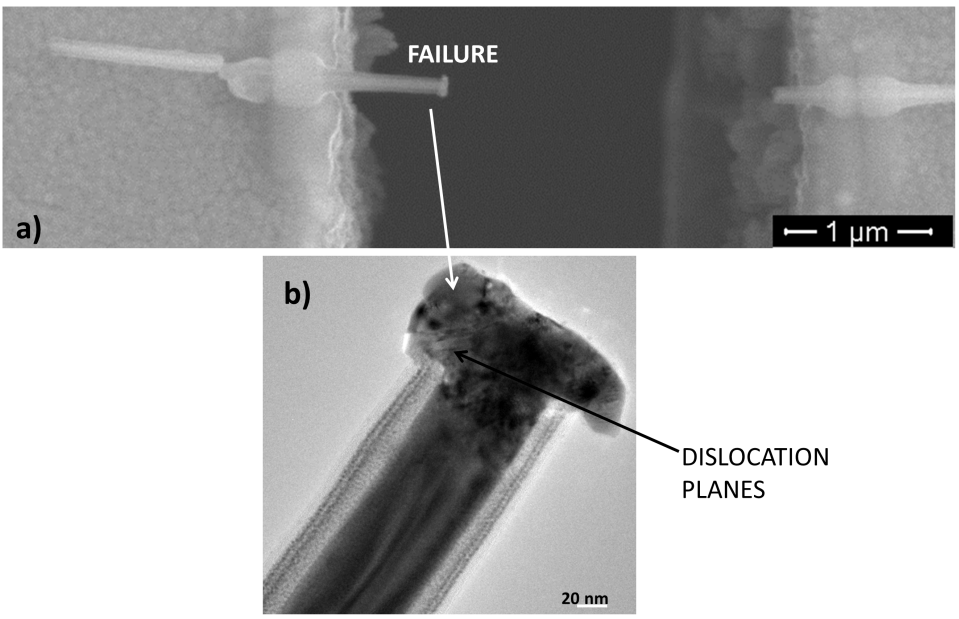

Figure 6.9: Fracture surfaces of the tested sample through SEM (a) and TEM observation (b).

Considering the linear portion of the curve (up to about 2% strain), the Young modulus results to be 85±2 GPa, showing good agreement with the values measured previously for this diameter [180]. However, the most significant feature of the curve is the fracture strain of the nanowire, which broke at about 16% strain.

Also the fracture stress of 1.95±0.2 GPa and the yield strength of 1.69±0.1 GPa are in good agreement with the data already reported in the literature.

It is now interesting to have a look to the fracture surface of the broken sample, which was imaged under TEM. Here, it is possible to notice a carbon layer deposited onto the sample during manipulation in the SEM. When the thickness of such layer increases significantly, it can affect the effectiveness of the test, since it increases the stiffness of the sample, as discussed in the next section in more details. Other features which can be noticed are some strips at the uppermost end of the fracture surface, which correspond to dislocation planes, meaning that the sample reached the plastic regime.

The sample fracture surfaces are shown in the SEM and TEM pictures reported in figure 6.9.

6.3.4 Other results

Since silver does not exhibit significant singularities in its characteristic, it is interesting to analyze the stress-strain curve derived during other two tests, where the sample resulted to be covered by a thick layer of carbon[6], because of a long permanence under SEM (figure 6.10).

In particular, the curve labeled as 'Experiment 3' is the curve already shown in the previous section. The other two refer to nanowires with diameter of

[6]By thick layer of carbon is meant a layer with thickness comparable with that of the original silver nanowire.

71±4 nm ('Experiment 1') and 65± 4nm ('Experiment 2'), which could not be broken after testing. In fact, in these cases the force generated by the electrostatic actuator was needed to deform a kind of composite nanowire, consisting of the original silver nanowire as core, and a layer of carbon as shell, and the stress values reported in the plot were computed as the ratio of the generated electrostatic force over the total area of the composite sample. Obviously, in order to break such system, a higher force is required than that causing failure of the silver nanowire alone. In particular, the force necessary to break the composite nanowire was bigger than the maximum value the electrostatic actuator could generate with the actual setup.

The first ('Experiment 1') and second ('Experiment 2') curve show two different shapes, which can be explained as follows. At the beginning of the test, the composite nanowire exhibits a linear behavior, since both the silver nanowire and carbon shell are in the linear regime. However, after a certain strain has been applied (around 2%), silver yields (as emerges from analysis of the third curve). Thus, to further increase the sample elongation, an increment of force is required to further deform only the shell, since the stress on the internal nanowire has been saturated. This means that after yielding of the silver nanowire, the slope of the composite sample characteristic changes and in particular reduces, as visible from curve 1. In the case of curve 2, more analysis is necessary. In fact, at about 3% strain, the characteristic has an instantaneous drop. It is very likely that it occurred as soon as the silver nanowire reached its yielding stress. Then, because of opening of local cracks, the resistant area reduced, thus causing a load drop. After stabilization, the curve starts increasing again, with a less steep slope, corresponding to the Young modulus of the carbon shell.

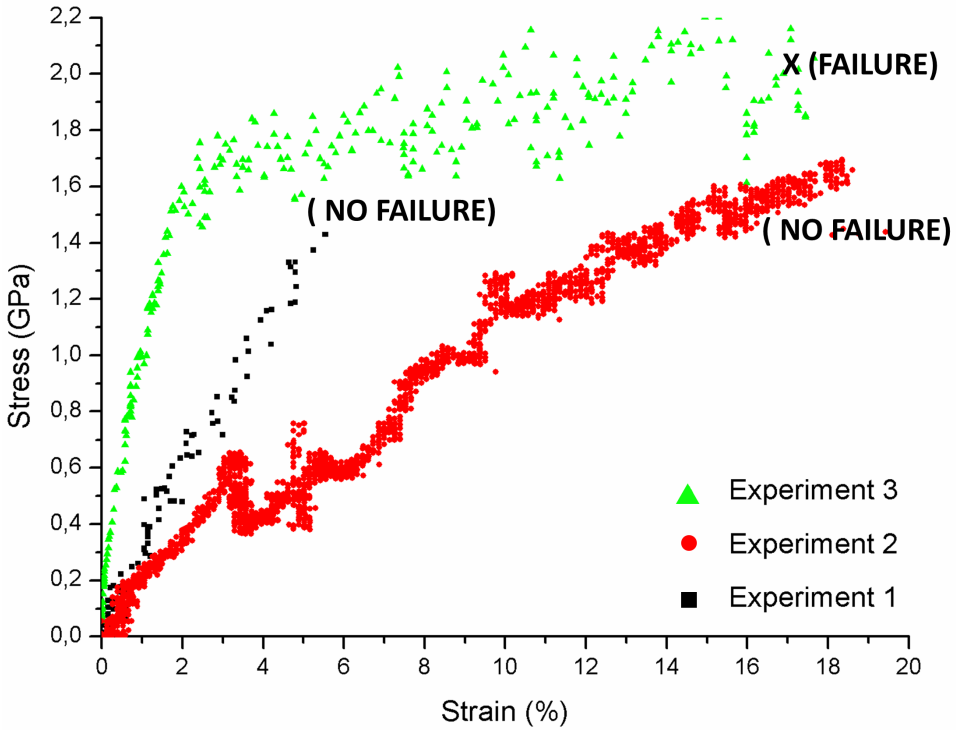

Figure 6.10: Comparison among three different stress-strain curves obtained from testing three different nanowires

In order to derive some quantitative information from experiments 1 and 2, it is interesting to consider the Young modulus of the composite nanowire (E^*). This can be computed as a function of the silver Young modulus (E_{Ag}) and the carbon shell Young modulus (E_c) through a classical mixture law:

$$E^* = E_{Ag} \cdot v_{Ag} + E_c \cdot v_c \tag{6.3}$$

where v_{Ag} and v_c are the volume fraction of the silver nanowire and carbon shell within the composite sample, respectively. From an SEM picture, it was possible to estimate the thickness of the carbon shell in both experiments

1 and 2. In particular, the global sample diameter resulted to be roughly three times the original nanowire radius. Thus,

$$v_{Ag} = \frac{A_{Ag}}{A_{tot}} = \frac{1}{9} \qquad v_c = \frac{A_c}{A_{tot}} = \frac{8}{9} \tag{6.4}$$

where A_{Ag}, A_c, and A_{tot} are the silver nanowire cross-sectional area, the carbon shell cross-sectional area, and composite sample area, respectively.

Exp n.	Diameter [nm]	E [GPa]	σ_y [GPa]	σ_u [GPa]	ϵ [%]
1	71±4	86±24	1.63±0.7	-	> 6
2	65±4	88±24	2.64±0.7	-	> 18
3	71±4	85±2	1.63±0.1	1.95±0.2	16

Table 6.1: Summary of the mechanical properties for silver as resulted from experiments on three different nanowires, where E is the Young modulus, σ_y the yield strength, σ_u the ultimate strength, and ϵ the percentage strain at fracture

From curves of Experiment 1 and 2, the initial slope results to be about 30±2 and 16±2 GPa, respectively. With reference to curve 3, silver can be modeled as a perfectly elasto-plastic material with reasonable approximation. Thus, the slope of the composite sample after yielding of the nanowire corresponds to the Young modulus of the carbon shell. In experiments 1 and 2, this results to be 23±2 and 7±2 GPa, respectively, which is close to the value of 13 GPa reported in literature [180]. Thus, the Young modulus of the silver nanowire can be back-calculated from the mixture law, providing 86±24 and 88±24GPa, respectively.

Furthermore, with reference to curve 2, it is possible to evaluate the expected stress (yield stress) inside the silver nanowire at 3% strain as: $\sigma_{Ag} =$

$E_{Ag} \cdot \epsilon = 88 \cdot 0.03 \approx 2.6$GPa. Such value, considering a corresponding uncertainty of 0.7 GPa, is reasonably close to the yield stress found for curve 3 (≈ 1.63 GPa). Nevertheless, it is possible that σ_y is higher in the second experiment, since this was conducted on a smaller sample, thus being affected by size effect.

Table 6.1 reports a summary of silver mechanical properties as determined through the above reported tests.

Finally, it is important to highlight that the testing system was able to detect the load drop in experiment 2. In fact, detection of singularities in the sample characteristic was the major requirement which motivated the design of the present testing stage.

6.4 Further developments

As shown in the previous section, the tensile load applied to the sample can be computed in real-time from the voltage applied to the electrostatic actuator. The sample displacement can instead be derived from image processing of successive SEM pictures recorded while testing. As an alternative method, the sample elongation can be computed in real-time from the thermal actuator bias voltage, which can be converted into displacement through its calibration curve. This procedure for strain measurement has three main advantages. First, it is not necessary to take hundreds of pictures for the sample, but eventually just few showing significant features, thus saving testing time. Second, upon reducing testing time and, above all, reducing imaging of the sample, also carbon deposition on samples is reduced. Third, on using the calibration curve of the thermal actuator for evaluation of displacement, it follows that load and displacement measurements of samples

during a test are really independent from each other.

However, calibration of the thermal actuator has to be conducted very carefully, trying to reproduce the strain rate expected later during test on a sample. Thus, it could be convenient to improve the current experimental setup, in order to develop a computer-assessed control of the thermal actuator bias voltage. This in fact should be able to guarantee a more regular strain rate applied during the whole test. Furthermore, also the architecture of the feedback control loop could be refined in order to provide a faster time response. In this way, very fast phenomena, as fracture initiation and failure of the sample, could be recorded. Thus, really complete stress-strain curve could be derived.

Finally, in future experiments the potential of the present device to provide electrical isolation of the sample from loading and sensing structures could be exploited, in order to perform electro-mechanical tests, aimed at determining electro-mechanical properties of samples, like piezoresistivity and piezoelectricity.

Conclusions

The interest in mechanical characterization of materials at the micro and nanoscale has significantly increased in the last decades, as indicated by the huge number of experiments carried out on micro/nanosamples. In order to provide a detailed description and classification of the different methodologies adopted in such experiments, an extensive bibliographic analysis was carried out (including about 600 papers and patents). This was aimed at establishing the suitability and limitations of each methodology for a specific application, thus providing guidelines for mechanical testing at the micro/nanoscale. In particular, the analysis revealed the on-chip testing devices to be the most interesting and promising tools for mechanical investigation at small length scales. In fact, these are very compact electromechanical systems (MEMS), and are able to provide deep insight in the mechanism of sample deformation. However, in spite of the intense work already done, further improvement is still required to enhance performances and overcome current limitations. For example, a major issue reported in a certain kind of tensile testing devices is the onset of instability, as soon as the sample under testing exhibits stress relaxation.

Such instability issue was studied with particular reference to the tensile testing device designed, fabricated, and applied at Northwestern University

(Evanston, IL) few years ago. The analysis was concluded with the indication of a possible solution (the introduction of a feedback control loop), which was then implemented in the design of a new class of testing devices, as described in detail in the present manuscript. In particular, five alternative devices were designed and fabricated, but of these only two typologies were considered herein, postponing the study of the others to a next future. Both of them allow performance of *in situ* SEM/TEM tensile testing of nanostructures under true displacement control, varying from the previous version for a novel system for load measurement. They differ from one another for the presence of electrical isolation of the sample from loading and sensing structures. In particular, this is an important feature, since it allows performance of electromechanical characterization of nanostructures, aimed at determining properties, like piezoresistivity and piezoelectricity.
The device provided with such feature was employed to perform the mechanical tests reported in the present manuscript. Here, the specimen was pulled at one end by a thermal actuator, and the displacement it delivered was determined with a resolution of few nanometers as a function of its bias voltage. By design, the sample elongation could be higher that 1μm, corresponding to a maximum strain of about 50%. In the present configuration, the strain rate was controlled manually by the operator, but a future development could introduce a computer-assessed control of the thermal actuator bias voltage, in order to guarantee a constant strain rate during tests.
A parallel-plate electrostatic actuator, controlled by a custom-made LabView routine (implementing a PID controller), measured the balance force applied to the other end of the sample, which, as a consequence, resulted to be fixed. This was designed in order to carry out force measurements with resolution of about 1μN for a maximum value of 100μN, and is at the

basis of a feedback control loop, consisting of a capacitive transducer (which measured the displacement of the sample side opposite to that connected to the thermal actuator) and the PID controller, too.

Both load and displacement can be monitored in real-time and recorded through independent signals by a computerized system operating in LabView environment. In this way, it is possible to derive the complete sample stress-strain curve, including those regions of stress relaxation, corresponding to inelasticity, phase transition, and necking.

Due to the above mentioned features, the device is suitable for testing a variety of nanostructures, especially one-dimensional nanostructures, like nanotubes and nanowires, with typical diameters of 10-200 nm and nominal gage length of 2μm.

However, following the design procedures illustrated for each of the elements included in the testing apparatus reported herein, other devices could be designed with customized measurement potentiality, thus further extending the application range to a wider variety of material samples.

The effectiveness of the designed testing system was successfully verified through an application on a silver nanowire with diameter of about 70 nm, whose mechanical properties were already known. The results obtained from such test agreed well with those reported in the literature.

As known, silver does not show significant singularities (e.g., load drops) in its characteristic. Nevertheless, the good attitude of the experimental apparatus to detect regions of stress relaxation was revealed by an experiment on a silver nanowire covered with a thick carbon layer, as may occur to samples kept for a long period under SEM. In this case, the stress-strain curve of the coated nanowire showed a load drop, which was successfully recorded. On the other hand, very fast singularities, as those associated to fracture initia-

tion and propagation until failure, could not be followed, meaning that the system time response should be improved. This could be done by refining the process of signals acquisition/generation through a more sophisticated electrical design.

In conclusion, good results obtained from testing on real samples have demonstrated the effectiveness of the developed experimental apparatus. However, more tests under SEM are still required for further validation, before performance of tests for characterization of other samples, especially under TEM. Moreover, additional work should be done in order to increase the system efficiency, thus reducing the long time required for setup calibration and specimen preparation. Time saving could be achieved by rearranging the involved external instrumentation in a more compact configuration, and adopting more automated calibration procedures.

Bibliography

[1] T. R. Hsu, MEMS and Microsystems-Design, Manufacture, and Nanoscale Engineering, John Wiley & Sons Inc., Hoboken, New Jersey, USA, (2008).

[2] J. W. Gardner, V. K. Varadan, O. O. Awadelkarim, Microsystems, MEMS and Smart Devices, John Wiley & Sons Inc., Chichester, UK, (2001).

[3] V. Labhasetwar and D. L. Leslie-Pelecky, Biomedical Applications of Nanotechnology, John Wiley & Sons Inc., Hoboken, New Jersey, USA, (2007).

[4] R. Osiander, M. A. G. Darrin, J. L. Champion, MEMS and Microstructures in Aerospace Applications. CRC Press, Boca Raton, FL, SA, (2006).

[5] M. F. Doerner, D. S. Gardner, W. D. Nix, Plastic properties of thin films on substrates as measured by submicron indentation hardness and substrate curvature techniques, J. Mater. Res. 1 (6) (1986) 845-851.

[6] C. A. Neugebauer, Tensile properties of thin, evaporated gold films, J. Appl. Phys. 31 (1960) 1096-1101.

[7] J. Monk, J. J. Hoyt, D. Farkas, Metastability of multitwinned Ag nanorods, Phys. Rev. B 78 (2008) 024112.

[8] D. Quian, G. J. Wagner, W. K. Liu, M.-F. Yu, R. S. Ruoff, Mechanics of carbon nanotubes, Appl. Mech. Rev. 55 (2002) 495-533.

[9] M. F. Pantano, H. D. Espinosa, L.Pagnotta, Mechanical characterization of materials at small length scales, J. Mech. Sci. Tech. 26 (2) (2012) 545-561.

[10] M. Alfano, L. Pagnotta, M.F. Pantano, A review of patented works on the mechanical characterization of materials at micro- nano-scale, Recent Patents on Nanotech. 5 (1) (2011) 37-45.

[11] K. Wouters and R. Puers Determining the Youngs modulus and creep effects in three different photo definable epoxies for MEMS applications. Sens. and Actuators A in press (2009).

[12] G. P. Zhang, C. A. Volkert, R. Schwaiger, P. Wellner et al, Length-scale-controlled fatigue mechanisms in thin copper films, Acta Mater. 54 (11) (2006) 3127-3139.

[13] M. A. Haque, H. D. Espinosa, H. J. Lee, MEMS for in situ testing-handling, actuation, loading, and displacement measurements, MRS Bulletin 36 (2010) 375-381.

[14] R. Liu, H. Wang, X. Li, G. Ding, C. Yang, A micro-tensile method for measuring mechanical properties of MEMS materials, J. Micromech. Microeng. 18 (2008) 065002.

[15] W. N. Sharpe Jr., B. Yuan , R. L. Edwards, A new technique for measuring the mechanical properties of thin films, J. Microelectromech. Syst. 6 (3) (1997) 193-199.

[16] E. Mazza, S. Abel, J. Dual, Experimental determination of mechanical properties of Ni and Ni-Fe microbars, Microsyst. Technol. 2 (1996) 197-202.

[17] D. A. LaVan and W. N. Sharpe Jr., Tensile testing of microsamples, Exp. Mech. 39 (1999) 210-216.

[18] M. A. Haque and M. T. A. Saif, In situ tensile testing of nanoscale freestanding thin films inside transmission electron microscope, Mater. Res. Soc. 20 (7) (2009) 1769-1777.

[19] P. B. Kaul, U. Singh, V. Prakash, In situ characterization of nanomechanical behavior of free-standing nanostructures, Exp. Mech. 49 (2009) 191-205.

[20] S. Cuenot, S. Dermoustier-Champagne, B. Nysten, Elastic modulus of polypyrrole nanotubes, Phys. Rev. Lett. 858 (2000) 1690-1693.

[21] T. Tsuchiya, O. Tabata, J. Sakata, Y. Taga, Specimen size effect on Tensile Strength of Surface-Micromachined Polycrystalline Silicon Thin Films, J. Microelectromech. Syst. 7 (1) (1998) 1057-7157(98)01301-8.

[22] E. P. S. Tan, C. N. Goh, C. H. Sow, C. T. Lim, Tensile test of a single nanofiber using an atomic force microscope tip, App. Phys. Lett. 86 (7) (2005) 073115.

[23] E. P. S. Tan and C. T. Lim, Physical properties of single polymeric nanofiber, App. Phys. Lett. 849 (2004) 1603-1605.

[24] S. Greek and S. Johansson, Tensile testing of thin film microstructures, Proc. SPIE 3224 (1997) 344-351.

[25] M. A. Haque and M. T. A. Saif, Application of MEMS force sensors for in situ mechanical characterization of nano-scale thin films in SEM and TEM, Sens. and Actuators A 97-98 (2002) 239-245.

[26] M. A. Haque and M. T. A. Saif, Deformation mechanisms in free-standing nanoscale thin films: A quantitative in situ transmission electron microscope study, Proc. of the Natl. Acad. of Sci. USA 101 (17) (2004) 63356340.

[27] S. Greek and F. Ericson, In situ tensile strength measurement and Weibull analysis of thick-film and thin film micromachined polysilicon structures, Mater. Res. Soc. Symp. Proc. 518 (1998) 51-56.

[28] J. A. Ruud, D. Josell, F. Spaepen, A new method for tensile testing of thin films, J. of Mater. Res. 8 (1) (1993) 112-117.

[29] T. A. Berfield, J. K. Patel, R. G. Shimmin, P.V. Braun, J. Lambros, N. R. Sottos, Micro- and Nanoscale Deformation Measurement of Surface and Internal Planes via Digital Image Correlation. Exp. Mech. 47 (2007) 51-62.

[30] W. G. Knauss and I Chasiotis, Mechanical measurements at micron and nanometer scale, Mech. of Mat., 35 (2003) 217-231.

[31] B. Han, Recent advancements of Moir and microscopic moir interferometry for thermal deformation analyses of microelectronics devices, Exp. Mech. 38 (4) (1998) 278-288.

[32] H. Xie, B. Li, B. Xu, J. Castracane, Focused Ion Beam Moir method, Optics and Lasers in Engineering 40 (3) (2002) 163-177.

[33] S. C.Yeon, Y.-H. Huh, D. I. Kim, J. H. Hahn, G. S. Kim, Y. H. Kim, Measurement of micro-tensile properties for hard coating material TiN, Advances in nondestructive evaluation 270-273 (2004) 1113-1118.

[34] C. S. Oh, H. J. Lee, S. G. Ko, S. W. Kim, H. G. Ahn, Comparison of the Youngs modulus of polysilicon film by tensile testing and nanoindentation, Sens. and Actuators A 117 (1) (2005) 151-158.

[35] J. J. Brown, A. I. Baca, K. A. Bertness, D. A. Dikin, R. S. Ruoff, V. M. Bright, Tensile measurement of single crystal gallium nitride nanowires on MEMS test stages, Sens. and Actuators A (2010) in press.

[36] M.T.A. Saif, N. C. MacDonald, Microinstruments for sub micron material studies, J. of Mat. Res., 13 (12) (1998) 3353-3356.

[37] J. H. Han and M. T. A. Saif, In situ microtensile stage for electromechanical characterization of nanoscale freestanding films, Rev. of Sci. Instrum. 77 (4) (2006) 045102.

[38] S. S. Hazra, M. S. Baker, J. L. Beuth, M. P. de Boer, Demonstration of an in situ on-chip tensile tester, J. of Micromech. and Microeng. 19 (2009) 082001.

[39] D. Zhang, W. Drissen, J. M. Breguet, R. Clavel, J. Michler, A high-sensitivity and quasi-linear capacitive sensor for nanomechanical testing applications, J. of Micromech. and Microeng. 19 (2009) 075003.

[40] Y. Zhu, C. Ke, H.D. Espinosa, Experimental determination of mechanical properties of Ni and Ni-Fe microbars, Microsyst. Technol. 2 (2007)19-202.

[41] S. N. Lu, D. A. Dikin, S. L. Zhang, F. T. Fisher, J. Lee, R. S. Ruoff, Realization of nanoscale resolution with a micromachined thermally actuated testing stage, Rev. of Sci. Instrum. 756 (2004) 2154 2162.

[42] A. Corigliano, L. Domenella, G. Langfelder, On-chip Mechanical Characterization using an Electro-thermo-mechanical Actuator, Exp. Mech. 50 (2010) 695-707.

[43] S. J. Eppel, B. N. Smith, H. Kahn, R. Ballarini, Nano measurements with micro-devices: mechanical properties of hydrated collagen fibrils, J. of the Royal Soc. Interface 3 (2006) 117-121.

[44] M. Naraghi, T., Ozkan, I. Chasiotis, M. P. de Boer, MEMS platform for on-chip nanomechanical experiments with strong and highly ductile nanofibers, J. of Micromech. and Microeng. 20 (2010) 125022.

[45] In-situ tensile testing of nano-scale specimens in SEM and TEM, Exp. Mech. 42 (1) (2002) 123-128.

[46] M. T.A. Saif, N. C. MacDonald, Microelectromechanical integrated microloading device (1998) US5786621.

[47] A. Haque, M. T. A. Saif, Apparatus and method for testing of microscale to nanoscale thin films (2004) US6817255 B2.

[48] W. Kang, M. T. Saif, A novel SiC MEMS apparatus for *in situ* uniaxial testing of micro/nanomaterials at high temperature, J. Micromech. Microeng. 21 (2011) 105017.

[49] H. D. Espinosa, Y. Zhu, N. Moldovan, Design and operation of a MEMS-based material testing systems for nanomechanical characterization, J. Microelectromech. Syst. 16 (5) (2007) 1219-1231.

[50] S. Gravier, M. Coulombier, A. Safi, N. Andre, A. Boe, J.-P. Raskin, T. Pardoen, New on-chip nanomechanical testing laboratory- Applications to Aluminum and Polysilicon thin films, J. Microelectromech. Systs. 18 (3) (2009) 555-569.

[51] V. Passi, U. Bhaskar, T. Pardoen, U. Sodervall, B. Nilsson, G. Petersson, M. Hagberg, J.-P. Raskin, High-throughput on-chip large deformation of Silicon nanoribbons and nanowires, J. Microelectromech. Syst. 21 (4) (2012) 822-829.

[52] M. D.Uchic, D. M. Dimiduk, J. N. Florando, W. D. Nix, Sample dimensions influence strength and crystal plasticity, Science 305 (5986) (2004) 986-989.

[53] J. R. Greer and W. D. Nix, Nanoscale gold pillars strengthened through dislocation starvation, Phys. Rev. B 73 (2006) 245410.

[54] J. R. Greer, W. C. Oliver, W. D. Nix, Size dependence of mechanical properties of gold at the micron scale in the absence of strain gradients, Acta Mater. 53 (2005) 1821-1830.

[55] S. Shim, H. Bei, M. K. Miller, G. M. Pharr, E. P. George, Effects of focused ion beam milling on the compressive behavior of directionally solidified micropillars and the nanoindentation response of an electropolished surface, Acta Mater. 57 (2009) 503-510.

[56] Z. W. Shan, R. K. Mishra, S. A. Syed Asif, O. L. Warren, A. M. Minor, Mechanical annealing and source-limited deformation in submicrometre-diameter Ni crystals, Nat. Mater. 7 (2) (2008) 115119.

[57] H. Zhang, B. E. Schuster, Q. Wei, K. T. Ramesh, The design of accurate micro-compression experiments, Scripta Mater. 54 (2006) 181-186.

[58] E. Suhir, Y. Xu, Y. Zhang, Method and apparatus for evaluation and improvement of mechanical and thermal properties of CNT/CNF arrays (2008) US20080096293 A1.

[59] V. T. Srikar, S. M. Spearing, A critical review of microscale mechanical testing methods used in the design of microelectromechanical systems, Exp. Mech. 43 (3) (2003) 238-247.

[60] S. M. Hu, Critical Stress in silicon brittle fracture, and effect of ion-implantation and other surface treatments. J of App Phys. 53 (5) (1982) 3576-3580.

[61] K. S. Chen, A. Ayon, S. M. Spearing, Controlling an Testing the fracture strength of silicon on the mesoscale, J. of the Am Ceram Soc. 83 (6) (2000) 1476-1484.

[62] A. Tuncay and A. T. Zehnder, A Monte-Carlo simulation of the effect of surface morphology on the fracture of nanobeams, Int. J. of Fracture 148 (2007) 129-138.

[63] H. Liu, C. H. Pan, P. Liu, Dimension effect on mechanical behavior of silicon micro-cantilever beams, Measurement 4 (2008) 885-895.

[64] G. J. McShane, M. Boutchich, A. Srikantha Phani, D. F. Moore, T. J. Lu, Youngs modulus measurement of thin-film materials using micro-cantilevers, J. of Micromech. and Microeng. 16 (2006) 1926-1934.

[65] M. P. de Boer, F. W. DelRio, M. S. Baker, On-chip structure suite for free-standing metal film mechanical property testing, Part I-Analysis, Acta Mater. 56 (2008) 3344-3352.

[66] M. P. de Boer, A. D. Corwin, P. G. Kotula, M. S. Baker, J. R. Michael, J. Subhash, M. J. Shaw, On-chip laboratory suite for testing of free-standing metal film mechanical properties, Part II-Experiments, Acta Mater. 56 (2008) 3313-3326.

[67] A. Corigliano, F. Cacchione, S. Zerbini, in: Yang, F. and Li, J. C. M. Micro and Nano Mechanical Testing of Materials and Devices, Springer, New York, USA Chapter 13, (2008).

[68] M. de Boer, F. Bitsie, B. D.Jensen, Electrostatic apparatus for measurement of microfracture strength (2002) US6424165 B1.

[69] T. J. Mackin, Z. C. Leseman, System and method for mechanical testing of freestanding microscale to nanoscale thin film (2006) US20060186874 Al.

[70] J. J. Vlassak W. D. and Nix, A new bulge test technique for the determination of Youngs modulus and Poissons ratio of thin films, J. of Mater. Res. 7 (1992) 3242-3249.

[71] X. Wei, D. Lee, S. Shim, S. Chen, J. W. Kysar, Plane-Strain Bulge Test for Nanocrystalline Copper Thin Films, Scripta Mater. 57 (2007) 541-544.

[72] P. M. Osterberg and S. D. Senturia, M-TEST: A test chip for MEMS material property measurement using electrostatically actuated test structures. J. of Microelectromech. Syst. 6 (2) (1997) 107-118.

[73] J. Sharma and A. DasGupta, Effect of stress on the pull-in voltage of membranes for MEMS application, J. of Micromech. and Microeng. 19 (2009) 115021.

[74] G. Fleury, C. Malhaire, C. Populaire, M. Verdier, A. Devos, P. L. Charvet, J. P. Polizzi, Mechanical cross-characterization of sputtered inconel thin films for MEMS applications, Sens. and Actuators B 126 (2007) 48-51.

[75] G. Stoney, Proc. of the Royal Soc. A 82 (1909) 172.

[76] J. Laconte, F. Iker, S. Jorez, N. Andr, J. Proost, T. Pardoen, D. Flandre, J.-P. Raskin, Thin film stress extraction using micromachined structures and wafer curvature measurements, Microelectron. Eng. 76 (2004) 219-226.

[77] H. D. Espinosa, B. C. Prorok, M. Fischer, A Novel Experimental Technique for Testing Thin Film and MEMS Materials, Proc. SEM Annual Conf. on Expt. and App. Mech., Portland, (2001) 446-449.

[78] H. D. Espinosa, B. C. Prorok, M. Fischer, A methodology for determining mechanical properties of freestanding thin films and MEMS materials, J. of the Mech. and Phys. of Solids 51 (2003) 47-67.

[79] Y. H. Huh, D. I. Kim, D. J. Kim, H. M. Lee, S. G. Hong, J. H. Park, C. D. Kee, Measurement of Mechanical Properties of thin film

by Membrane Deflection Test, Exp. Mech. (2009) DOI 10.1007/s11340-009-9247-4.

[80] H.D. Espinosa and B. Peng, A New Methodology to Investigate Fracture Toughness of Freestanding Thin Films and MEMS Materials, J. of Microelectromench. Syst. 14 (1) (2005) 153-159.

[81] H. D. Espinosa, B. Peng, N. Moldovan, T. A. Friedmann, X. Xiao, D. C. Mancini, O. Auciello, J. Carlisle, C. A. Zorman, M. Merhegany, Elasticity, Strength and Toughness of single Crystal Silicon Carbide, Ultrananocrystalline Diamond, and Hydrogen-free Tetrahedral Amorphous Carbon, App. Phys. Lett. 89 (7) (2006) 073111.

[82] B. Peng, H. D. Espinosa, N. Moldovan, X. Xiao, O. Auciello, J. A. Carlisle, Fracture Size Effect in UNCD - Applicability of Weibull Theory, J. of Mater. Res. 22 (4) (2007) 913-925.

[83] G. Schiltges, D. Gsell, J. Dual, Torsional tests on microstructures: two methods to determine shear-moduli, Microsyst. Technol. 5 (1998) 22-29.

[84] N. A. Fleck, G. M. Muller, M. F. Ashby, J. W. Hutchinson, Strain gradient plasticity: theory and experiments, Acta Met. et Mater. 42 (2) (1994) 475-487.

[85] D. J. Dunstan, B. Ehrler, R. Bossis, S. Joly, K. M. Y. P'ng, Elastic limit and strain hardening of thin wires in torsion, Phys. Rev. Lett. 103 (2009) 155501.

[86] A. P. Ternovskii, V. P. Alekhin, M. Kh. Shorshorov, M. M. Khrushchev, V. N. Skvortsov, The character of the variation of microhardness with

indentation size and the deformation behavior of materials under conditions of concentrated surface loading, Zavodskaya Laboratoriya 39 (1973) 1242.

[87] S. I. Bulychev, V. P. Alekhin, M. Kh. Shorshorov, A. P. Ternovskii, G. D. Shnyrev, Determining youngs modulus from the indenter penetration diagram, Zavodskaya Laboratoriya 41 (1975) 1137.

[88] J. B. Pethica, R. Hutchings, W. C. Oliver, Hardness Measurement at Penetration Depths as small as 20 nm, Taylor & Francis, London, UK (1983).

[89] W. C. Oliver and G. M. Pharr, An Improved Technique for determining Hardness and Elastic Modulus Using Load and Displacement Sensing Indentation Experiments, J. of Mater. Res. 7 (6) (1992) 1564-1583.

[90] Y. I. Golovin, Nanoindentation and Mechanical Properties of Solids in Submicrovolumes, Thin Near-Surface Layers, and Films: A Review, Phys. of the Solid State 50 (12) (2008) 2205-2236. [**?**] A. C. Fischer-Cripps, Critical review of analysis and interpretation of nanoindentation test data. Surface & Coatings Technol. 200 (2006) 4153-4165.

[91] Y.-T. Cheng and C.-M. Cheng, Scaling, dimensional analysis, and indentation measurements, Mater. Sci. and Eng. R 44 (2004) 91-149.

[92] W. C. Oliver and G. M. Pharr, Measurement of hardness and elastic modulus by instrumented indentation: Advances in understanding and refinements to methodology, J. of Mater. Res. 19 (1) (2004) 3-20.

[93] S. Kataria, S. Goyal, S. Dash, A. K. Tyagi, Nanomechanical characterization of thermally evaporated Cr thin films-FE analysis of the substrate effect, Thin Solid Films 519 (2010) 312-318.

[94] A. E. Giannakopulos, S. Suresh, Method and apparatus for determination of mechanical properties of functionally-graded materials (1999) US5999887.

[95] S. Suresh, A. Giannakopoulos, Method and apparatus for determining preexisting stresses based on indentation or other mechanical probing of the material (2001) US6311135 B1.

[96] T. Otiti, Y. Cao, S. M. Allameh, Z. Zong, O. Akogwu, W. O. Soboyejo, Nanoindentation measurements of mechanical properties of Ni thin films: Effect of microstructure and substrate modulus, Mater. and Manufacturing Process. 22 (2) (2007) 195-205.

[97] Y. S. Wang, S. L. Qu, Y. X. Gai, S. Dong, Y. C. Liang, Residual strains of aluminum alloy characterized by nanoindentation, Trans. of nonferrous metals Society of China 19 (3) (2009) 767-771.

[98] M. S. Kennedy, A. L. Olson, J. C. Raupp, N. R. Moody, D. F. Bahr, Coupling bulge testing and nanoindention to characterize materials properties of bulk micromachined structures, Microsyst. Technol. 11 (2005) 298-302.

[99] X. Li, B. Bhushan, K. Takashima, C.-W. Baek, Y.-K. Kim, Mechanical characterization of micro/nanoscale structures for MEMS/NEMS applications using nanoindentation techniques, Ultramicroscopy 97 (2003) 481-494.

[100] G. P. Zhang and Z. G. Zhang, in: G. C. H. Sih, Multiscale Fatigue Crack Initiation and Propagation of Engineering Materials: Structural Integrity and Microstructural Worthiness, Srpinger, (2008).

[101] D. H. Alsem, R.Timmerman, B. L. Boyce, E. A. Stach, J. Th. M. de Hosson, R. O. Ritchie, Very high-cycle fatigue failure in micron-scale polycrystalline films: Effects of environment and surface oxide thickness, J. of App. Phys. 101 (2007) 013515.

[102] S. P. Hannula, J. Wanagel, C. Y. Li, A comparative study of the mechanical properties of bonding wire, ASTM Special Technical Publications 850, American Society for Testing and Materials, Philadelphia. (1984).

[103] G. Kathibi, A. Betzwar-Kotas, V. Grger, B. Weiss, A study of the mechanical and fatigue properties of metallic microwires, Fatigue and Fracture of Engineering Materials & Structures 28 (2005) 723-733.

[104] R. Hofbeck, K. Hausmann, B. Ilschner, H. U. Kunzi, Fatigue of very thin copper and gold wires, Scripta Met. 20 (1986) 1601-1605.

[105] M. Judelewicz, H. U. Kunzi, N. Merk, B. Ilschner, Microstructural development during fatigue of copper foils 20-100 m thick, Mater. Sci. and Eng. A 186 (1-2) (1994) 135-142.

[106] S. Hong and R. Weil, Low cycle fatigue of thin copper foils, Thin Solid Films 283 (1996) 175-181.

[107] D. T. Read and J. W. Dally, Fatigue of microlithographically patterned free-standing aluminum thin-film under axial stress, J. of Electron. Packaging 117 (1995) 1-6.

[108] D. T. Read, Tension-tension fatigue of copper thin films, Int. J. of Fatigue 20 (3) (1998) 203-209.

[109] D. Son, J.-J. Kim, T. W. Lim, D. Kwon, Evaluation of fatigue strength of LIGA nickel film by microtensile tests, Scripta Mater. 50 (2004) 1265-1269.

[110] Y. Nagai, T. Namazu, S. Inoue, Fatigue life evaluation for single- and poly-crystalline silicon films by pulsating-tension cyclic loading test, Surface and Interface Analysis 40 (2008) 993-997.

[111] M. Hommel, O. Kraft, E. Arzt, A new method to study cyclic deformation of thin films in tension and compression, J of Mater Res. 14 (1999) 2373-2376.

[112] K. Takashima, Y. Higo, S. Sugiura, M. Shimojo, Fatigue crack growth behavior of micro-sized specimens prepared from an electroless plated Ni-P amorphous alloy thin film, Mater. Trans. 42 (2001) 68-73.

[113] G. P. Zhang, K. Takashima, M. Shimojo, Y. Higo, Fatigue behavior of microsized austenitic stainless steel specimens, Mater. Lett. 57 (2003) 1555-1560.

[114] R. Schwaiger and O. Kraft, High cycle fatigue of thin silver films investigated by dynamic microbeam deflection, Scripta Met. 41 (1999) 823-829.

[115] Y. C. Wang, A. Misra, R. G. Hoagland, Fatigue properties of nano scale Cu/Nb multilayers, Scripta Met. 54 (2006) 1593-1598.

[116] C. L. Muhlstein, Characterization of structural films using microelectromechanical resonators, Fatigue & Fracture of Eng. Mater. & Struct. 28 (8) (2005) 711-721.

[117] R. Monig, R. R. Keller, C. A. Volkert, Thermal fatigue testing of thin film metal films, Rev. of Sci. Instrum. 75 (2004) 4997-5004.

[118] J. Bagdahn and W. Sharpe, Fatigue of polycrystalline silicon under long-term cyclic loading, Sens. and Actuators A 103 (2003) 9-15.

[119] T. Ando, M. Shikida, K. Sato, Tensile-mode fatigue testing of silicon films as structural materials for MEMS, Sens. and Actuators A 93 (2001) 70-75.

[120] H. S. Cho, K. J. Hemker, K. Lian, J. Goettert, G. Dirras, Measured mechanical properties of LIGA Ni structures, Sens. and Actuators A 103 (2003) 59-63.

[121] M.-T. Lin, C.-J. Tong, K.-S. Shiu, Monotonic and fatigue testing of freestanding submicron thin beams application for MEMS, Microsyst. Technol. 14 (2008) 1041-1048.

[122] C.-Y. Kim, J.-H. Song, D.-H. Lee, Development of a fatigue testing system for thin films, Int. J. of Fatigue 31 (2008) 736-742.

[123] T. Hua, H. Xie, X. Feng, X. Wang, J. Zhang, P. Chen, Q. Zhang, A new dynamic device for low-dimensional materials testing, Rev. of Sci. Instrum. 80 (2009) 126108.

[124] S. He, J. S. Chang, L. Li, H. Ho, Characterization of Youngs modulus and residual stress gradient of MetalMUMPs electroplatednickel film, Sens. and Actuators A 154, (2009) 149-156.

[125] L. M. Zhang, D. Uttamchandani, B. Culshaw, Measurement of the Mechanical Properties of Silicon Microresonators, Sens. and Actuators A 29 (1991) 79-84.

[126] T. Ikehara, R. A. E. Zwijze, K. Ikeda, New Method for an Accurate Determination of Residual Strain in Polycrystalline Silicon Films by Analyzing Resonant Frequencies of Micromachined Beams, J. of Micromech. and Microeng. 11 (2001) 55-60.

[127] C. Q. Chen, Y. Shi, Y. S. Zhang, J. Zhu, Y. J. Yan, Size Dependance of Youngs Modulus in ZnO Nanowires, Phys. Rev. Letters 96 (2006) 075505.

[128] M. Alfano and L. Pagnotta, A non destructive technique for the elastic characterization of thin isotropic plates, NDT&E international 40 (2) (2007) 112-120.

[129] D. R. Frana and A. Blouin, All-optical measurement of in-plane and out-of-plane Youngs modulus and Poissons ratio in silicon wafers by means of vibration modes, Meas. Sci. and Technol. 15 (2004) 859-868.

[130] H. Ogi, N. Nakamura, M. Hirao, Advanced resonant ultrasound spectroscopy for measuring anisotropic elastic constants of thin films, Fatigue & Fracture of Eng. Mater. & Struct. 28 (8) (2005) 657 663.

[131] L. Kiesewetter, J.-M. Zhang, D. Houdeau, A. Steckenborn, Determination of Youngs moduli of microelectromechanical thin films using the resonance method, Sens. and Actuators A 35 (2) (1992) 153-159.

[132] C.-W. Baek, Y.-K. Kim, Y. Ahn, Y.-H. Kim, Measurement of the mechanical properties of electroplated gold thin films using micromachined beam structures, Sens. and Actuators A 1-3, (2005) 17-27.

[133] G. Rehder and M. N. P. Carreno, PECVD a-SiC: Youngs modulus obtained by MEMS resonant frequency, J. of Non-Crystalline Solids 354 (2007) 19-25.

[134] X. D. Bai, P. X. Gao, Z. L. Wang, E. G. Wang, Dual-Mode Mechanical Resonance of Individual ZnO Nanobelts, App. Phys. Lett. 82 (26) (2003) 4806-4808.

[135] Y.-J. Kim and M.G. Allen, In Situ Measurement of Mechanical Properties of Polyimide Films using Micromachined Resonant String Structures, IEEE Trans. on Components and Packaging Technol. 22 (2) (1996) 282-290.

[136] M. Bao, H. Yang, Squeeze film air damping in MEMS, Sens. Actuators A 137 (2007) 3-27.

[137] S. Nigro, L. Pagnotta, M. F. Pantano, Analytical and numerical modeling of squeeze-film damping in perforated microstructures, Microfluid. Nanofluid. 12 (2012) 971-979.

[138] M. Kothari, L. Kogut, C. Chu,i System and method for providing residual stress test structure (2007) US20070177129 Al.

[139] S. Banerjee, N. Gayathri, S. R. Shannigrahi, S. Dash, A. K. Tyagi, B. Raj, Imaging distribution of local stiffness over surfaces using atomic force acoustic microscopy, J. of Phys. D: App. Phys. 40 (8) (2007) 2539-2547.

[140] F. Mege, F. Volpi, M. Verdier, Mapping of elastic modulus at submicrometer scale with acoustic contact resonance AFM, Microelectron. Eng. 87 (3) (2010) 426-420.

[141] D. Passeri, M. Rossi, A. Alippi, A. Bettucci, A. Serra, E. Filippo, M. Lucci, I. Davoli, Atomic force acoustic microscopy characterization of nanostructured selenium-tin films, Superlattices and Microstructures 44 (4-5) (2008) 641-649.

[142] D. C. Hurley, K. Shen, N. M. Jennett, J. A. Turner, Atomic force acoustic microscopy methods to determine thin-film elastic properties, J. of App. Phys. 94 (4) (2003) 2347-2354.

[143] G. Stan, C. V. Ciobanu, P. M. Parthangal, R. F. Cook, Diameter-dependent radial and tangential elastic moduli of ZnO nanowires, Nano Letters 7 (12) (2007) 3691-3697.

[144] H. Kahn, R. Ballarini, J. J. Bellante, A. H. Heuer, Fatigue failure in polysilicon not due to simple stress corrosion cracking, Science 298 (2002) 1215-1218.

[145] S. Cho, J. F. Crdenas-Garca, I. Chasiotis, Measurement of nanodisplacements and elastic properties of MEMS via the microscopic hole method, Sens. and Actuators A 120 (2005) 163-171.

[146] V. T. Srikar, A. K. Swan, M. S. Unlu, B. B. Goldberg, S. M. Spearing, Micro-Raman Measurement of Bending Stresses in Micromachined Silicon Flexure, J. of Microelectromech. Syst. 12 (6) (2003) 779-787.

[147] L. De Wolf, Stress Measurements in Si Microelectronics Devices using Raman Spectroscopy, J. of Raman Spectroscopy 30 (1999) 877-883.

[148] M. A. Haque, H. D. Espinosa, H. J. Lee, MEMS for in situ testing-handling, actuation, loading, and displacement measurements, MRS Bulletin 36 (2010) 375-381.

[149] R. Agrawal, B. Peng, H. D. Espinosa, Experimental-Computational investigation of ZnO nanowires strength and fracture, Nanoletters 9 (12) (2008) 4177-4183.

[150] J. A. Pelesko, D. H. Bernstein, Modeling MEMS and NEMS, 2003, Chapman & Hall/CRC, Boca Raton, FL, USA.

[151] Y. Zhu, H. D. Espinosa, An electromechanical material testing system for in situ electron microscopy and applications, PNAS 102 (41) (2005) 14503-14508.

[152] Y. Zhu, N. Moldovan, H. D. Espinosa, A microelectromechanical load sensor for in situ electron and x-ray microscopy tensile testing of nanostructures, Appl. Phys. Lett. 86 (2005) 013506.

[153] H. D. Espinosa, Y. Zhu, N. Moldovan, Design and Operation of a MEMS-based material testing system for nanomechanical characterization, Journal of Microelectromech Syst. 16 (5) (2007) 1219-1231.

[154] H. Guo, K. Chen, Y. Oh, K. Wang, C. Dejoie, S.A. S. Asif, O. L. Warren, Z. W. Shan, J. Wu, A. M. Minor, Mechanics and Dynamics of the Strain-Induced M1-M2 Structural Phase Transition in Individual VO2 Nanowires, Nanoletters 11 (2011) 3207-3213.

[155] J. J. Brown, J. W.on Suk, G. Singh, A. I. Baca, D. A. Dikin, R. S. Ruoff, V. M. Bright, Microsystem for nanofiber electromechanical measurements, Sens. and Actuators A 155 (2009) 1-7.

[156] J. J. Brown, A. I. Baca, K. A. Bertness, D. A. Dikin, R. S. Ruoff, V. M. Bright, Tensile measurement of single crystal gallium nitride nanowires on MEMS test stages, Sens. and Actuators A (2010) DOI:10.1016/j.sna.2010.04.002.

[157] Y. Gao, Y. Fu, W. Sun, Y. Sun, H. Wang, F. Wang, J. Zhao, Investigation on the mechanical behavior of fivefold twinned silver nanowires, Computational Mater. Sci. 55 (2012) 322-328.

[158] R. A. Bernal, R. Agrawal, B. Peng, K. A. Bertness, N. A. Sanford, A. V. Davydov, H. D. Espinosa, Effect of growth orientation and diameter on the elasticity of GaN nanowires. A combined in situ TEM and atomistic modeling investigation, NanoLetters 11 (2011) 548-555.

[159] Y. Zhu, A. Corigliano, H. D. Espinosa, A thermal actuator for in situ microscopy testing: design and characterization, Journal of Micromech. Microeng. 16 (2006) 242-253.

[160] M. A. Hopcroft, W. D. Nix, T. W. Kenny, What is the Young's Modulus of Silicon?, J. Microelectromechanical Syst. 19 (2) (2010) 229-238.

[161] C. L. Wong, M. Palaniapan, Phonon detection technique for the study of the temperature coefficient of resonance frequency in clamped-clamped beam resonators, J. Micromech. Microeng. 19 (2009) 065021.

[162] D. Zhang, J.-M. Breguet, R. Clavel, V. Sivakov, S. Christiansen, J. Michler, *In situ* Electron Microscopy Mechanical Testing of Silicon Nanowires Using Electrostatically Actuated Tensile Testing Stages, J. Microelectromech. Syst. 19 (3) (2010) 663-674.

[163] L. Li, M. Begbie, G. Brown, D. Uttamchandani, Design, simulation and characterization of a MEMS optical scanner, J. Micromech. Microeng. 17 (2007) 1781-1787.

[164] D. C. Miller, B. L. Boyce, M. T. Dugger, T. E. Buchheit, K. Gall, Characteristics of a commercially available silicon-on-insulator MEMS material, Sens. Actuators A 138 (2007) 130-144.

[165] C. Yamahata, D. Collard, B. Legrand, T. Takekawa, M. Kumemura, G. Hashiguchi, H. Fujita, Silicon nanotweezers with subnanometer resolution for the micromanipulation of biomolecules, J. Microelectromech. Syst. 17 (3) (2008) 623-631.

[166] W. C. Young. R. G. Budynas, Roark's formulas for stress and strain, Mc Graw Hill, New York, USA, (2002).

[167] M. Bao, Analysis and Design principles of MEMS devices, Elsevier, Amsterdam, The Netherlands, (2005).

[168] SOIMUMPs Design Handbook, Rev. 7.0.

[169] Y. Zhang, X. Liu, C. Ru, Y. L. Zhang, L. Dong, Y. Sun, Piezoresistivity characterization of synthetic silicon nanowires using a MEMS device, J. of Microelectromech. Syst. 20 (4) (2011) 959-967.

[170] E. H. Sarraf, B. Cousins, E. Cretu, S. Mirabbasi, Design and implementation of a novel sliding mode sensing architecture for capacitive MEMS accelerometers, J. Micromech. Microeng. 21 (2011) 115033.

[171] J. Cui, Z. Guo, Q. Zhao, Z. Yang, Y. Hao, G. Yan, Force rebalance controller synthesis for a micromachined vibratory gyroscope based on sen-

sitivity margin specifications, J. Microelectromech. Syst. 20 (6) (2011) 1382-1394.

[172] I Veryeri, I. Basdogan, Adjusting the vibratory response of a micromirror via position and velocity feedback, J. Vibration Control 17 (1) 69-79.

[173] M. Vagia, Y. Koveos, G. Nikolakopoulos, A. Tzes, Robust proportional-integral-derivative controller design for an electrostatic micro-actuator with measurement uncertainties, IET Control Theory & Applications 4 (12) (2010) 2793-2801.

[174] B. Koo, X. Zhang, J. Dong, S. M. Salapaka, P. M. Ferreira, A 2 degree-of-freedom SOI-MEMS translation stage with closed-loop positioning, J. Microelectromech. Syst. 21 (1) (2012) 13-22.

[175] Y. Zhu, A. Bazaei, S. O. R. Moheimani, M. R. Yuce, Design, Modeling, and control of a micromachined nanopositioner with integrated electrothermal actuation and sensing, J. Microelectromech. Syst. 20 (3) (2011) 711-719.

[176] F. Shirazi, J. Mohammadpour, K. M. Grigoriadis, An LPV design approach for voltage control of an electrostatic MEMS actuator, J. Microelectromech. Syst. 20 (1) (2011) 302-311.

[177] J. R. Leigh, Applied control theory, Peter Peregrinus Ltd., London, UK, (1987).

[178] W. J. Porter, M. D. Uchic, R. John, N. B. Barnas, Compression property determination of a gamma titanium aluminide alloy using microspecimens, Scripta Mater. 61 (2009) 678-681.

[179] K. S. Kim, J. Y. Song, E. K. Chung, J. K. Park, S. H. Hong, Relationship between mechanical properties and microstructure of ultra-fine gold bonding wires, Mechanics of Materials 38 (2006) 119-127.

[180] T. Filleter, S. Ryu, K. Kang, J. Yin, R. A. Bernal,K. Sohn, S. Li, J. Huang, W. Cai, H. D. Espinosa, Nucleation-controlled distributed plasticity in penta-twinned silver nanowires, Small DOI: 10.1002/smll.201200522 (2012).

[181] B. Wu, A. Heidelberg, J. J. Boland, J. E. Sader, X. Sun, Y. Li, Microstructure-hardened silver nanowires, Nanoletters 6 (3) (2010) 468-472.

[182] M. Lucas, A. M. Leach, M. T. McDowell, S. E. Hundyadi, K. Gall, C. J. Murphy, E. Riedo, Plastic deformation of pentagonal silver nanowires: Comparison between AFM nanoindentation and atomistic simulations, Phys. Rev. B 77 (2008) 245420.

[183] J. Monk, J. J. Hoyt, D. Farkas, Metastability of multiwalled Ag nanorods: Molecular dynamics study, Phys. Rev. B 78 (2008) 024112.

[184] Y. Gao, Y. Fu, W. Sun, Y. Sun, H. Wang, F. Wang, J. Zhao, Investigation on the mechanical behavior of fivefold twinned silver nanowires, Computational Materials Science 55 (2012) 322-328.

[185] Y. Chen, B. L. Dorgan, Jr., D. N. Mcllroy, D. E. Aston, On the importance of boundary conditions on the mechanical bending behavior and elastic modulus determination of silver nanowires, J. Appl. Phys. 100 (2006) 104301.

[186] G. Y. Jing, H. L. Duan, X. M. Sun, Z. S. Zhang, J. Xu, Y. D. Li, J. X. Wang, D. P. Yu, Surface effects on elastic properties of silver nanowires: Contact atomic-force microscopy, Phys. Rev. B 73 (2006) 235409.

[187] S. Cuenot, C. Fretigny, S. Demoustier-Champagne, B. Nysten, Surface tension effect on the mechanical properties of nanomaterials measured by atomic force microscopy, Phys. Rev. B 69 (2004) 165410.

[188] A. M. Leach, M. McDowell, K Gall, Deformation of top-down and bottom-up silver nanowires, Advanced functional materials 17 (2007) 43-53.

[189] J. H. Yoo, S. I. Oh, M. S. Jeong, The enhanced elastic modulus of nanowires associated with multitwins, J. Appl. Phys. 107 (2010) 094316.

[190] M. T. McDowell, A. M. leach, K. Gall, On the elastic modulus of metallic nanowires, Nanoletters 8 (11) (2008) 3613-3618.

[191] G. A Kovacs, Micromachined Transducers Sourcebook, Mc Graw Hill, New York, USA, (1998).